

University of Alberta

**Effects of Y_2O_3 Additions on the Resistance of
Aluminum to Corrosive Wear**

by

Walid B. Khalifa Bouaeshi



A thesis submitted to the Faculty of Graduate Studies and Research in partial
fulfillment of the Master of Science

in

Materials Engineering

Department of Chemical and Materials Engineering

Edmonton, Alberta

Spring 2004



Library and
Archives Canada

Bibliothèque et
Archives Canada

Published Heritage
Branch

Direction du
Patrimoine de l'édition

395 Wellington Street
Ottawa ON K1A 0N4
Canada

395, rue Wellington
Ottawa ON K1A 0N4
Canada

Your file *Votre référence*

ISBN: 0-612-96452-3

Our file *Notre référence*

ISBN: 0-612-96452-3

The author has granted a non-exclusive license allowing the Library and Archives Canada to reproduce, loan, distribute or sell copies of this thesis in microform, paper or electronic formats.

L'auteur a accordé une licence non exclusive permettant à la Bibliothèque et Archives Canada de reproduire, prêter, distribuer ou vendre des copies de cette thèse sous la forme de microfiche/film, de reproduction sur papier ou sur format électronique.

The author retains ownership of the copyright in this thesis. Neither the thesis nor substantial extracts from it may be printed or otherwise reproduced without the author's permission.

L'auteur conserve la propriété du droit d'auteur qui protège cette thèse. Ni la thèse ni des extraits substantiels de celle-ci ne doivent être imprimés ou autrement reproduits sans son autorisation.

In compliance with the Canadian Privacy Act some supporting forms may have been removed from this thesis.

Conformément à la loi canadienne sur la protection de la vie privée, quelques formulaires secondaires ont été enlevés de cette thèse.

While these forms may be included in the document page count, their removal does not represent any loss of content from the thesis.

Bien que ces formulaires aient inclus dans la pagination, il n'y aura aucun contenu manquant.

Canada

Abstract

Aluminum has found many engineering applications due to its great formability, low density, and high resistance to corrosion. Since aluminum is not strong, it is usually strengthened by introduction of second phases, reinforcing particles or fibers.

The objective of this work is to strengthen aluminum without decreasing its corrosion resistance. Yttria was selected as reinforcing particles. It was demonstrated that by adding yttria particles, aluminum was strengthened with improved polarization behavior and higher resistance to corrosive wear in sulfuric acid and sodium chloride solutions. Microstructure of aluminum became finer. However, the added yttria particles were not observed in the modified aluminum. Instead, a new phase, Al_3Y , formed, which could result from possible decomposition or melting of the yttria particles during an arc melting process. The improved properties of aluminum by yttria addition could thus be largely attributed to the formation of Al_3Y phase and the resultant finer microstructure.

Acknowledgement

I would deeply like to thank Dr. Dongyang Li for his guidance and assistance during this work.

And I also would like to thank Alberta Energy Research Institute (AERI), National Science and Engineering Research Council of Canada (NSERC), Syncrude Canada Ltd, Suncor Energy, and Deloro Stellite Inc for their financial support.

Last but not least, I would like to express my great appreciation to Mr. Robert W. Kier for his help and support.

LIST OF CONTENTS

1	INTRODUCTION.	1
1.1	WEAR OF MATERIALS	1
1.2	WEAR MODES AND MECHANISMS.....	2
1.2.1	<i>Abrasive wear</i>	3
1.2.2	<i>Adhesive Wear</i>	6
1.2.3	<i>Erosive wear</i>	6
1.3	CORROSIVE WEAR	8
1.3.1	<i>Corrosion -Wear Mechanism and Material Protection</i>	8
1.4	RARE-EARTH ELEMENTS (RE)	9
1.5	APPLICATIONS OF RARE-EARTH ELEMENTS AGAINST AGGRESSIVE ENVIRONMENTS.....	11
1.5.1	<i>High-Temperature Oxidation</i>	12
1.5.2	<i>Effect of Rare Earth Elements on Corrosion Resistance</i>	24
1.5.3	<i>Effects of Rare Earths on Corrosive Wear</i>	28
2	MICROSTRUCTURE OF ALUMINUM MODIFIED WITH Y₂O₃ ADDITION.	
2.1	MATERIAL AND SAMPLE PREPARATION	36
2.2	MICROSTRUCTURAL OBSERVATION AND PHASE ANALYSIS	39
2.2.1	<i>Optical microscopy (OM), scanning electron microscopy (SEM), and energy dispersive spectroscopy (EDX) analysis:</i>	39
2.2.2	<i>X-ray diffraction (XRD) analysis</i>	45
3	MECHANICAL PROPERTIES OF ALUMINUM MODIFIED WITH Y₂O₃ ADDITION.	
3.1	HARDNESS MEASUREMENT.....	51
3.1.1	<i>Macro-Hardness Measurement</i>	54
3.1.1	<i>Micro-Hardness Measurement</i>	56
4	ELECTROCHEMICAL BEHAVIOR OF ALUMINUM MODIFIED WITH Y₂O₃ ADDITION..	
4.1	INTRODUCTION	64
4.2	ELECTROCHEMICAL POLARIZATION TEST	67
4.3	ELECTROCHEMICAL SCRATCH TEST.....	71
4.4	NANOINDENTATION ANALYSIS: MECHANICAL BEHAVIOR OF THE PASSIVE FILM	76
4.5	THE RESISTANCE OF PASSIVE FILM TO SCRATCH.....	80
5	CORROSIVE WEAR OF ALUMINUM MODIFIED WITH Y₂O₃ ADDITION.	
5.1	CORROSIVE WEAR MECHANISM	87
5.1.1	<i>Effect of Corrosion on Wear</i>	87
5.1.2	<i>Effect of Wear on Corrosion</i>	88
5.2	EVALUATION OF WEAR-CORROSION SYNERGISM	88
5.3	EFFECTS OF Y ₂ O ₃ ADDITIONS ON CORROSIVE WEAR OF ALUMINUM.....	90

5.3.1	<i>Experimental details</i>	90
5.3.2	<i>Results and Discussion</i>	92

6 SUMMARY AND FUTURE WORK.

6.1	SUMMARY OF THE THESIS	98
6.2	POSSIBLE FUTURE WORK.....	100
6.2.1	<i>Material Processing and sintering</i>	100
6.2.2	<i>Microstructural Observation</i>	102

REFERENCES	108
-------------------------	------------

LIST OF TABLES

Table 1.4-1 Rare-Earth elements [29].	10
Table 2.2-1 Chemical composition of 0, 5, 10, and 20wt%Y₂O₃-containing Al samples.	45
Table 3.1-1The variation of HRB number with yttria content.	54
Table 3.1-2 Microindentation measurements.	58
Table 3.1-3 The measured (η) ratio of the matrices in Yttria-free and Yttria-containing Aluminum samples.	60
Table 4.4-1 Nanoindentation Parameters results.	79
Table 4.5-1The critical failure loads of the passive film during scratch test	84
Table 6.2-1 Chemical composition of sintered 5, 10, and 20wt%Y₂O₃-containing Al samples.	106

LIST OF FIGURES

Figure 1.1-1 Disciplines involved in wear process	2
Figure 1.2-1 Wear Modes [3].	3
Figure 1.2-2 Types of contact during abrasion wear. (a) two-body abrasion, (b) three-body abrasion, [12]	4
Figure 1.2-3 Five mechanisms of abrasive wear [3].	5
Figure 1.2-4 A schematic of adhesion wear mechanism [12]	6
Figure 1.2-5 A schematic of erosion action of hard particles on a target surface [3].	7
Figure 1.5-1. The effect of 0.1%Ce(CeO₂) on morphologies of oxide scales respectively on	14
Figure 1.5-2. The effect of Cerium in both metal and oxide	15
Figure 1.5-3. TEM micrograph taken in the vicinity of an oxide/metal interface which shows a Y₃Al₅O₁₂ particles in the oxide and a fine YAlO₃ particles in the metal [84].	16
Figure 1.5-4. Mechanism for Y₃Al₅O₁₂ segregation at grain boundaries in Al₂O₃ oxide scale formed on an alumina-former alloy with Y₂O₃ [84].	17
Figure 1.5-5. Effect of RE additions on formation of inwardly growing pegs in Al₂O₃ scale: (A) detached scale formed on Fe-10Al-1Cu alloy. (B) deeply etched section of the tenacious scale formed on Fe-10Al-1Hf alloy, showing micro-pegs [81].	20
Figure 1.5-6. A proposed mechanism responsible for oxide spallation	22
Figure 1.5-7 Surfaces of Co-base alloy (imprint-free, completely imprinted) after removal of its surface oxide scale: a) without Yttrium, b) with Yttrium [104].	23
Figure 1.5-8. Rates of corrosion of wrought Mg and RE-containing Mg alloys NaCl compared to that of 2024 Al alloy [107].	25
Figure 1.5-9. Inhibition of corrosion of (a) aluminum 7075 alloy, (b) zinc and (c) mild-steel in aerated 0.1 N NaCl with 100 ppm mixed rare-earth chloride[117].	26
Figure 1.5-10. Potentiodynamic polarization curve of different aluminum alloys	27
Figure 1.5-11. Potentiodynamic polarization curves of 304	28
Figure 1.5-12 Variation in wear loss in 0.1M H₂SO₄ solution with respect to applied load: sliding speed 0.59 m/s, sliding distance 1000 m [121].	29
Figure 1.5-13 (a) 304 stainless steel; (b) 304 stainless steel containing 1 wt%. %Y;	30
Figure 1.5-14 Variation of corrosive wear rate of materials in	31
Figure 1.5-15 Variation in corrosion-erosion loss versus the velocity for	32
Figure 1.5-16 Electron work function of Y-free and Y-containing 304 Stainless steel	33
Figure 1.5-17 Load-displacement curves of Y-free and Y-containing 304 stainless steel samples passivated in 3.5% HNO₃ solution: (a) 304 stainless steel (0-50μ); (b) Y-containing 304 stainless steel (0-50μ); (c) 304 stainless steel (0-100μ); (d) Y-containing 304 stainless steel (0-100μ) [44].	34
Figure 1.5-18 Changes in electrical contact resistance after passivation treatment	34
Figure 2.1-1. Schematic of the apparatus for powder compaction.	38

Figure 2.2-1. Optical microscopy images; (a) Y_2O_3 -free Al, (b) 5wt% Y_2O_3 -containing Al,	41
Figure 2.2-2. SEM images of: (a) 5wt% Y_2O_3 -containing Al, (b) 10wt% Y_2O_3 -containing Al	43
Figure 2.2-3. EDX analysis for different spots illustrated in Fig. 2.2-2; (a) 5wt% Y_2O_3 -containing Al, (b) 10wt% Y_2O_3 -containing Al, (c) Y_2O_3 -containing Al.	44
Figure 2.2-4. X-ray diffraction patterns of Y_2O_3 -free aluminum	48
Figure 2.2-5. An Al-Y Phase Diagram [127].	49
Figure 3.1-1 A schematic representation of load –displacement curve	53
Figure 3.1-2 The change in HRB number as a function of the Yttria content.	55
Figure 3.1-3 The Fischer micromechanical probe.	56
Figure 3.1-4 Indentation tests of surfaces of various samples:	58
Figure 3.1-5 Increase in the hardness of the matrix by Yttrium.	59
Figure 3.1-6 Load-displacement curves of Yttria-free and Yttria-containing Aluminum samples.	60
Figure 3.1-7 Variation of (η) ratio in Yttria-free and Yttria-containing Aluminum samples.	61
Figure 3.1-8 The solubility of Yin Al shown in an Al-Y phase diagram [127].	62
Figure 3.1-9 An Aluminum-Yttrium phase diagram [127]	63
Figure 4.1-1 Typical polarization Curve of a passive metal	65
Figure 4.2-1 Polarization curves of Y_2O_3 -free and Y_2O_3 -containing samples in a 0.1M H_2SO_4 solution.	68
Figure 4.2-2 Polarization curves of Y_2O_3 -free and Y_2O_3 -containing samples in a 3.5wt%NaCl solution.	70
Figure 4.3-1 Schematic plot of anodic current versus time.	72
Figure 4.3-2 Schematic illustration of the electrochemical scratch set-up	74
Figure 4.3-3 Current-Time Curves in a 0.1M H_2SO_4 solution, 25mN and 0.5 Volts.	75
Figure 4.3-4 Current-Time Curves in a 0.1M H_2SO_4 solution, 35mN and 0.5 Volts.	76
Figure 4.4-1 Nano indentation curves of Y_2O_3 -free and Y_2O_3 -containing Aluminum samples under applied load of 15 μ N.	78
Figure 4.4-2 Nano indentation curves of Y_2O_3 -free and Y_2O_3 -containing Aluminum samples under applied load of 20 μ N.	79
Figure 4.5-1 Schematic of test setup for scratch and adhesion tests [145].	81
Figure 4.5-2 The geometry of the tip used in the scratch test.	81
Figure 4.5-3 ;a) Y_2O_3 -free Al, b) 5wt% Y_2O_3 -Al, c) 10wt% Y_2O_3 -Al, and d) 10wt% Y_2O_3 -Al.	84
Figure 5.3-1 A pin-one-disk tribometer for wear test.	91
Figure 5.3-2. Dry wear loss of Y_2O_3 -free and Y_2O_3 -containing Al samples against the applied load.	93
Figure 5.3-3. Wear losses of Y_2O_3 -free and Y_2O_3 -containing Al samples with respect to the applied load in a 0.1M H_2SO_4 solution.	94
Figure 5.3-4 Wear losses of Y_2O_3 -free and Y_2O_3 -containing Al samples with respect to the applied load in a 3.5wt% NaCl solution.	94

Figure 6.2-1 SEM images of samples sintered at 630°C for 8 hours: (a) 5wt% Y_2O_3 -containing Al, (b) 10wt% Y_2O_3 -containing Al, (c) 20wt% Y_2O_3 -containing Al. 103

Figure 6.2-2 EDX peaks for different points illustrated in Fig.6.2-1; a) 5wt% Y_2O_3 -containing Al, b) 10 wt% Y_2O_3 -containing Al, c) 20 wt% Y_2O_3 -containing Al. 105

1 Introduction

1.1 Wear of Materials

Wear may be generally defined as material removal when two surfaces rub each other. Wear occurs in a wide variety of operations in industry and results in large capital loss for repairing of various facilities. The damage to surface of components in a mechanical system may change their dimensions and could even cause failure of the entire system.

Wear is often affected by environment, such as corrosion. The environmental influence may result in synergism of chemical attack and mechanical wear, which could lead to significantly increased damage to a surface. In addition to the synergism of wear and environment factors, wear itself is also very complicated, involving mechanical, physical and chemical processes, such as deformation, fracture, adhesion, frictional heating, etc. These processes are largely affected by the wear conditions, including; the type of load, sliding speed, lubrication, temperature, materials properties, and surface finishing.

Due to its complexity, wear research certainly requires multidisciplinary expertise and approaches in order to develop effective techniques and materials against wear. Fig. 1.1-1 summarizes main subjects involved in wear research and materials protection.

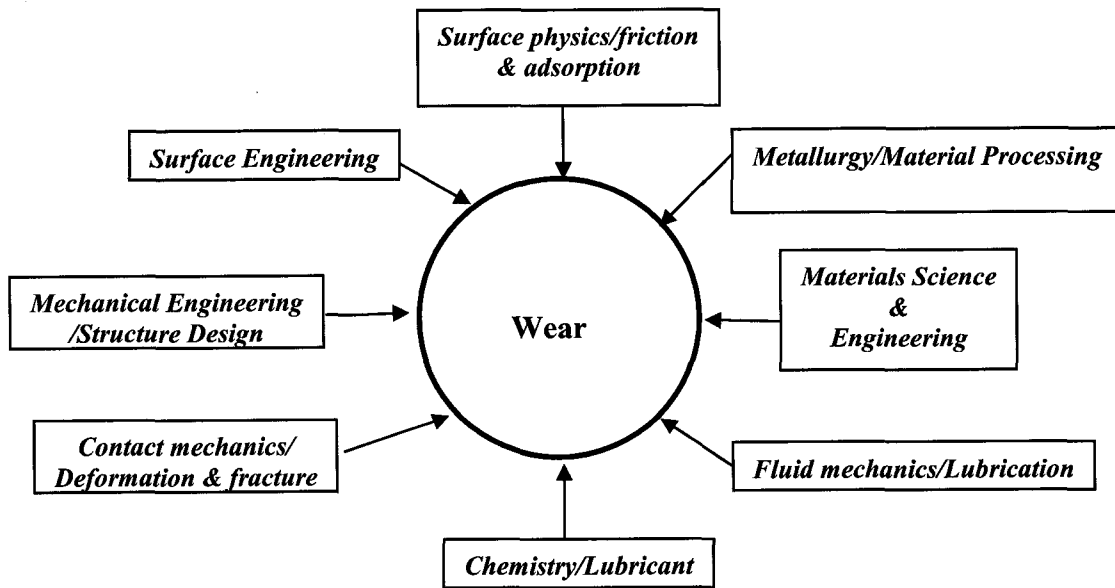


Figure 1.1-1 Disciplines involved in wear process

1.2 Wear Modes and Mechanisms

Wear may occur in various modes with different mechanisms. In general, mechanical wear may fall into three major categories [1]:

- 1) Sliding wear.
- 2) Impact wear.
- 3) Rolling contact wear [2].

Fig. 1.2-1 illustrates various modes of mechanical wear.

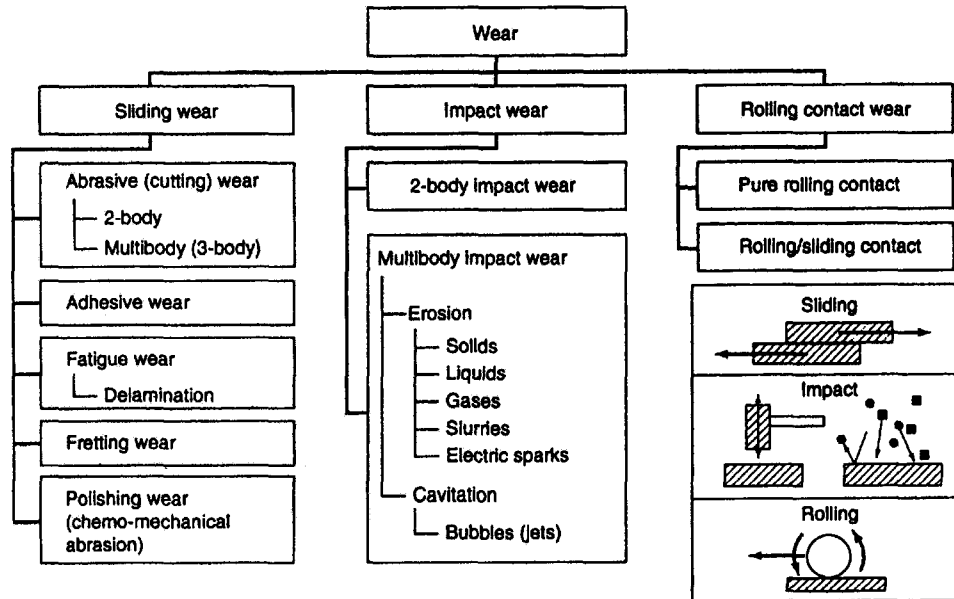
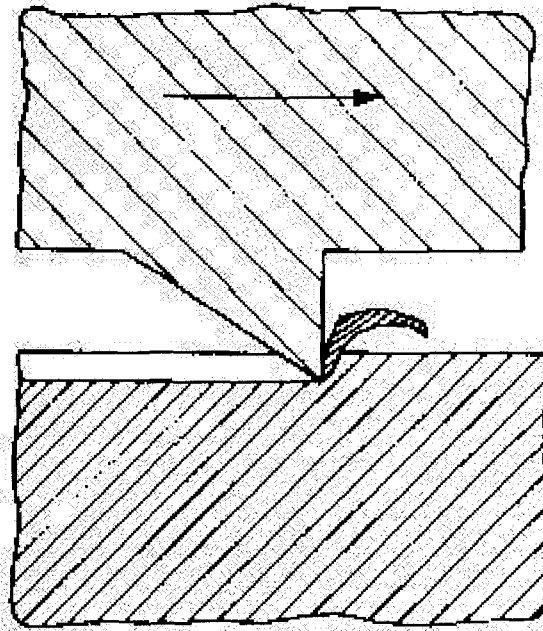


Figure 1.2-1 Wear Modes [3].

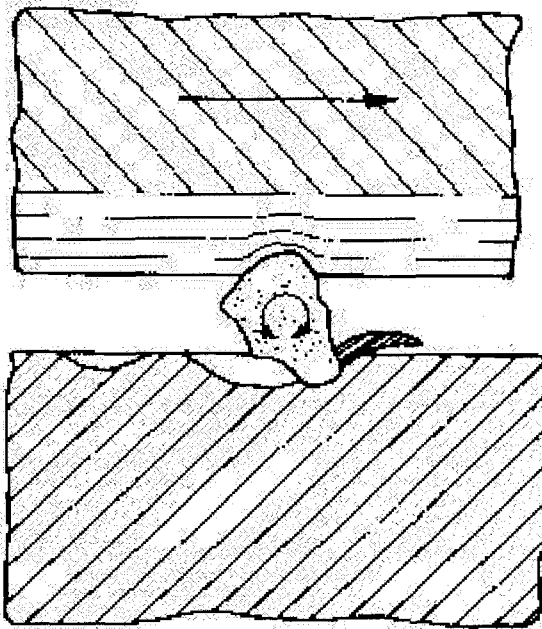
However, very often a wear process involves more than one mode. In the following section, three mechanical wear modes commonly encountered in industry are briefly introduced. They are; abrasive wear, adhesive wear, and erosion [3].

1.2.1 Abrasive wear

Abrasion involves the removal of material from a surface by the mechanical action of an abrasive, which has an acicular profile and is harder than the surface being worn. Abrasive wear usually takes place under two-body or three-body condition, as illustrated in Fig 1.2-2.



(a)



(b)

Figure 1.2-2 Types of contact during abrasion wear. (a) two-body abrasion, (b) three-body abrasion, [12]

In the former, abrasive particles slide along a surface with probable rotation, resulting in wear of the surface as illustrated in Fig 1.2-2 a). In three-body wear, abrasive particles exist between two surfaces which move in opposite directions as Fig 1.2-2 b) illustrates.

The removal of material during abrasion may involve several mechanisms including fracture, fatigue, and even melting when sliding speed is sufficiently high. An abrasion process may involve more than one wear mechanism. Plowing, wedge formation, cutting, microfatigue, and microcracking are often observed during abrasive wear (see Fig. 1.2-3).

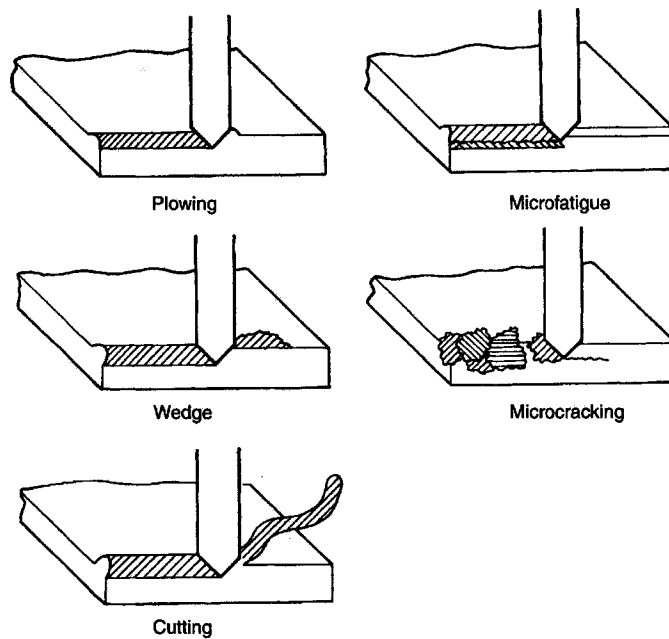


Figure 1.2-3 Five mechanisms of abrasive wear [3].

1.2.2 Adhesive Wear

Adhesive wear is defined as the removal of material due to large adhesion between two surfaces sliding on each other; Fig. 1.2-4 illustrates a schematic of adhesive wear. During adhesive wear, material may transfer from one surface to another and surface seizure may result, which could lead to failure of a mechanical system. Adhesive wear may occur between metallic materials, ceramics, polymers, or combination of these materials. Adhesive wear strongly depends on adhesion between the materials, strength of both surfaces, surface films, e.g., oxides or lubricants. The mutual affinity of materials play a major role in adhesive wear [3-11].

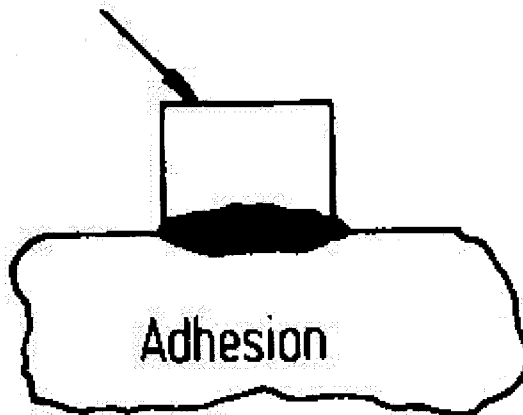


Figure 1.2-4 A schematic of adhesion wear mechanism [12]

1.2.3 Erosive wear

Erosive wear is described as loss of surface material that results from repeated impingement of liquid or solid particles. The primary factors causing erosion wear are velocity, impact angle, particle size, particle angularity, and mechanical properties of the

target material and the solid particles [1]. The solid particles may be suspended and carried by a medium such as air and water. Fig 1.2-5 illustrates material removal caused by action of repetitive compressive loading of hard particles. The stress involved in erosive wear is only occasionally large enough to break the solid particles. This implies that the original angularity and size of the particles are important to erosive damage to a target material [1-3, 11-20].

The severity of erosive wear is dependent on the impact velocity, impact angle, and mechanical properties of the surface. The higher the impact velocity, the larger the damage to the target surface. For soft materials, maximum erosion damage occurs usually at an angle of about 30° between the target surface and the direction of the erosive particles. For hard and brittle material, the maximum erosion may occur if the particles impinge the target surface vertically.

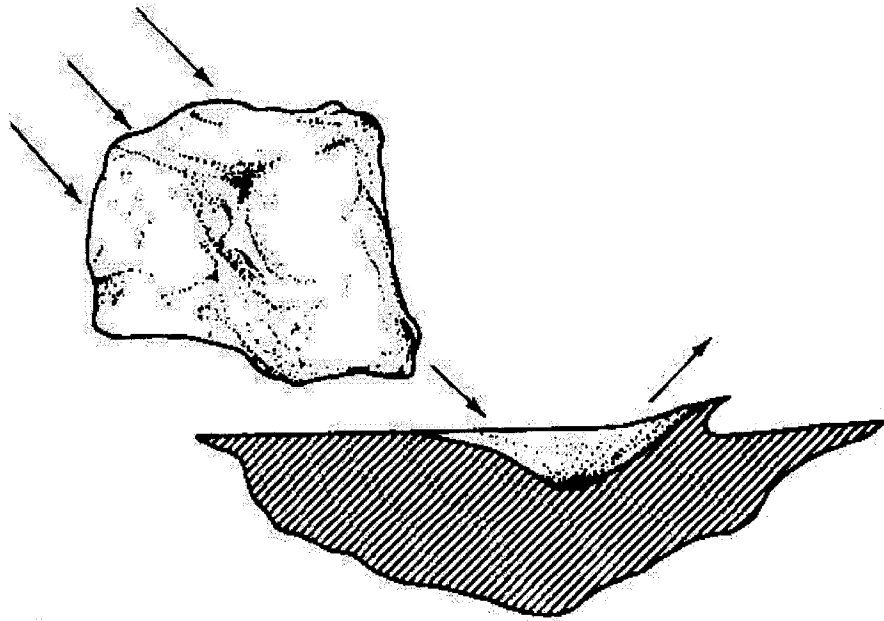


Figure 1.2-5 A schematic of erosion action of hard particles on a target surface [3].

1.3 Corrosive Wear

As mentioned earlier, wear is more or less influenced by environment, such as wear of mining facilities influenced by humidity and corrosive media.

The material damage due to wear could be much more severe if an aggressive medium is involved, i.e., corrosion. The synergy of corrosion and wear may result in total material loss much greater than those respectively caused by wear or corrosion. Corrosive wear is affected by many factors, which make the corrosive wear mode complicated.

1.3.1 Corrosion -Wear Mechanism and Material Protection

For those corrosion-resistant metals and alloys, whose corrosion resistance comes from the development of the surface passive films, properties of the passive films are very important from the standpoint of resistance to corrosive wear and erosion corrosion. When a material is attacked with the synergy of wear and corrosion, mechanical forces may damage the protective passive film. The resultant fresh metal surface is exposed to the aggressive environment, thus leading to accelerated damage to the metal. The ability of a passive film to protect its substrate depends on the speed and magnitude of mechanical force, the environment, also the resistance of the film to mechanical damage, and its rate of re-formation when destroyed or damaged.

An adherent, dense, and strong passive film would provide better protection and minimize the total damage than one that is easily removed by mechanical actions [3, 21-27].

1.4 Rare-Earth elements (RE)

An overview:

In recent years, there is increasing interest in application of rare-earth elements such as yttrium (Y) in enhancing the resistance of metallic materials to corrosive wear [28]. In the periodic table, there are 15 elements ($Z=57$ to 71) whose properties resemble each other (see Table 1.4-1), which are so-called rare-earth elements. The name of rare earth is originated from the Latin *terra rara*, which means “rare earth”.

They were considered rare for a long time, but investigations of the rare-earth elements in the last decades have shown that they are far more abundant than gold, lead, and mercury. All these elements are metals; often existing in ores and minerals [29].

Yttrium ($Z=39$) and Scandium ($Z=21$) are usually included with those elements, although they are not members in the rare-earths family. The reason lies in the similarity of their properties to those of the rare earth elements [30].

Table 1.4-1 Rare-Earth elements [29].

Z	Element	Symbol	Z	Element	Symbol
57	Lanthanum	La	65	Terbium	Tb
58	Cerium	Ce	66	Dysprosium	Dy
59	Praseodymium	Pr	67	Holmium	Ho
60	Neodymium	Nd	68	Erbium	Er
61	Promethium	Pm	69	Thulium	Tm
62	Samarium	Sm	70	Ytterbium	Yb
63	Europium	Eu	71	Lutetium	Lu
64	Gadolinium	Gd			

Historically, the rare earth elements did not find extensive use. However, with time the situation changed extensively, now the rare earth elements have found a wide range of applications in industry.

Mechanical properties of steel and pig iron are seriously affected by the content of impurities such as oxygen, nitrogen, sulfur, and phosphor. Great efforts are made to remove these elements during the process of melting. These elements negatively affect properties of the materials, by increasing brittleness, reducing ductility, and lowering their wear resistance. Because of the high reactivity of rare-earth elements, rare-earth elements have been used to remove non-metallic impurities by interacting with them at elevated temperatures and removing them with ease, thus improving the quality of the pig iron and steel [31-37].

Alloying rare-earth elements with nonferrous alloys such as aluminum and magnesium has also found a wide range of applications [38-40]. Al-Ce alloy was first obtained leading to important technical improvement in the improved mechanical properties and higher resistance to fatigue and cracking [29]. Recently have shown that alloying rare earths to aluminum and magnesium alloys can dramatically extend their service life with higher resistance to stress corrosion cracking [33, 41, 42]. It was also demonstrated that additions of rare-earth elements (0.5-1%) to steel [43], stainless steels [44, 45], pure aluminum [28], aluminum alloys [46-54], and aluminum composites [55], considerably increased their corrosion resistance.

1.5 Applications of rare-earth elements against aggressive environments

The high reactivity of rare earth elements makes them suitable for controlling corrosion of many materials. It was also demonstrated that the rare earth elements play an appreciable role in improving high-temperature oxidation resistance of Alumina, Chromia – forming alloys [56-66] in addition to improving their resistance to aqueous and atmospheric corrosion [46-54]. Applications of rare-earth elements have also been found in the field of Tribology. It was demonstrated that rare earths or reactive elements improved the wear and erosion resistance of pure aluminum [28], aluminum alloys [67], stainless steel [28, 67, 68], cast irons [69], in dry conditions and corrosive environments if they were added as alloying

elements or oxide particles, or applied as constituents in protective coatings [68, 70-73].

In the following sections, applications of rare earth elements in resisting high-temperature oxidation, aqueous corrosion, and wear are briefly reviewed.

1.5.1 High-temperature oxidation

The resistance of alloys and metallic coatings to oxidation relies on the formation of continuous and slow growing oxide scale. The oxide scales should be non porous, crack-free, and adherent to the substrate. Oxides having these capabilities are chromia, alumina, and silica. Chromia and alumina have much greater extent of applications than Silica. These oxide scales can be improved by alloying rare earth elements such as Ce to the alloy substrate. It was observed 65 years ago that adding a small amount of Cerium as a deoxidizer to a chromium-containing heater alloy resulted in significant increase in the service life of the alloy [74]. The improvement in oxidation resistance by adding reactive elements is mainly attributed to the reduction in the oxidation rate, enhancement of oxide adhesion, and higher resistance to spallation [75].

1. The effect of rare-earth elements on initial oxidation:

The mechanisms responsible for the improvement in oxidation resistance by adding rare earth elements may be: 1) heterogeneous nucleation of the oxide scale,

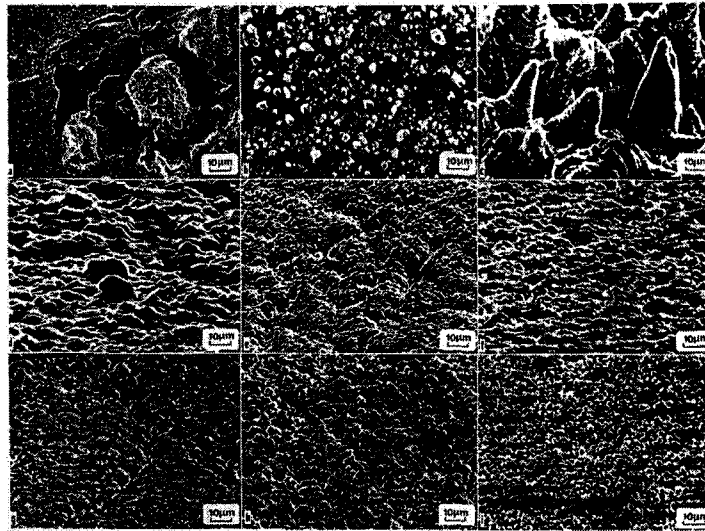
2) modification of the alloy's diffusivity, and 3) the formation of a barrier layer on the alloy substrate [75-77].

- Heterogeneous nucleation of oxide:

Rapid formation of an oxide scale is of importance to oxidation resistance of an alloy. The rapid formation of oxide scale could be promoted by heterogeneous nucleation of oxide at grain boundaries, and dispersed oxide particles in the substrate [78].

It was demonstrated that in initial stages of oxidation in Fe-16Cr, Fe-18Cr, and Fe-20Cr alloys containing various amounts of Ce as an alloying element and as a dispersed oxide phase accelerated the formation of oxide film through heterogeneous nucleation by providing extra nucleation sites [79, 80]. The Ce addition also affected the composition and microstructure of the formed oxide film.

The morphology of the formed oxide scale on the steels was affected by adding Ce and CeO₂. Fig. 1.5-1 illustrates the effect of Ce and CeO₂ additions on grain size of the oxide scale. The formation of a fine grained Cr₂O₃ scale was observed on surfaces of the Ce and CeO₂-containing alloys. The plasticity of an oxide increases usually with a decrease in the oxide grain size. Such a decrease in grain size may increase the ability of the oxide to absorb thermal shock and relax thermal stress. These effects are beneficial to the resistance of the oxide scale to failure and spallation.



a- Fe-16Cr, b- Fe-18Cr, c- Fe-20Cr. d- Fe-16Cr-0.1Ce, e- Fe-18Cr-0.1Ce, f- Fe-20Cr-0.1Ce
g- Fe-16Cr-0.1CeO₂, h- Fe-18Cr-0.1CeO₂, i- Fe-20Cr-0.1CeO₂

Figure 1.5-1. The effect of 0.1%Ce(CeO₂) on morphologies of oxide scales respectively on Fe-16Cr, Fe-18Cr, and Fe-20Cr after 70 h oxidation at 1000°C [80].

The overall performance of the Cr-containing alloys in terms of oxidation is improved when Ce is added to the alloys. Fig. 1.5-2 illustrates the effect of Ce and CeO₂ on the oxidation resistance of the Fe-Cr alloys.

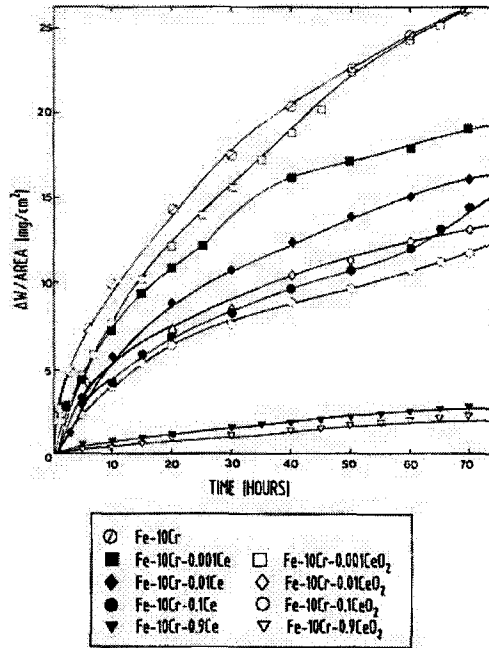


Figure 1.5-2. The effect of Cerium in both metal and oxide form on high-temperature oxidation of Fe-10Cr at 1000°C [80].

2. The effect of the rare-earth elements on the oxide growth

Although rare-earth elements increase the nucleation of oxide, they, however, reduce the oxide growth rate and thus the oxide thickness [75, 81].

There are several possible mechanisms responsible for the effect of rare-earth elements on the oxide growth:

1. *Blocking of atomic diffusion along grain boundaries*

The growth of oxide scale largely depends on atomic diffusion along grain boundaries. For instance, fast diffusion of chromium and aluminum along grain boundaries makes Cr/Al-containing alloys resistant to oxidation by forming a protective oxide scale such as Cr_2O_3 and Al_2O_3 . However, this diffusion will

continue through the oxide scale and promotes the growth of the scale. As a result, the scale is thickened, therefore cracking and spallation of the scale would be possible. When rare-earth elements, e.g., cerium and yttrium, are added to the alloys, these elements can segregate at the grain boundaries and in the form oxide particles of the reactive elements that can slow down atomic diffusion along grain boundaries [82-85].

Particles of CeO_2 , Y_2O_3 , YCrO_3 , and $\text{Y}_3\text{Al}_5\text{O}_{12}$ (YCrO_3 , and $\text{Y}_3\text{Al}_5\text{O}_{12}$ probably resulted from Y_2O_3 - Cr_2O_3 and Y_2O_3 - Al_2O_3 solid-solid reaction, respectively) were observed in the scale mainly at grain boundaries, as shown in Fig. 1.5-3.

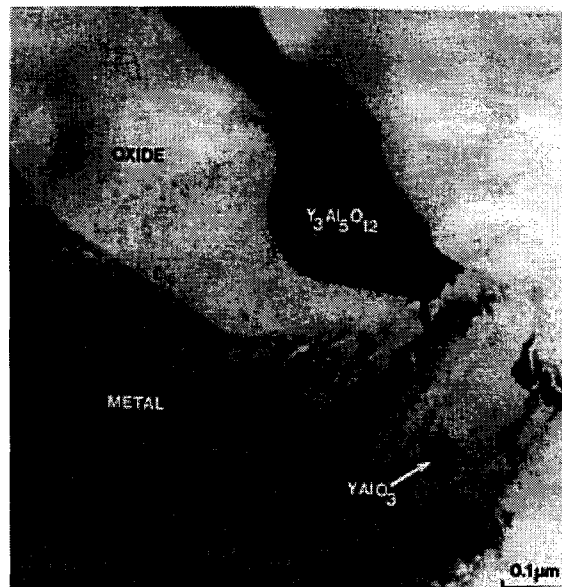


Figure 1.5-3. TEM micrograph taken in the vicinity of an oxide/metal interface which shows a $\text{Y}_3\text{Al}_5\text{O}_{12}$ particles in the oxide and a fine YAlO_3 particles in the metal [84].

It was suggested that when oxidizing at 1200°C, $YAlO_3$ particles in the alloys dissolve, and dissolved yttrium may diffuse along the metal/oxide interface and segregate at Al_2O_3 grain boundaries as the oxide grows into the metal.

Yttrium can react with Al_2O_3 and form $Y_3Al_5O_{12}$:

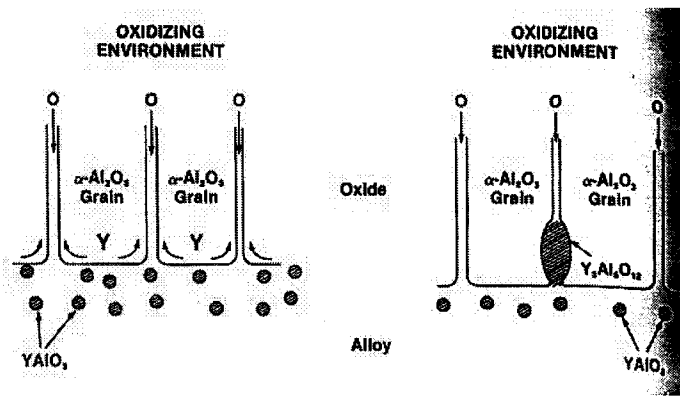
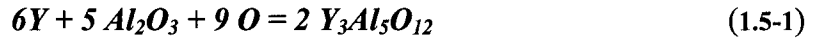


Figure 1.5-4. Mechanism for $Y_3Al_5O_{12}$ segregation at grain boundaries in Al_2O_3 oxide scale formed on an alumina-former alloy with Y_2O_3 [84].

It is suggested that grain growth and Al transport in Al_2O_3 are suppressed by $Y_3Al_5O_{12}$ particles. Fig. 1.5-4 illustrates the mechanism responsible for the formation of $Y_3Al_5O_{12}$ particles at grain boundaries.

A decreased oxidation rate will reduce oxidation, thus improving oxidation resistance of the material.

II. Effect of rare-earth elements on the oxide adherence

The rare-earth elements may enhance the metal/oxide adherence. It is known that failure of an oxide scale involves fracture through the thickness and along the metal/oxide interface as well. The failure or spallation of an oxide scale is assumed to occur when the stored elastic energy within a localized volume of oxide exceeds a critical value that is required to generate new surfaces by decohesion [86]. Rare-earth elements may improve the metal/oxide adherence in the following the possible ways:

(i) Reduction of oxide growth rate

The inhibition of oxide growth by rare-earth elements through blocking diffusion reduces the oxide thickness. A thinner oxide generates smaller mismatch strain energy and thus reduces the oxide spallation [86].

As mentioned earlier the reduction of atomic diffusion can reduce the oxide thickness. It is also suggested that dissolution of $Y_3Al_5O_{12}$ precipitates in Al_2O_3 may reduce the concentration of Al vacancies especially along grain boundaries [84, 87]. Calculation shows that there is strong bonding between Y ions and cation vacancies in Al_2O_3 [88], and this may lead to a change in the growth mechanism from outward growth mode to inward growth mode [89, 90], thus a further decrease in the oxidation growth rate.

(ii) Enhanced plasticity of oxide scale

As indicated earlier, rare-earth elements increase the nucleation rate for oxide development and result in fine grained oxide scale. Such a change in the oxide scale's microstructure helps to relax strain and thus decrease the oxide brittleness [84, 91, 92].

Previous studies have also demonstrated that rare-earth oxide particles segregating at grain boundaries, may increase the energy barrier to cracking and, hence, improve the strength and fracture toughness of the oxide scale [93].

(iii) Oxide pegging:

As a result of the internal oxidation of the reactive alloying additions, oxide intrusions form and extend into the substrate. This provides mechanical keying of the oxide to the alloy substrate and thus improves the interfacial bonding. Fig 1.5-5 shows scanning electron microscope (SEM) images of formed oxide pegs on Hf-containing Fe-Al alloy. The formation of such oxide pegs has been reported by many researchers [81, 94-101].

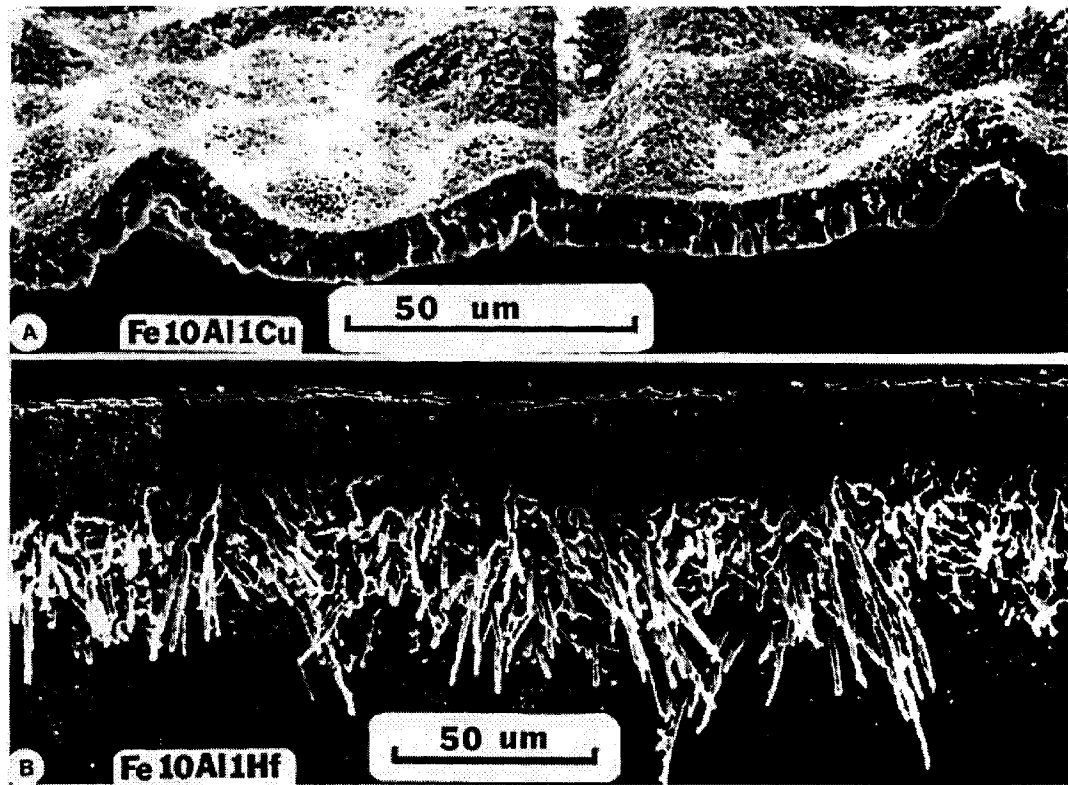


Figure 1.5-5. Effect of RE additions on formation of inwardly growing pegs in Al_2O_3 scale: (A) detached scale formed on Fe-10Al-1Cu alloy. (B) deeply etched section of the tenacious scale formed on Fe-10Al-1Hf alloy, showing micro-pegs [81].

The development of the micro-pegs could be assisted by oxygen short-circuit diffusion along the rare-earth elements oxide particles. For instance, Al_2O_3 grows very slowly in to the substrate and almost any addition might increase its growth rate. Therefore, oxygen may migrate faster along the oxide/substrate interface, leading to the growth of oxide pegs [81].

Micro-pegs may enhance the interfacial adhesion in the following possible ways [102]:

- 1) Providing intimate contact between the oxide scale and the alloy substrate.
- 2) Acting as a graded layer; the layer mixing the oxide pegs and the substrate would help to accommodate interfacial stress from the lattice mismatch, which is harmful to the interfacial bond.
- 3) Improving the fracture toughness of the interfacial region by blocking interfacial crack propagation.

(iv) Provision of vacancy sink:

Additions of rare-earth elements and their oxides could provide alternative sites for vacancy condensation during oxidation and thus reduce void formation at the oxide/alloy interface and consequent separation of the oxide from the substrate [81, 95, 101].

The supply of interfacial vacancies arises mainly from outward diffusion of cations within the scale, especially during early stages of oxidation when the faster growing base metal oxide occurs at elevated temperatures. In addition, unequal fluxes of different alloy components in the substrate can give a net flow of vacancies to the alloy substrate [103].

The vacancy is detrimental to the oxide adherence. For example, during the oxidation of a Fe-25Cr-4Al alloy, the spallation of the protective oxide from the

substrate was found as a result of void presence in the vicinity of the oxide/Alloy interface [95]. Fig. 1.5-6 schematically illustrates the mechanism for oxide failure as a result of the existence of voids at the interface.

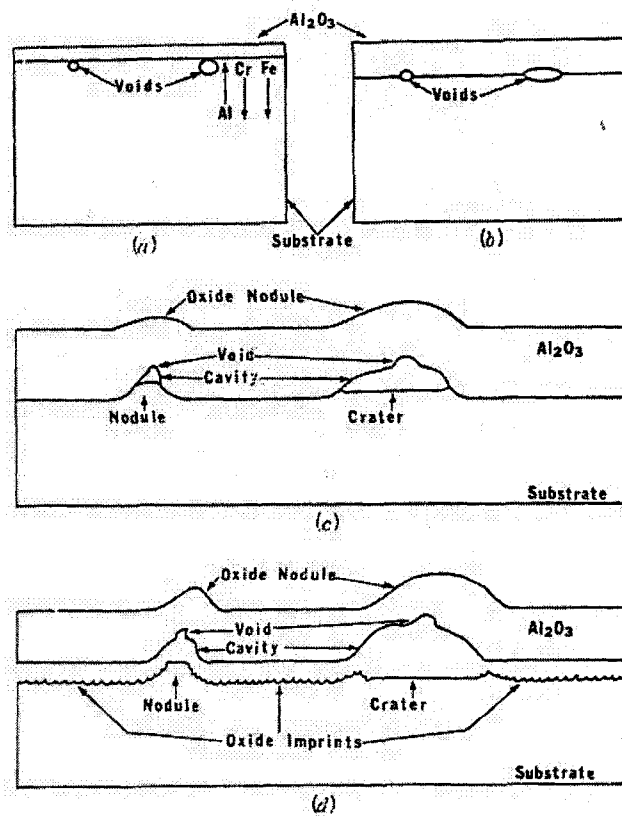


Figure 1.5-6. A proposed mechanism responsible for oxide spallation as a result of the existence of voids at interface [95].

It has been demonstrated that the rare earths or reactive elements can minimize the development of voids at the oxide/substrate interface [95, 101, 103]. Fig. 1.5-7 Illustrates morphologies of substrate surfaces after oxide scales were

removed. One may see that alloyed Yttrium reduced interfacial voids (Fig. 1.5-7b), in contrast with the one without Yttrium (Fig. 1.5-7a).

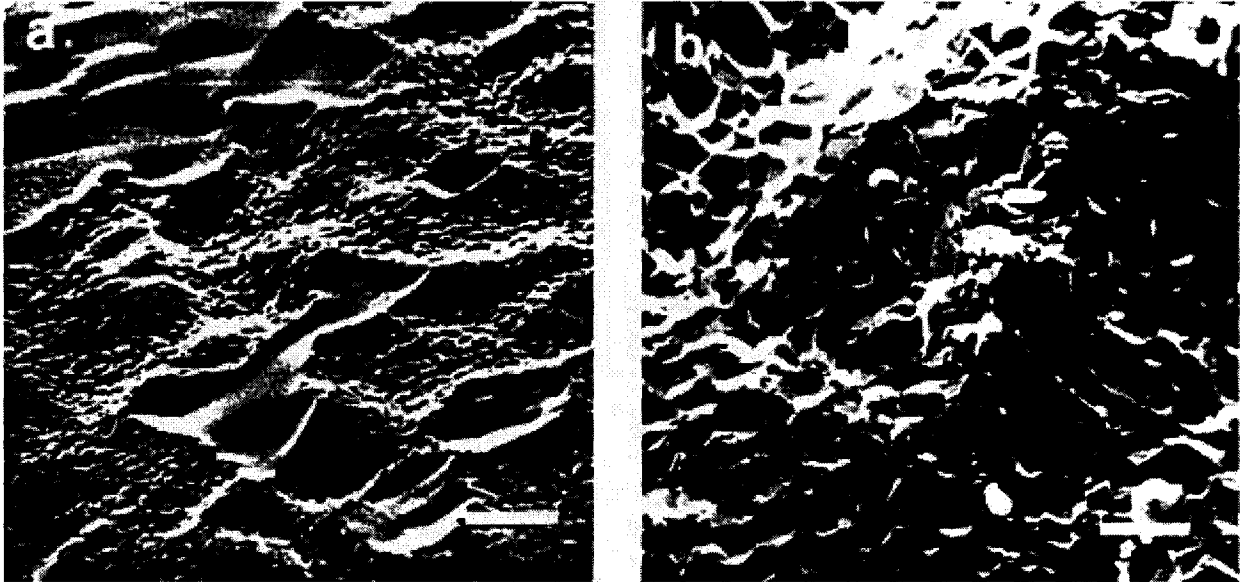


Figure 1.5-7 Surfaces of Co-base alloy (imprint-free, completely imprinted) after removal of its surface oxide scale: a) without Yttrium, b) with Yttrium [104].

The reduction of interfacial voids by rare earth elements can be attributed to the following [104]:

- 1) Formation of vacancy sinks at the surface of rare-earth rich inter-metallic precipitate, internal oxides, or stable oxides dispersoids.
- 2) Modification of scale initiation processes by rapidly suppressing the base metal oxidation.

1.5.2 Effect of rare-earth elements on corrosion resistance

Rare earth elements (RE) have also found applications in resisting aqueous corrosion. Since the early 1930's, studies have been conducted to evaluate effects of RE on corrosion [105]. For instance, in 1972, Russian workers observed that neodymium (Nd) markedly reduced the corrosion rate of magnesium (Mg) [106]. Some magnesium alloys containing rare-earth elements have been available in a market whose corrosion performance is equal to, or better than, high-strength Al alloys [107]. As shown Fig. 1.5-8, corrosion rate was decreased when rare-earth elements were alloyed with the magnesium.

Various rare-earth salts such as YCl_3 , $LaCl_3$ and $CeCl_3$, were found beneficial to alloys when added to aggressive media as corrosion inhibitors [108-115]. It has been demonstrated that corrosion of aluminum alloy [113-115], mild steel [116], and zinc [111] in aqueous chloride solution (0.1N NaCl) were reduced when RE cations are present as Fig. 1.5-9 illustrates. The beneficial effect of RE cations on corrosion behavior of 1045 and 304 steels was also observed [110].

This function of inhibiting aqueous corrosion is attributed to the formation of a hydrated RE oxide film on the metal surface. The hydrated rare earth oxide film may act as a barrier between the corrosive solution and the alloy, thus protecting the material from corrosion.

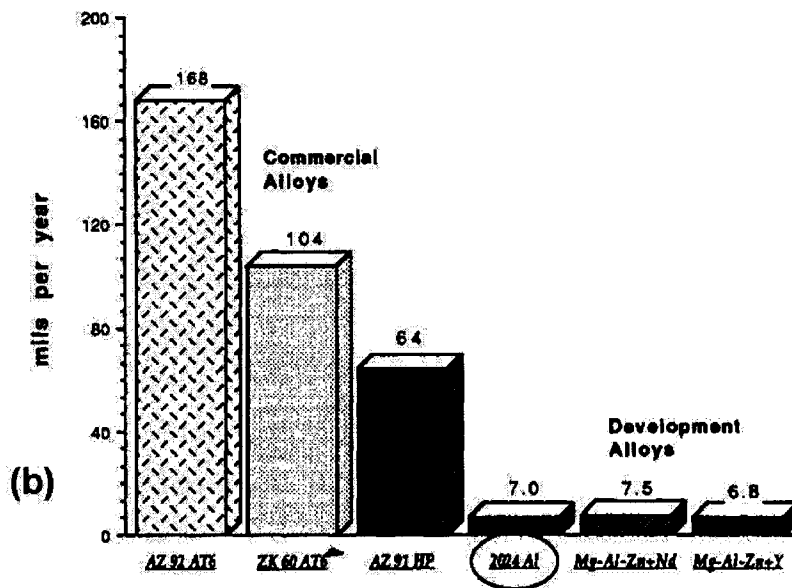
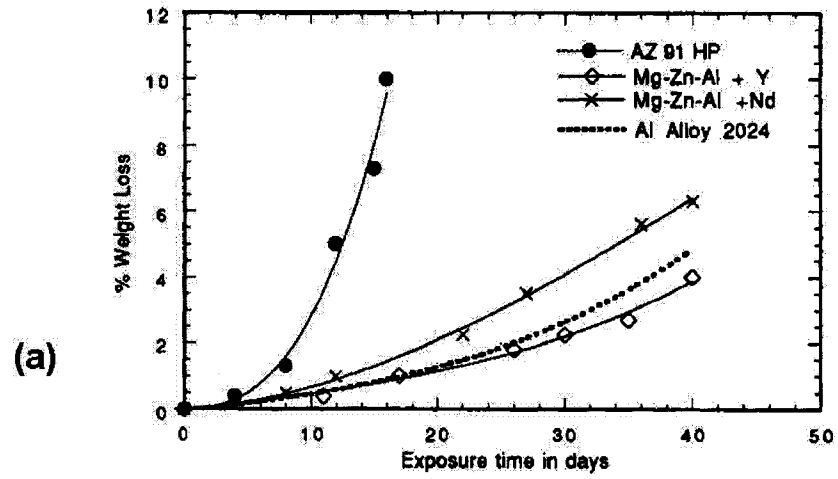


Figure 1.5-8. Rates of corrosion of wrought Mg and RE-containing Mg alloys NaCl compared to that of 2024 Al alloy [107].

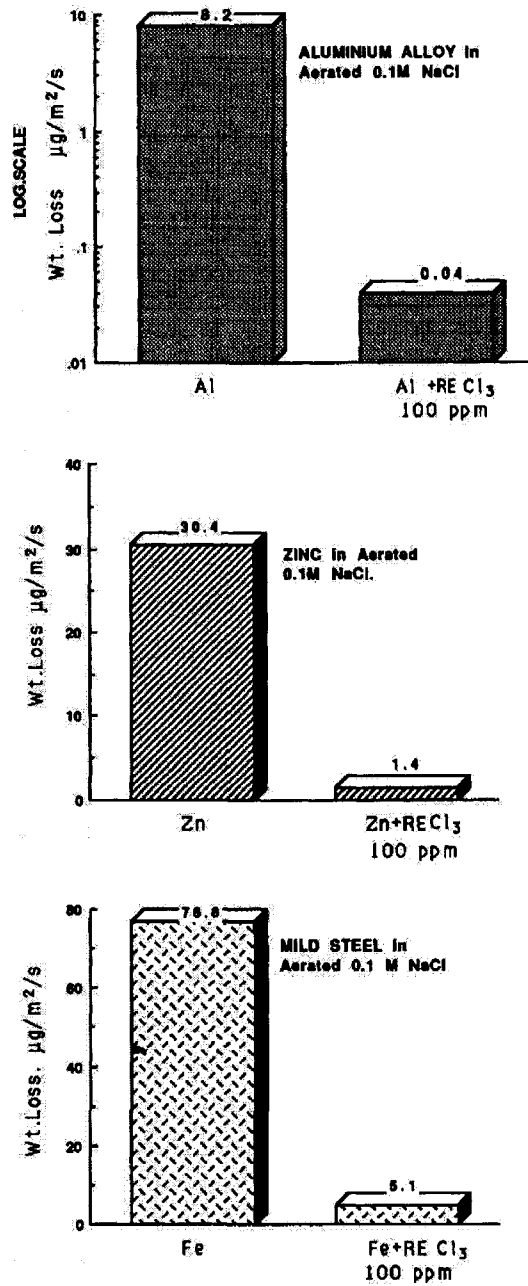


Figure 1.5-9. Inhibition of corrosion of (a) aluminum 7075 alloy, (b) zinc and (c) mild-steel in aerated 0.1 N NaCl with 100 ppm mixed rare-earth chloride[117].

The formation of a protective film can result in changes in surface electrochemical and mechanical properties. It was demonstrated that additions of rare-earth elements could improve the polarization behavior of aluminum in a 0.1M HNO₃ solution [28], Fig. 1.5-10 shows potentiodynamic polarization curves of Y/Y₂O₃-Containing Aluminum, pure Aluminum, and 6061 Aluminum alloy. As illustrated, both the cathodic and anodic arms of the polarization curves of the Y/Y₂O₃-Containing Aluminum were shifted to lower current densities, which mean that the corrosion resistance was improved. Rare-earth elements have similar effects on polarization behavior of stainless steel [118]. Fig. 1.5-11 illustrates the improvement in the polarization behavior of stainless steel in a 0.1M H₂SO₄ solution.

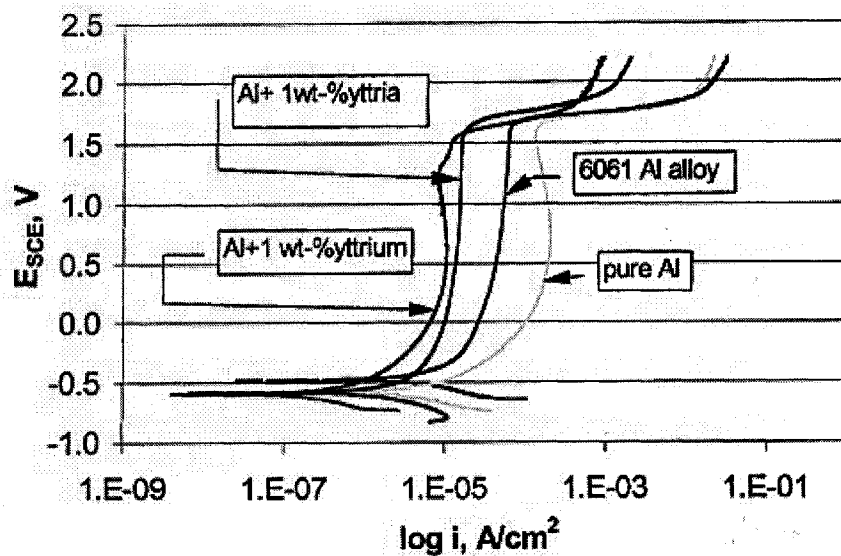


Figure 1.5-10. Potentiodynamic polarization curve of different aluminum alloys in a 0.1M HNO₃ solution [28].

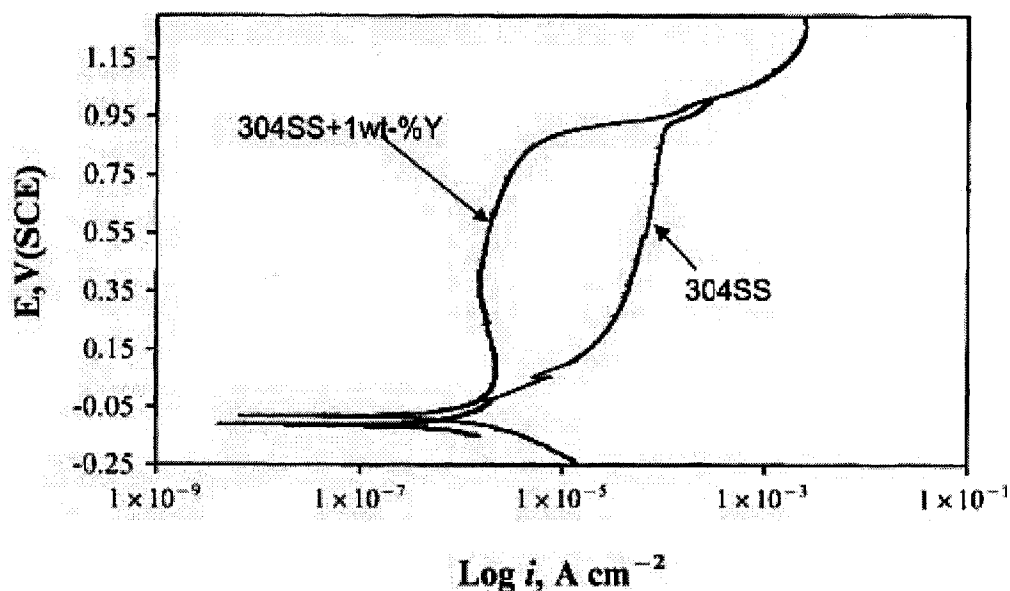


Figure 1.5-11. Potentiodynamic polarization curves of 304 Stainless Steel, with and without Yttrium [118].

Inhibition of aqueous corrosion is achieved when anodic and cathodic reactions or any of the partial reactions are decreased. The polarization behavior is certainly a good indication of the beneficial effect of RE on the corrosion resistance.

1.5.3 Effects of rare-earth elements on corrosive wear

It is well known that the synergism of corrosion and wear can result in a significant increase in material loss. Recent studies [119-123] have shown that RE can considerably enhance the corrosive wear resistance. The situation is similar in

the case of high-temperature wear of stallite 6 alloy [124]. When the oxidation is suppressed by RE, the synergism of wear and oxidation is diminished, thus leading to lower wear rate.

It was demonstrated that 1wt% alloyed Yttrium markedly improved the resistance of 304 stainless steel to corrosive wear [121], Fig. 1.5-12 illustrates corrosive wear of 304 stainless steel in a 0.1M H₂SO₄ solution.

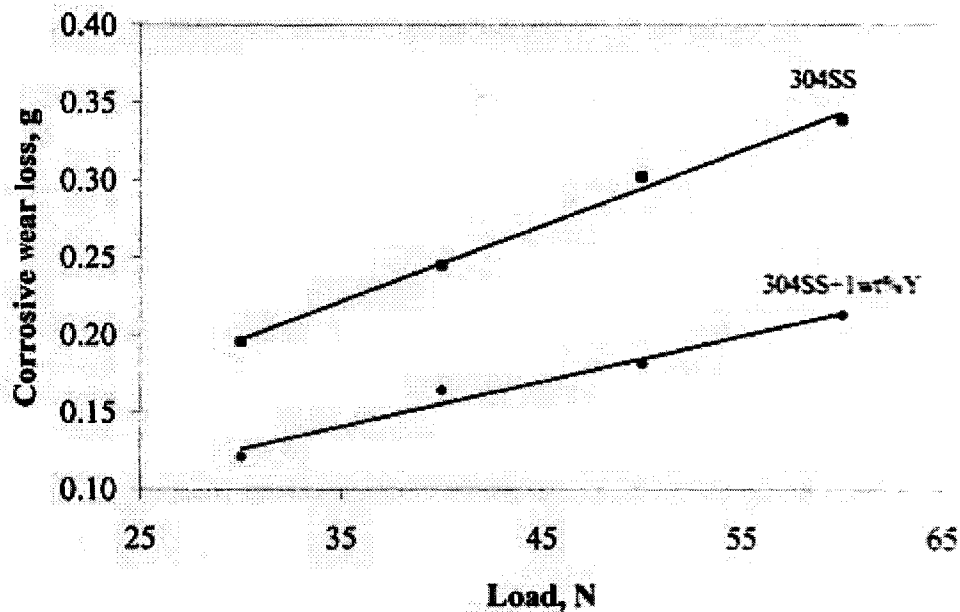


Figure 1.5-12 Variation in wear loss in 0.1M H₂SO₄ solution with respect to applied load: sliding speed 0.59 m/s, sliding distance 1000 m [121].

Scanning electron microscopy (SEM) observation demonstrated that microcracking occurred in the surface layer of Y-Free 304 stainless steel but did not occur in Y-Containing 304 stainless steel when worn in the 0.1M H₂SO₄ solution (see Fig. 1.5-13).

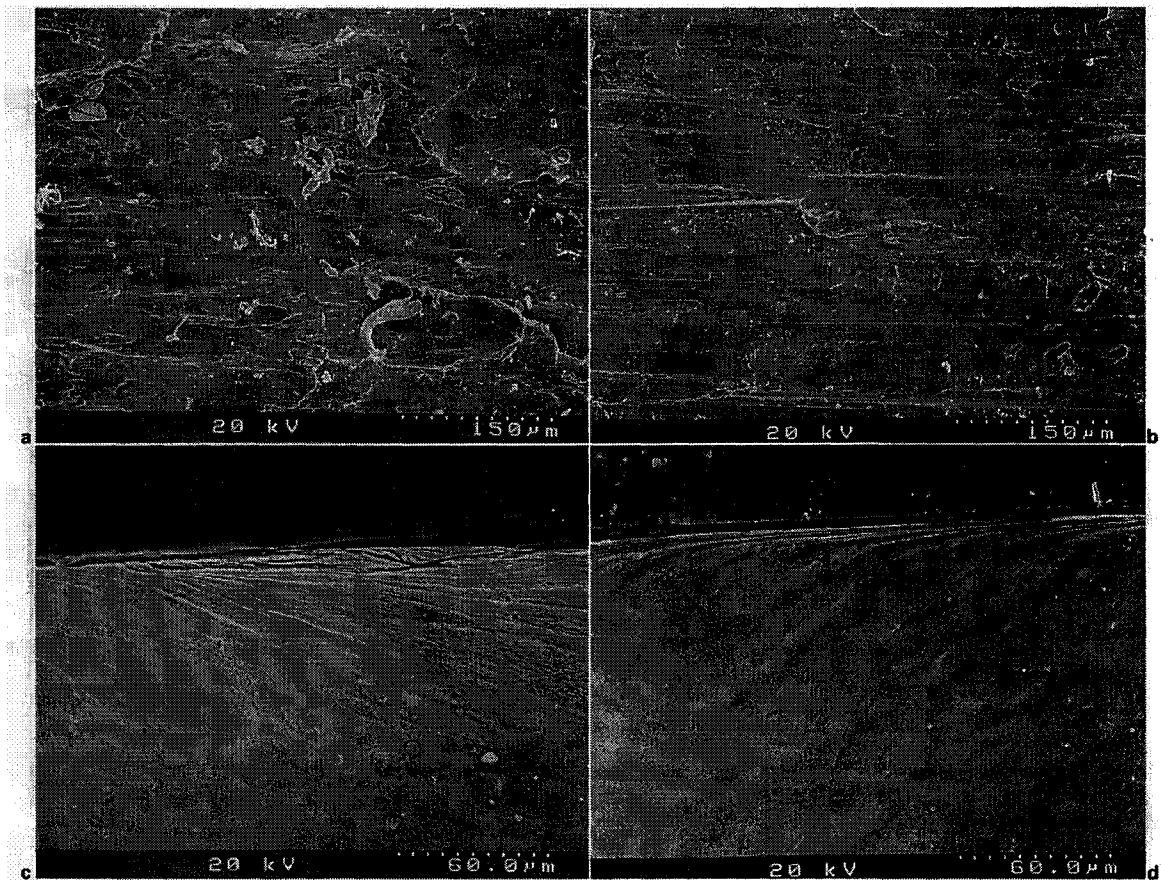


Figure 1.5-13 (a) 304 stainless steel; (b) 304 stainless steel containing 1 wt%. %Y; (c) cross-section of a worn 304 stainless steel sample; (d) cross-section of a 304 stainless steel sample containing 1wt. %Y [121].

Fig. 1.5-14 illustrates corrosive wear of pure Al, Al-1wt%Y, Al-1wt%Y₂O₃ and 6061 Al alloy in a 0.1M H₂SO₄ solution. The beneficial effect of Yttrium was clearly demonstrated.

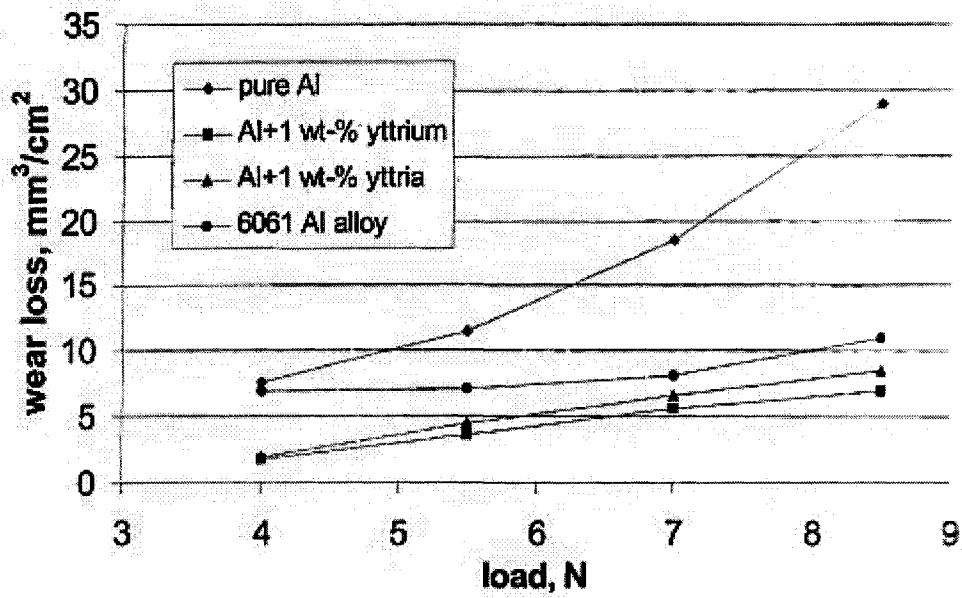


Figure 1.5-14 Variation of corrosive wear rate of materials in 0.1M HNO₃ Solution [28].

The beneficial effect of RE on corrosive wear of stainless steel and aluminum alloys could largely result from the improvement in their passive films. As illustrated in Fig. 1.5-15, alloyed Yttrium markedly increased the resistance of 304 stainless steel to corrosive erosion in a slurry of 0.1M H₂SO₄ containing 30%SiO₂ sand [119]. However, when the velocity of the slurry, relative to the sample, exceeded a certain value, there was almost no difference between Y-Free and Y-Containing samples. This implies that the main beneficial role that Yttrium plays is to improve the passive film, since at high slurry velocities, passive film may not form and thus no difference in corrosive erosion behavior between Y-Free and Y-Containing samples was observed.

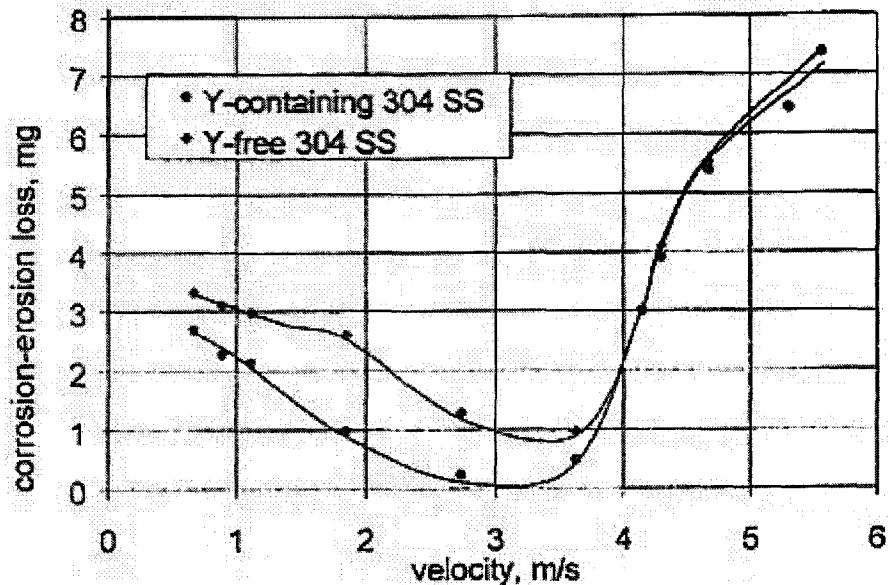


Figure 1.5-15 Variation in corrosion-erosion loss versus the velocity for Y-free and Y-containing 304 Stainless Steel in 0.1M H₂SO₄ slurry Containing 30% silica sand [119].

Further studies on the effect of RE on passive film demonstrated that:

- 1) The chemical stability of the passive film on stainless steel was higher when RE was alloyed to the steel, which has been confirmed by its increased surface electron work function, shown in Fig. 1.5-16 [44].
- 2) Mechanical properties of the passive film were improved, evaluated using a Nano-Mechanical Probe as Fig 1.5-17 illustrates [44].

3) The scratch resistance of the passive film was improved, evaluated using a microscratch tester with capability of monitoring changes in the electrical contact resistance as Fig. 1.5-18 illustrates [44].

A passive film with improved mechanical properties and chemical stability would lead to higher resistance to corrosion and corrosive wear.

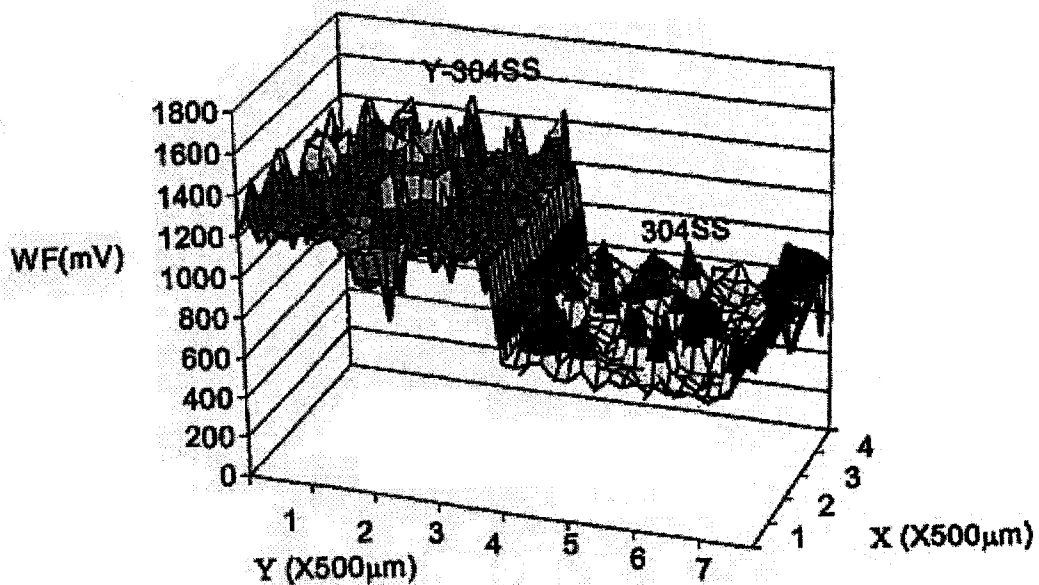


Figure 1.5-16 Electron work function of Y-free and Y-containing 304 Stainless steel After passivation treatment in 3.5 % HNO_3 solution for 12 h (X and Y are spatial axes) [44].

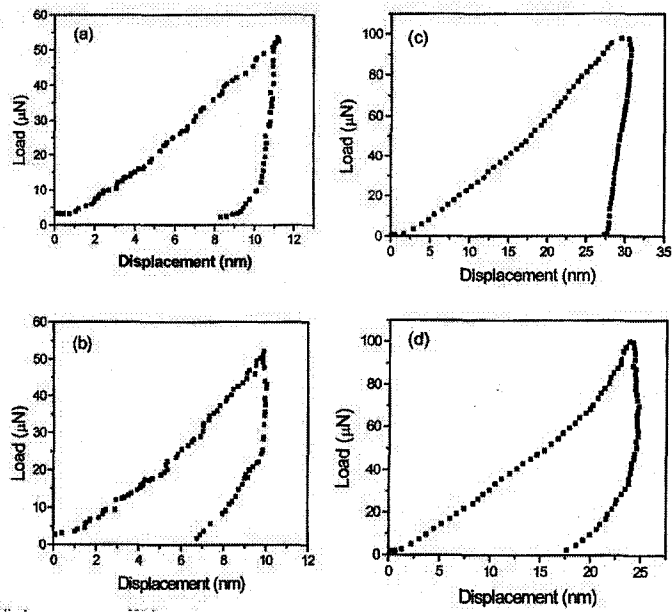


Figure 1.5-17 Load-displacement curves of Y-free and Y-containing 304 stainless steel samples passivated in 3.5% HNO₃ solution: (a) 304 stainless steel (0-50µm); (b) Y-containing 304 stainless steel (0-50µm); (c) 304 stainless steel (0-100µm); (d) Y-containing 304 stainless steel (0-100µm) [44].

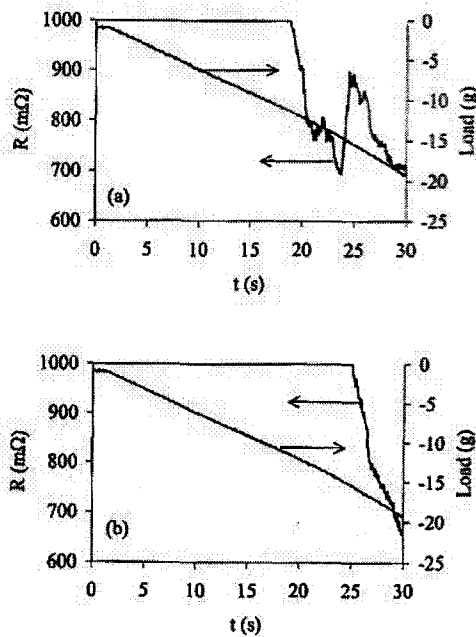


Figure 1.5-18 Changes in electrical contact resistance after passivation treatment in 3.5% HNO₃ solution: (a) Y-free 304 stainless steel (b) Y-containing 304 stainless steel [44].

In summary, it is clear that the addition of rare-earth elements (RE) can inhibit the synergistic action of wear and corrosion and thus diminishing the corrosive wear of materials. The improvement in the passive film has large contribution to the increase in the resistance to corrosion and corrosive wear.

In additions to rare-earth elements, it was also observed that rare-earth compounds such as Y_2O_3 also improved the resistance of aluminum to corrosion and corrosive wear [125]. It was reported that the rare-earth compounds were also beneficial to the oxide adherence [75, 78-81]. However, whether or not the rare-earth compounds can improve the resistance to corrosion and corrosive wear has not been well investigated.

The objective of this work is to investigate effects of Y_2O_3 particles in aluminum on the performance of the metal during corrosion, corrosive wear and mechanical wear. This study is oriented to fundamental understanding of the effect of Y_2O_3 on corrosion and corrosive wear of aluminum and aluminum alloys, and also for potential application of rare earth compounds against corrosive wear in aggressive environments.

Since Yttrium is active and hard to handle during material processing. The application of inexpensive Y_2O_3 particles could be more feasible and economical.

2 Microstructure of Aluminum Modified with Y_2O_3 Addition

As mentioned earlier, rare-earth elements are beneficial to the resistance of alloys to corrosion and corrosive wear. However, these elements are expensive and hard to handle due to their high reactivity.

The objective of the present research is to explore potential application of rare-earth compounds in increasing corrosive wear resistance. A sample, Y_2O_3 was chosen for this study.

This chapter reports results of investigation on microstructure of Y_2O_3 -containing aluminum made using an arc melting furnace, employing optical microscopy (OM), scanning electron microscopy (SEM), energy dispersive x-ray spectroscopy (EDX) and X-ray diffraction (XRD).

2.1 Material and sample preparation

Commercial pure aluminum powder (99.8%) with particle size from -40 to +325 Mesh (420 to 44 μ m) was used to make the samples, respectively containing 0, 5, 10, and 20 wt.% Y_2O_3 powder (Nominal). The Y_2O_3 powder had its particle size smaller than 10 μ m.

During sample preparation, Al and Y_2O_3 powders were mixed in a plastic bottle with a size of 60 mm in diameter and 120 mm in height. A number of alumina milling

balls were put into the bottle to prevent any agglomeration of the Y_2O_3 particles and to ensure a homogenous powder's mixture. The bottle was rotated at a speed of 155 rpm on a mill apparatus in air for 10 hours.

The mixed powder was then loaded into a tool steel compaction die having a size of 1" in diameter (25.4mm diameter). The die's wall and punches were lubricated using mould release spray before the powder was loaded into it for easy removal of a sample from the die after compaction. A Carver laboratory press machine was used to press the die under a compaction load of 11 tons, (~24,000 Lbs). The die was kept under the compaction load for 5 minutes, as illustrated in Fig. 2.1-1.

A pressed sample was then melted in a STERM water cooled arc-melting furnace. Inside the melting chamber of the furnace there is a copper hearth and a stainless steel bell jar. The gas inlet and outlet valves were mounted in the bell jar to let argon gas flow in the melting chamber. The copper hearth was water cooled by allowing the water run through it. A glass view port was made on the bell jar for monitoring the melting process.

The electrode was made of tungsten. The melting electrode was inserted from the bell jar's top which was used to move it forward and backward using a moving arm to ensure melting of the whole sample. The moving arm was also water cooled to prevent overheating.

Before melting, the furnace was evacuated down to 5×10^{-2} Torr and then filled with argon gas to a pressure of 1 atm. Such a process was repeated three times to ensure a proper argon environment in the furnace. A continuous argon gas flow was maintained at a rate of 2 l/min during the melting and cooling processes. All samples were turned over, remelted and cooled for four times in order to reduce compositional inhomogeneity. All samples had dimensions of $10 \times 10 \times 30$ mm.

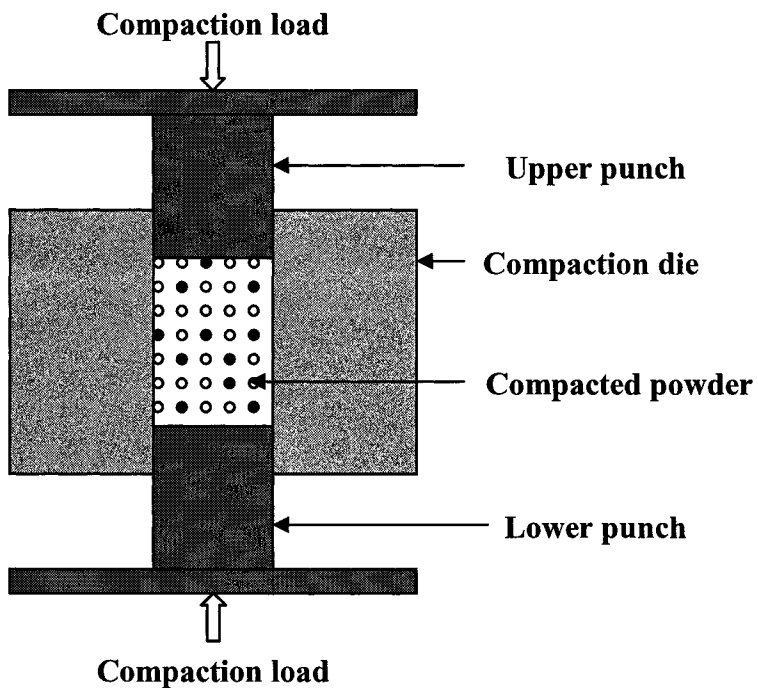


Figure 2.1-1. Schematic of the apparatus for powder compaction.

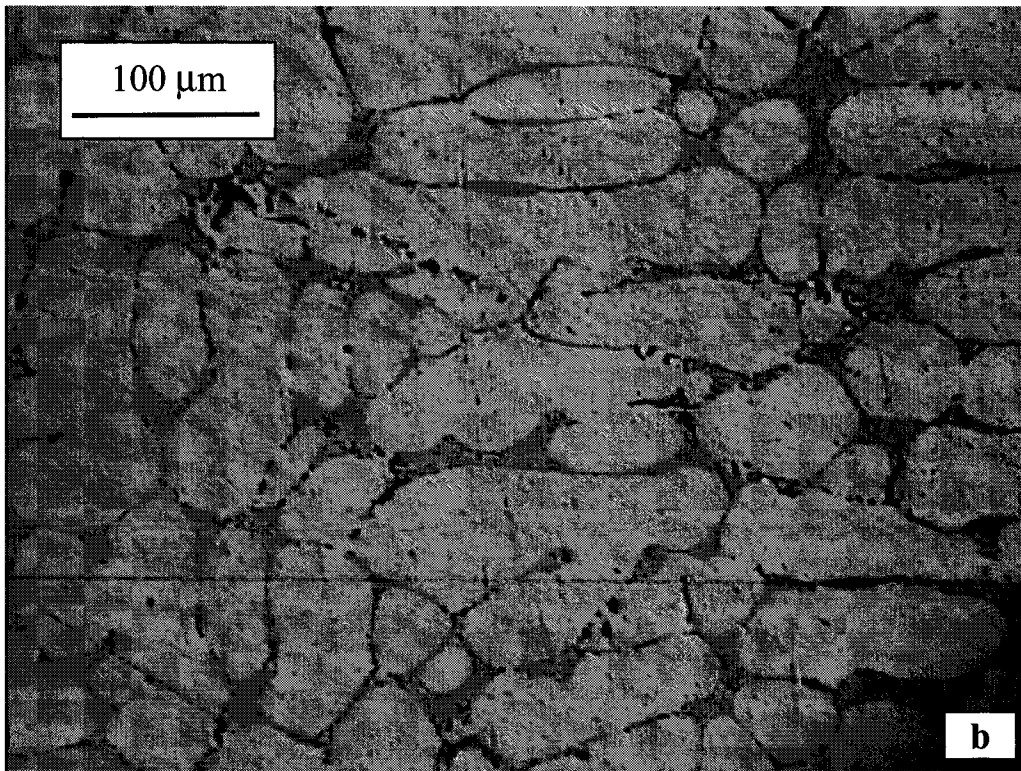
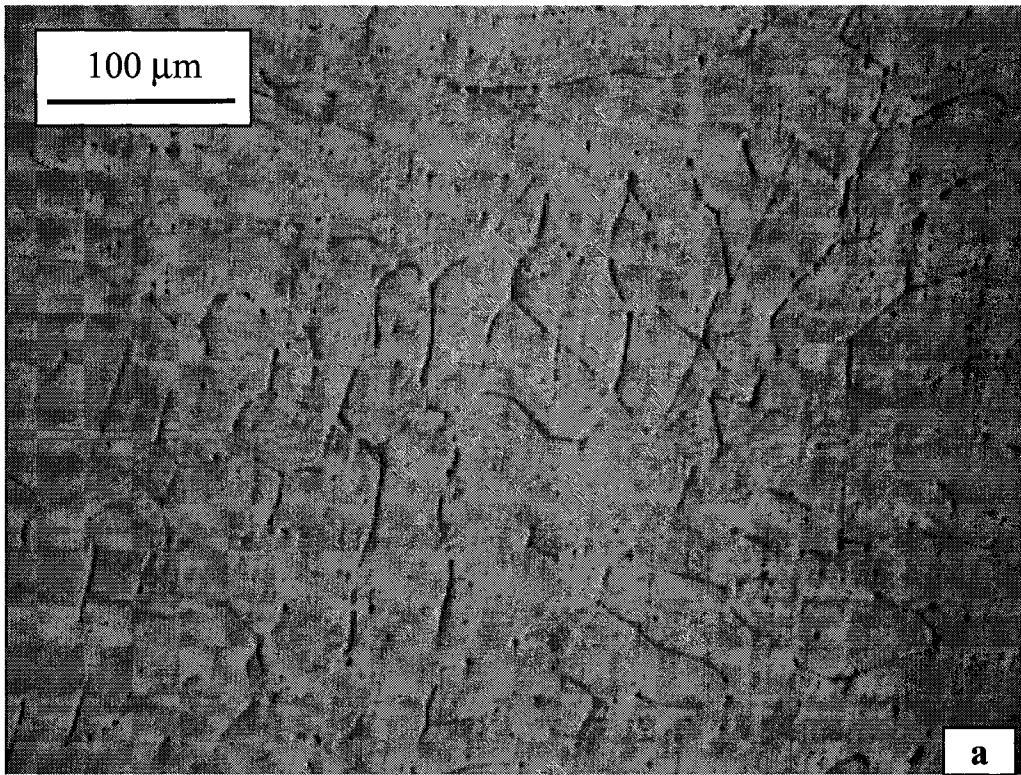
The samples were then kept in an Ar-protected tube furnace at 630° C for 1 hour to further reduce the microstructural inhomogeneity; the samples were cooled in the furnace.

2.2 Microstructural observation and phase analysis

2.2.1 Optical microscopy (OM), scanning electron microscopy (SEM), and energy dispersive spectroscopy (EDX) analysis:

For microstructural examination, Y₂O₃-free Al and Y₂O₃-containing Al samples were cut from the annealed cast using an ISOMET 2000 linear precision cooled saw. The samples having dimensions of 5×10×10 mm were mounted in epoxy resin, polished to 0.05μm (roughness) and etched for 1 minute using a *Keller's reagent* (2mL HF (48%), 3mL HCl (con), 5mL HNO₃ (con), 190mL water).

Microstructure of the samples was observed under an optical microscope and obtained metallographs are shown in Fig. 2.2-1, for aluminum samples with (a) 0wt%Y₂O₃, (b) 5wt% Y₂O₃, (c) 10wt% Y₂O₃, and (d) 20wt% Y₂O₃, added respectively. Unexpectedly, dispersed Y₂O₃ particles were not observed in the aluminum matrix. Instead, eutectic microstructure was observed as shown in Fig. 2.2-1. The added Y₂O₃ made the microstructure finer, although original Y₂O₃ particles were not retained. The samples with 5wt% Y₂O₃ and 10wt% Y₂O₃ added showed a microstructure consisting of aluminum dendrites and an eutectic mixture containing aluminum and an Y-rich phase. When the fraction of Y₂O₃ was increased to 20wt%, Y-rich phase grew and appeared as dispersed particles as Fig. 2.2-1 (d) illustrates.



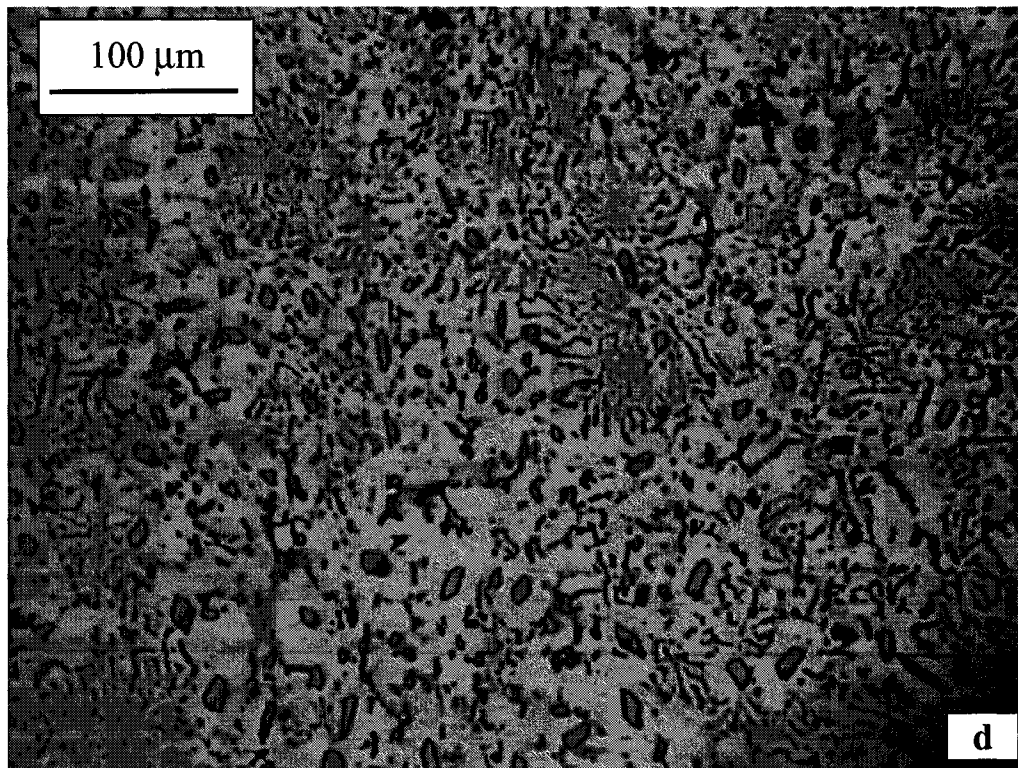
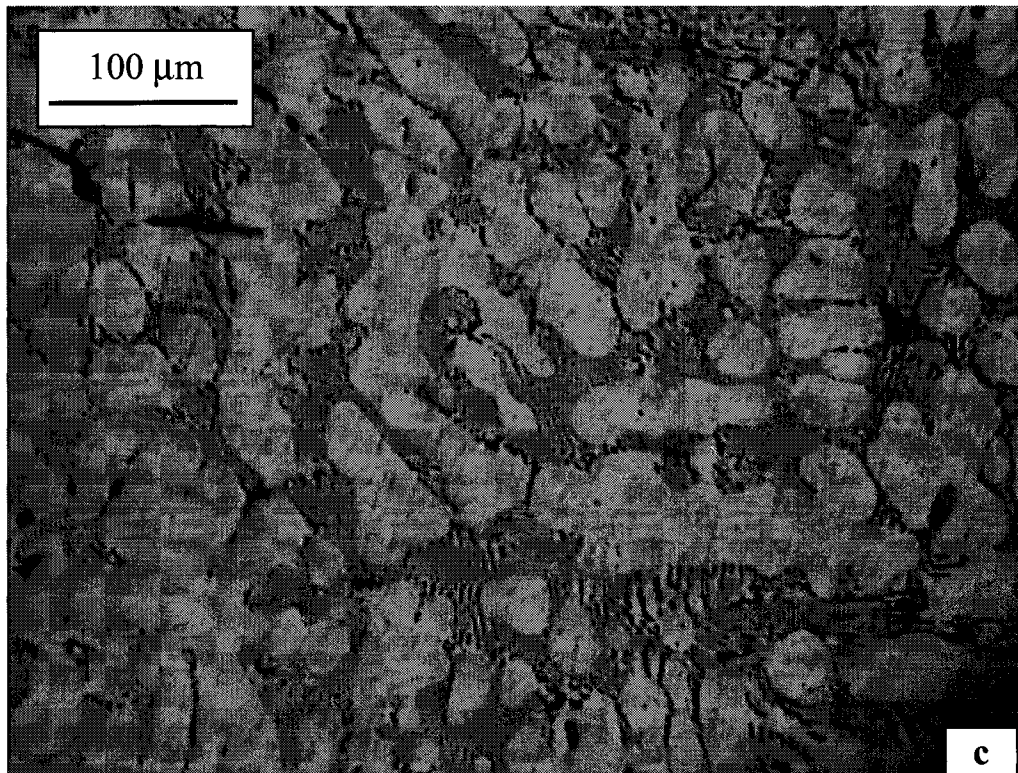


Figure 2.2-1. Optical microscopy images; (a) Y_2O_3 -free Al, (b) 5wt% Y_2O_3 -containing Al, (c) 10wt% Y_2O_3 -containing Al, (d) 20wt% Y_2O_3 -containing Al.

In order to take a closer look at the microstructures, SEM and EDX were used to examine 5, 10, 20wt% Y_2O_3 -containing Al samples using a PGT PRISM SEM/EDX system.

Fig. 2.2-2 illustrates backscattered electron images of (a) 5wt% Y_2O_3 , (b) 10wt% Y_2O_3 , and (c) 20wt% Y_2O_3 , respectively. Fig. 2.2-3 illustrates EDX peaks from which compositions of different samples were determined. It was demonstrated that the dendritic arms, i.e. the dark domains in the 5 and 10wt% Y_2O_3 -containing Al samples, were pure aluminum, while the bright areas had 57.96wt% Y. The bright phase in the 20wt% Y_2O_3 -containing Al samples had a composition of 58.4 wt% Y. The compositions of various domains in different samples are given in Table 2.2-1.

It should be pointed out that there was no any indication of the presence of oxygen in the samples, which implies that the Y_2O_3 particles could be melted or decomposed during the melting process.

In order to confirm this hypothesis, X-ray diffraction (XRD) was employed to determine phases in Y_2O_3 -containing Al samples. Results of XRD analysis are presented with discussion in the following section.

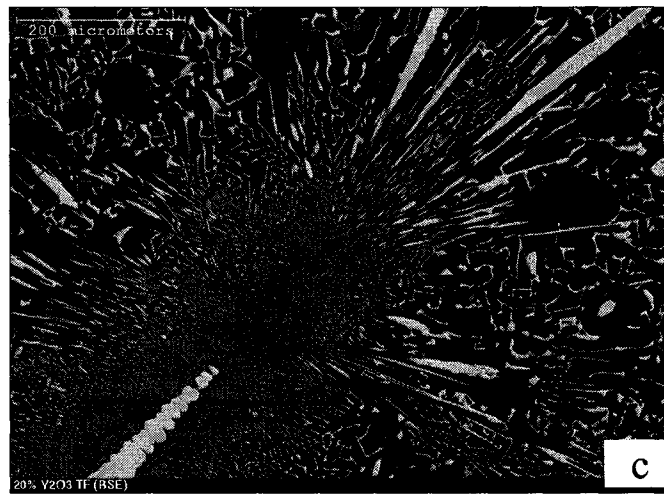
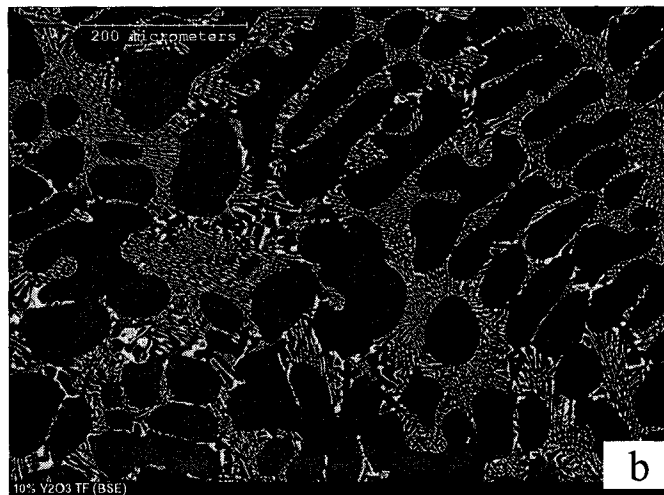
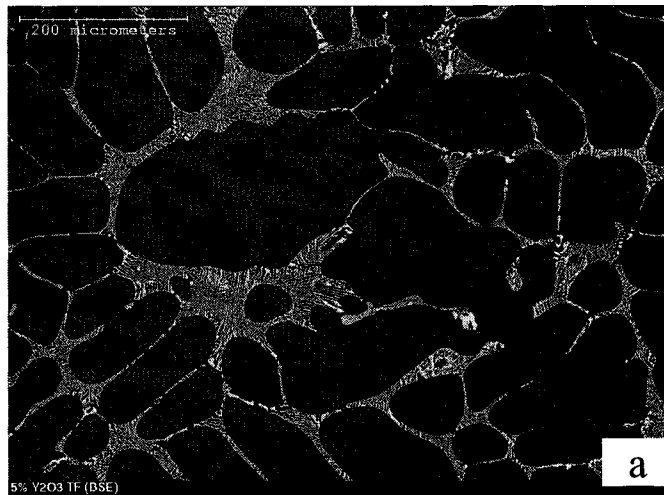
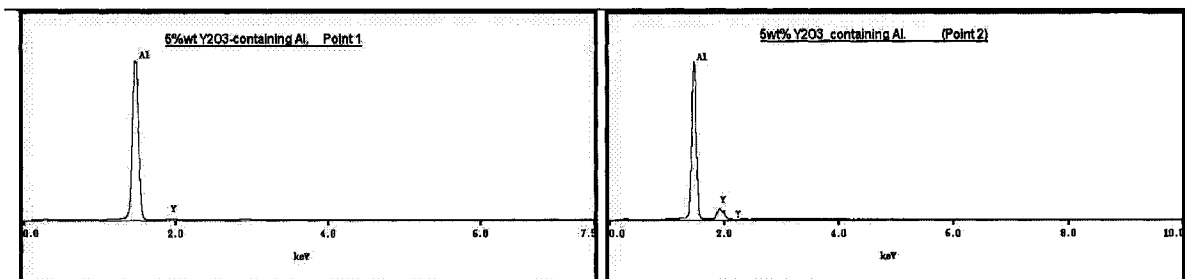
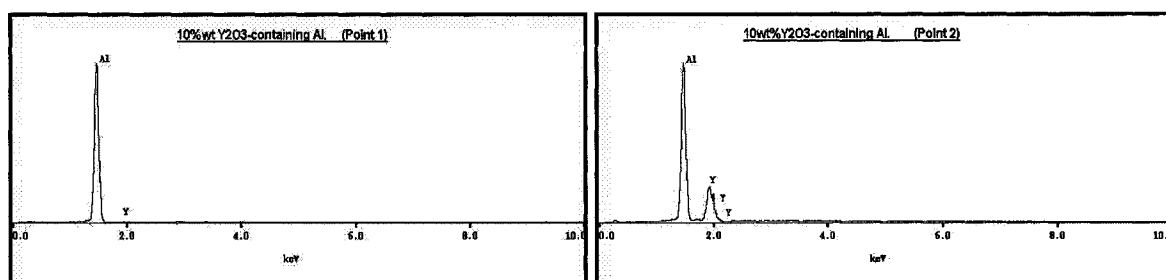


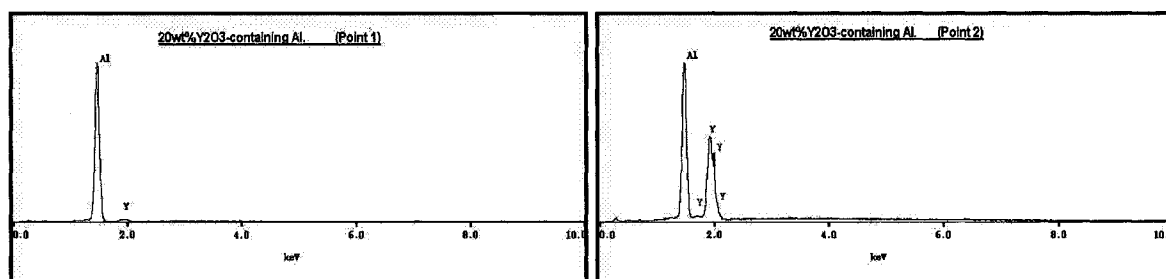
Figure 2.2-2. SEM backscattered electron images of: (a) 5wt% Y_2O_3 -containing Al, (b) 10wt% Y_2O_3 containing Al, and (c) 20wt% Y_2O_3 -containing



(a)



(b)



(c)

Figure 2.2-3. EDX analysis for different spots illustrated in *Fig. 2.2-2*; (a) 5wt% Y_2O_3 -containing Al, (b) 10wt% Y_2O_3 -containing Al, (c) Y_2O_3 -containing Al.

Table 2.2-1 Chemical composition of 0, 5, 10, and 20wt%Y₂O₃-containing Al samples.

Material	Overall Composition (Wt%)			Dark Domain Composition (Wt%)		Bright Domain Composition (Wt%)	
	Al	Y	Si	Al	Y	Al	Y
0wt% Y ₂ O ₃	100	0.0	0.0	N.A	N.A	N.A	N.A
5wt% Y ₂ O ₃	97.2	2.8	0.0	100	0	42	58
10wt% Y ₂ O ₃	93.1	6.9	0.0	100	0	41.6	58.4
20wt% Y ₂ O ₃	84.2	15.8	0.0	100	0	41	59

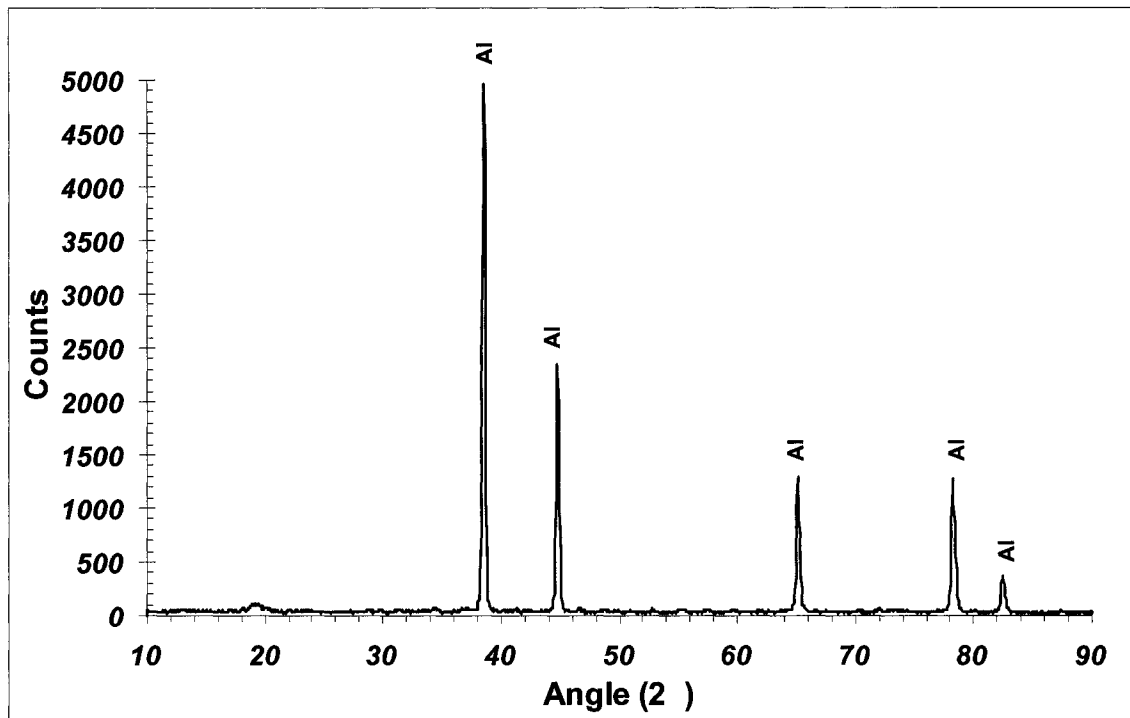
2.2.2 X-ray diffraction (XRD) analysis

The Y₂O₃-free aluminum and Y₂O₃-containing aluminum samples were analyzed using a Rigaku Geigerflex X-ray diffractometer. Before XRD analysis, all samples were ground and collected powder had an approximate particle size of 1mm. The X-ray patterns of Y₂O₃-free, 5wt%, 10wt%, and 20wt% Y₂O₃-containing Al samples were obtained and shown in Fig. 2.2-4a, b, c and d, respectively. As illustrated in Fig. 2.2-4a, the Y₂O₃-free Al sample only showed peaks of pure aluminum.

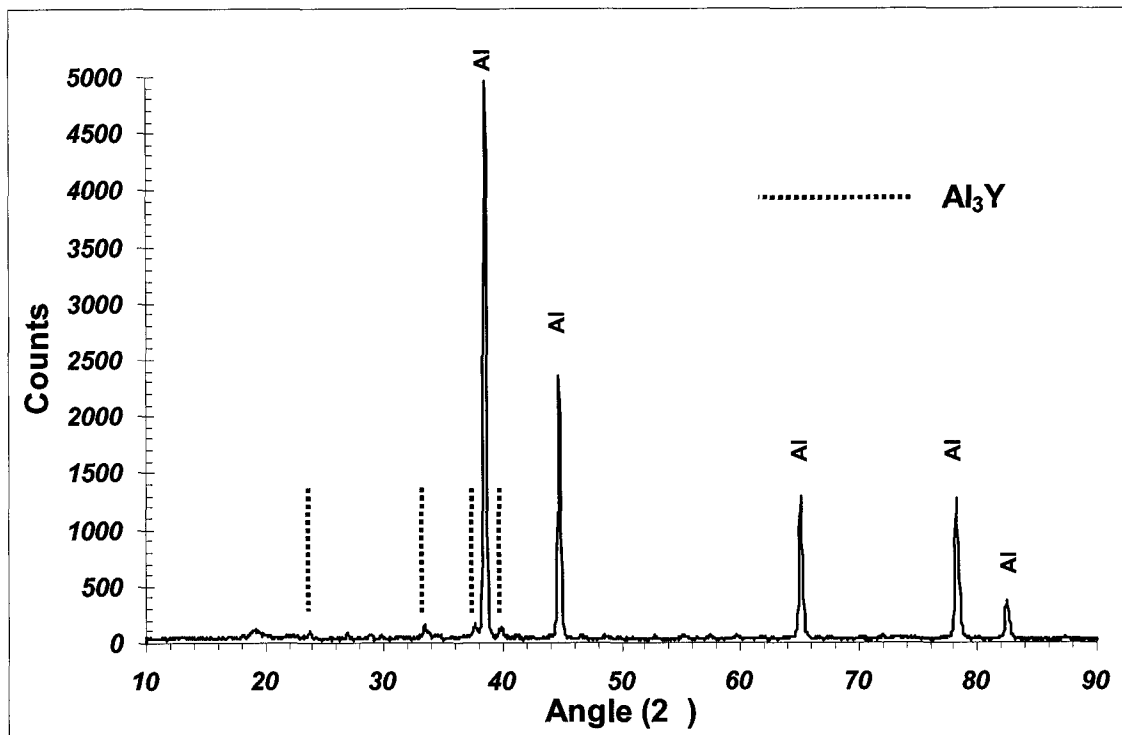
In Fig. 2.2-4b, c, and d, which illustrate XRD pattern of samples containing 5, 10, and 20wt%Y₂O₃, new peaks were observed. The new peaks were identified to come from

Al_3Y intermetallic compound. No Y_2O_3 peaks were identified for 5wt%, 10wt%, and 20wt% Y_2O_3 -containing samples.

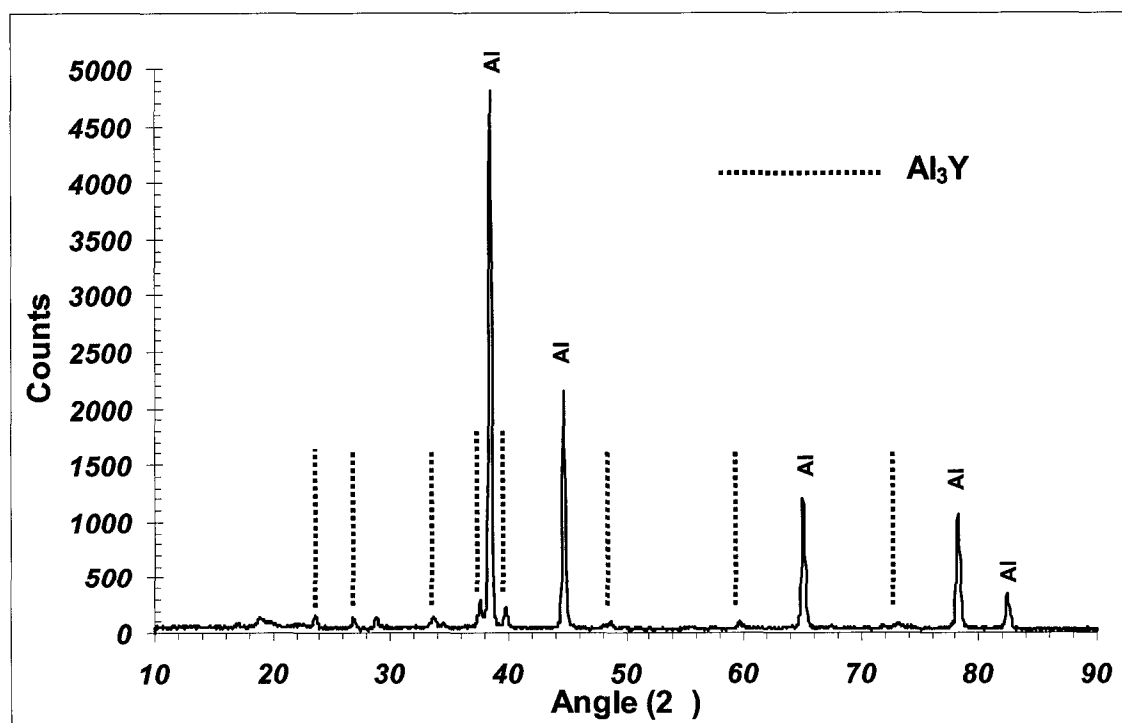
The appearance of the Al_3Y intermetallic compound could result from possible melting of Ytria particles when the samples were melted in the arc melting furnace, since the temperature could reach as high as $3700^\circ C$ which exceeds the melting point of Y_2O_3 which is $\sim 2400^\circ C$, or as a result of possible decomposition of Y_2O_3 or reaction between Ytria and aluminum that led to the formation of an equilibrium phase of Al_3Y intermetallic compound.



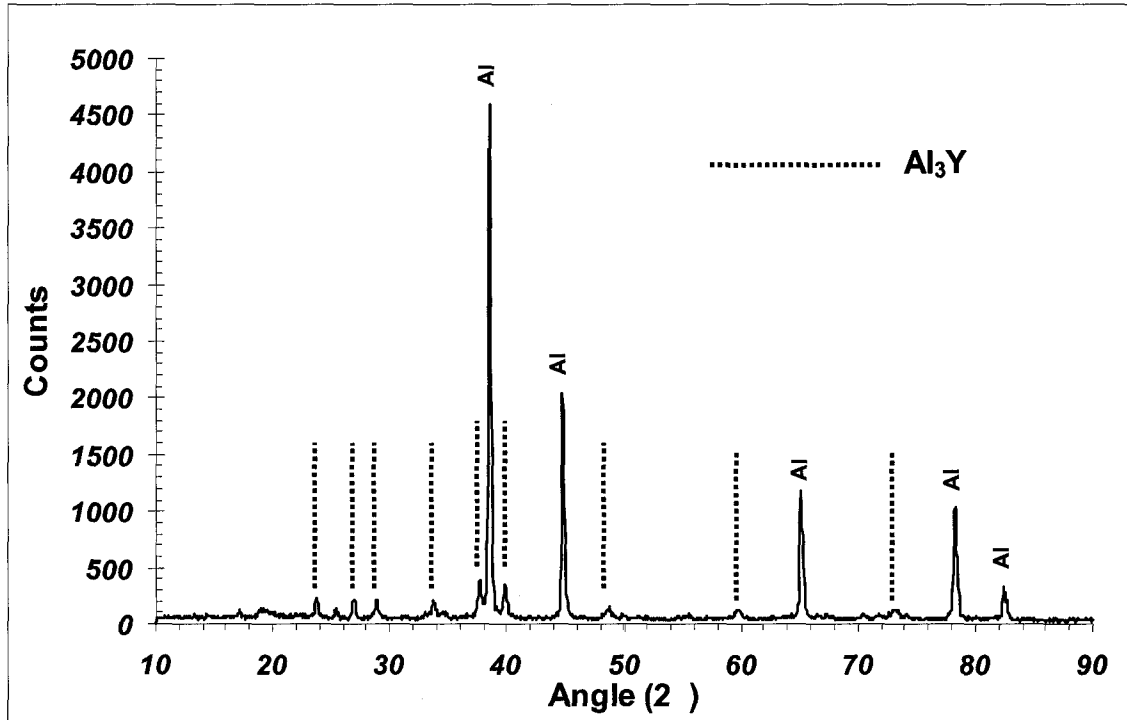
(a)



(b)



(c)



(d)

Figure 2.2-4. X-ray diffraction patterns of Y_2O_3 -free aluminum and Y_2O_3 -containing aluminum samples

When Y was released from Y_2O_3 , it may react with aluminum to form Al_3Y phase. Fig. 2.2-5 illustrates a Y-Al phase diagram. The solubility of Y in Al is very low, less than 0.1wt%; beyond this content, Al_3Y forms [126, 127].

The experimentally determined Al_3Y phase is consistent with the phase diagram of Al-Y system.

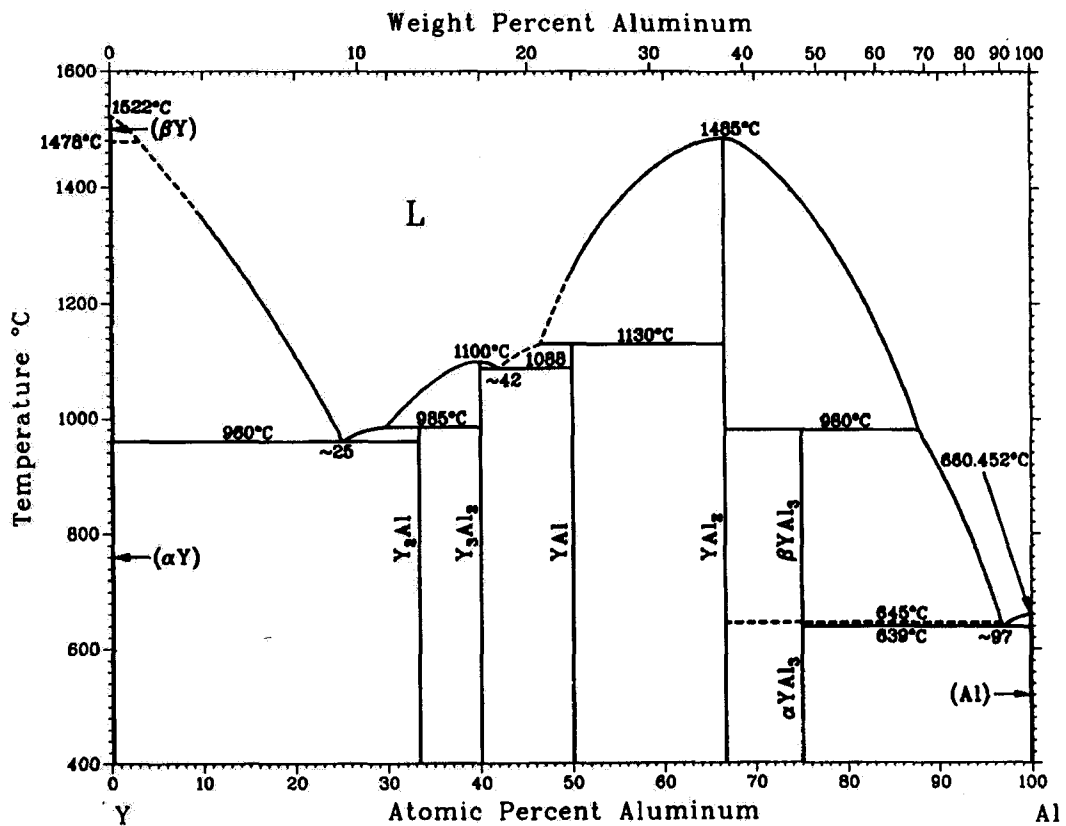


Figure 2.2-5. An Al-Y Phase Diagram [127].

In summary, eutectic microstructure developed during melting when Y_2O_3 particles were added to aluminum. However, the Y_2O_3 particles were somehow melted or decomposed; the released Y reacted with aluminum to form Al_3Y phase. The final eutectic microstructure consisted of aluminum dendritic domains and Al_3Y -aluminum mixture. The Al_3Y phase increased with the content of Y_2O_3 .

3 Mechanical properties of Aluminum Modified with Y_2O_3 Addition

The wear resistance of a material is mainly dependent on its mechanical properties, among which the hardness may play an important role.

Hardness is not a fundamental property of a material, but depends on many mechanical properties such as the tensile strength, young's modulus, and the yield strength. When selecting materials for wear application, one needs to first consider the hardness of the materials, the harder the surface is, usually the wear is less.

The dependence of the wear resistance is usually described using the well-known Archold's equation [128, 129]:

$$Wl = \frac{K \times L \times l}{H} \quad (2.2-1)$$

where Wl is the wear volume loss, K is the wear coefficient, L is the applied load, l is the sliding distance, and H is the hardness of the material.

Hardness can be defined as the resistance of a metal to plastic deformation, which usually can be determined by indentation test. This term may also refer to stiffness or the resistance to scratching, abrasion, or cutting. The greater the hardness of a metal, the greater is its resistance to deformation. Hardness is of importance to the performance of a material. Although hardness is undoubtedly a measurable quantity, to date it has not yet

been well described; or in other words, it appears not to be easy to establish a quantitative relationship between hardness and other basic mechanical properties, such as Young modulus, yield strength, ultimate tensile strength, etc. Therefore, a hardness test only results in a dimensionless number which reflects the hardness of a material. By fixing the testing condition, e.g., using standard indenters and load, materials can be compared in terms of hardness [130-132].

The wear resistance is also influenced by other mechanical properties such as elasticity [133], although hardness plays a predominant role. This chapter reports our studies on the effect of Y_2O_3 additions on hardness and elastic behavior of aluminum.

3.1 Hardness measurement

Hardness measurement can be performed on macro-, micro- or nano- levels, depending on the applied force and dimensions of the indenter.

Macro-indentation is a quick and simple method for determining hardness of a material. By measuring the geometry of a dent or the indentation depth under a fixed load, the hardness of the material can be determined. When evaluating coatings, one has to use light loads and smaller indenters, since the macro-indentation could be too large relative to the thickness of the coatings.

Furthermore, if one wants to evaluate hardness values of different phases in a heterogeneous material, macro-hardness measurement is obviously inadequate. In this case, micro-hardness measurements should be carried out.

Similar to macro-hardness test, the micro-hardness is determined also using an indenter such as a Vickers or Knoop indenter but with smaller tip and under considerably smaller load. The resultant dents are so small that they must be measured under a microscope. Hardness values of different phases and microconstituents can thus be determined.

Recent development of the microindentation technique has made it possible to record the load-displacement curve, from which not only the hardness but also other mechanical properties can be evaluated. These are two important parameters that can be determined from the load-displacement curve. One is the maximum penetration depth, h_{\max} , a measure of a material's hardness; the smaller the depth, the harder the material. The second parameter is the ratio (η) of the recoverable deformation energy (S_r - the area enclosed under the unloading curve and maximum penetration depth) to the total deformation energy (S_t -is the area enclosed under the loading curve and the maximum depth). Fig3.1-1 shows a typical load-displacement curve, in which the above-mentioned h_{\max} , S_t and S_r are marked.

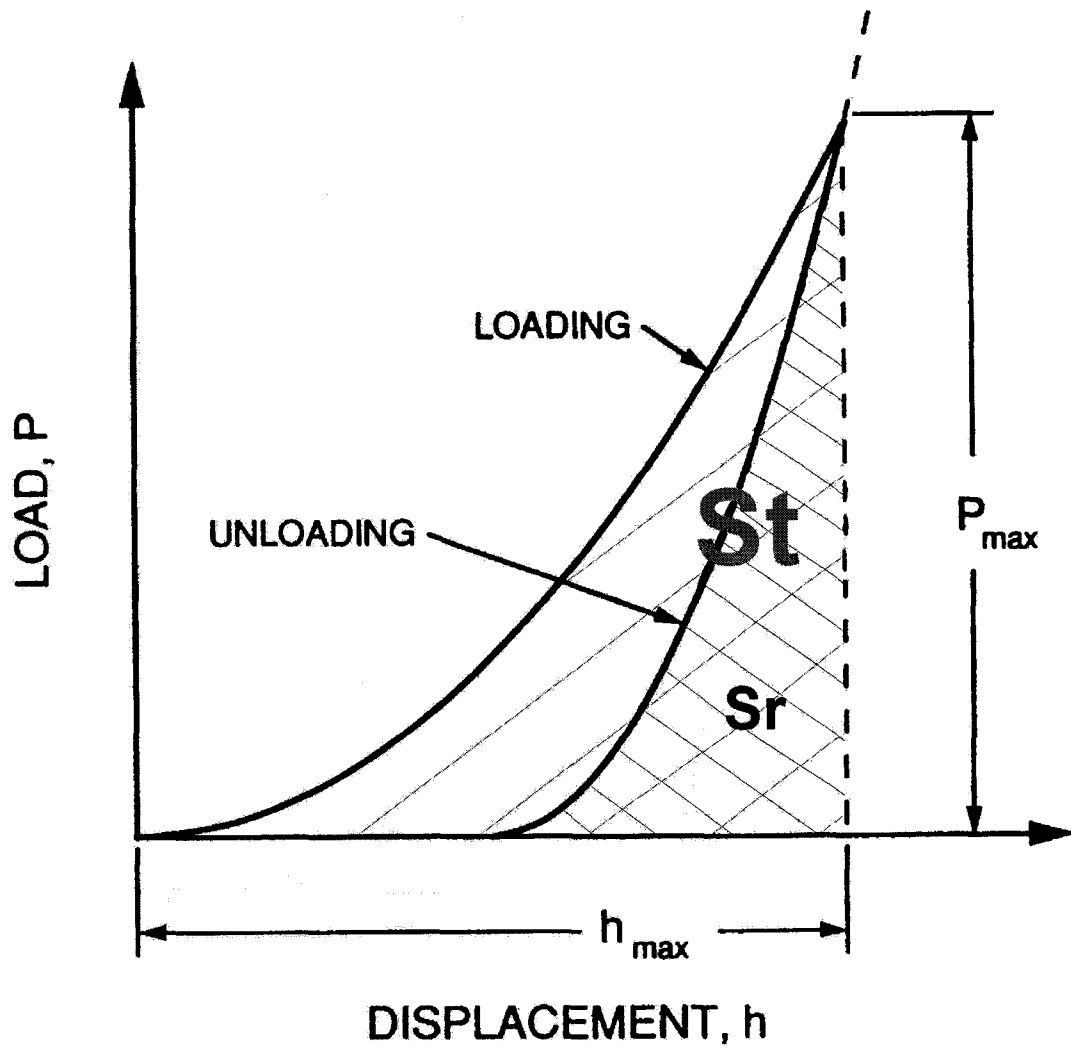


Figure 3.1-1 A schematic representation of load –displacement curve
 P_{max} : the maximum indentation load; h_{max} : the indenter displacement under P_{max} ; [134].

In the present work, macro-hardness and micro-hardness of Y_2O_3 -free and Y_2O_3 -containing Al samples were determined.

3.1.1 Macro-hardness measurement

Samples respectively containing 0wt%, 5wt%, 10wt%, and 20wt% Y_2O_3 were cut from a piece of each material made using an arc melting furnace, described in the previous chapter. The samples had dimensions of $10 \times 10 \times 5$ mm. All samples were polished using abrasive paper of grit 600 in order to obtain smooth surfaces for hardness measurements.

A Rockwell Hardness testing machine (Wilson) was used for macrohardness measurement using Rockwell B scale. The applied load was 100 Kg, and the indenter was made of a tool steel ball with a diameter of 1.5875 mm.

During the hardness test, ten different spots on the surface of each sample were randomly chosen. The final hardness was an average of 10 hardness measurements. The variation of the measured hardness for each group of samples was $\pm 5\%$. Table 3.1 shows the average Rockwell B hardness numbers of the materials, being tested as a function of Y_2O_3 content.

Table 3.1-1The variation of HRB number with Y_2O_3 content.

Materials	HRB
Al-0wt% Y_2O_3	25
Al-5wt% Y_2O_3	28
Al-10wt% Y_2O_3	36
Al-20wt% Y_2O_3	49

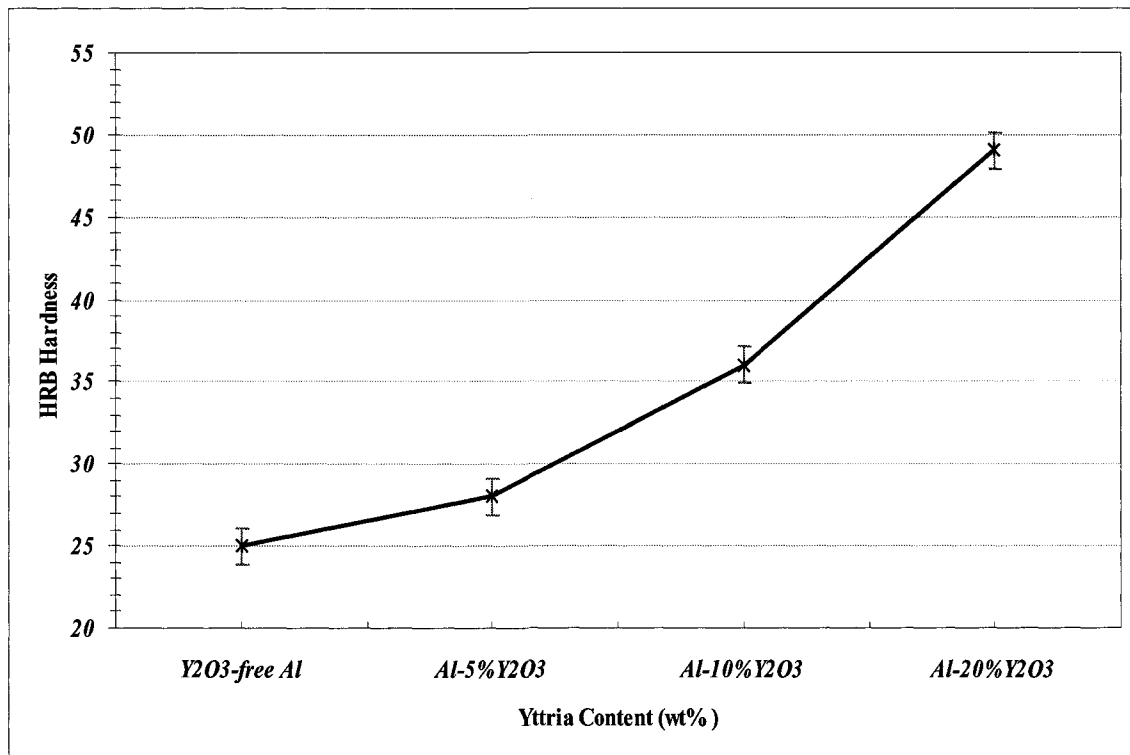


Figure 3.1-2 The change in HRB number as a function of the Y_2O_3 content.

From Table 3.1-1 and Fig. 3.1-2 it is clear that the hardness increased with the increase of the yttria content in the material. It has been demonstrated in chapter 2 that the microstructure of aluminum was refined by adding yttria and the Y_2O_3 decomposition led to the formation of a eutectic mixture consisting of Al and Al_3Y . The effect of second phase strengthening and microstructure refinement, the Y_2O_3 -containing Al samples were harder.

In order to obtain more information on the increase in hardness, especially the localized mechanical behavior, micro-hardness measurements were carried out on different

domains. Results of the measurement are presented in the next section with the aim of understanding the effect of Y_2O_3 additions on the hardness of aluminum.

3.1.1 Micro-hardness measurement

Samples of 0wt%, 5wt%, 10wt%, and 20wt% Y_2O_3 were prepared for micro-hardness indentation. All samples were mounted with epoxy resin, ground using sand papers and then polished to roughness of $0.05\ \mu\text{m}$ using a $0.05\ \mu\text{m}$ alumina slurry. In order to identify different phases and to evaluate their mechanical properties by microindentation, all samples were etched using *Keller's reagent*.

Microindentation measurements were carried out using a Fischer micromechanical probe (provided by Fischer Technology Inc) illustrated in fig. 3.1-3.

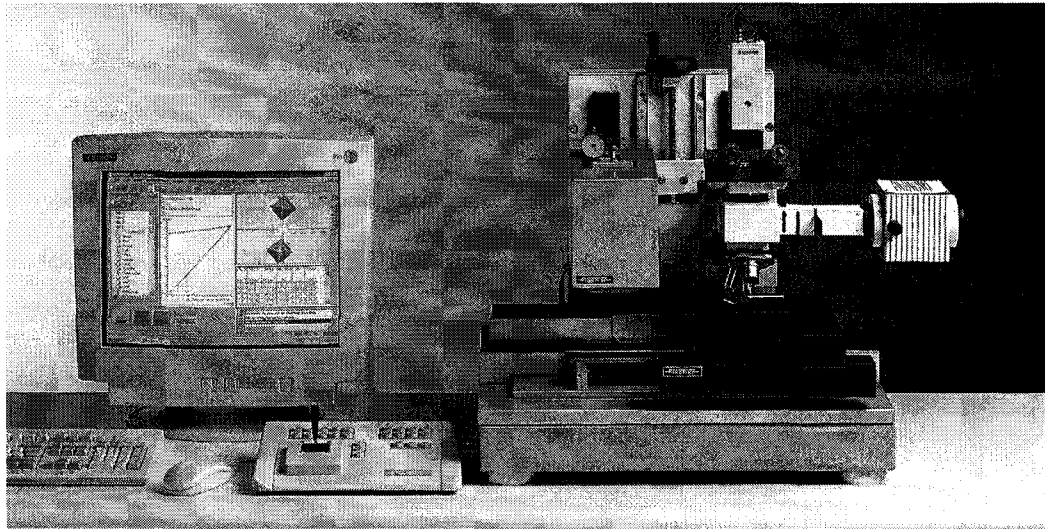


Figure 3.1-3 The Fischer micromechanical probe.

The micromechanical probe was associated with an optical microscope that has the capability of capturing digital images of an indented surface and conducting image analysis. The indenter had a pyramid-shaped diamond tip. The maximum indentation load was 300mN. The system was computer controlled and the load-displacement curve was recorded automatically. The measured micro-hardness was an average of 10 measurements. The variation in the measured hardness number for each group of samples was $\pm 5\%$.

Table 3.1-2 lists HV numbers of different domains in various samples obtained from the microindentation test. Fig. 3.1-4 shows optical micrographs of different surfaces on which microindentation was performed.

From Table 3.1-2, hardness of the matrix (primary aluminum-yttrium solid solution phase) increased when Y_2O_3 was added. The more added Y_2O_3 , the harder the matrix.

In the sample added with 20 wt% Y_2O_3 , Al_3Y phase was so large that its hardness could be determined. Indentation test showed that the Al_3Y phase had hardness as high as 428.3 HV (Vickers's Hardness). In this sample, the eutectic structure became coarser (see Fig. 3.1-4d) and there were no distinctive eutectic domain and matrix for indentation test. Or in other words, the Al-20 wt% Y_2O_3 sample consisted of only large Al_3Y phase and coarser eutectic matrix as Fig. 3.1-4d illustrates.

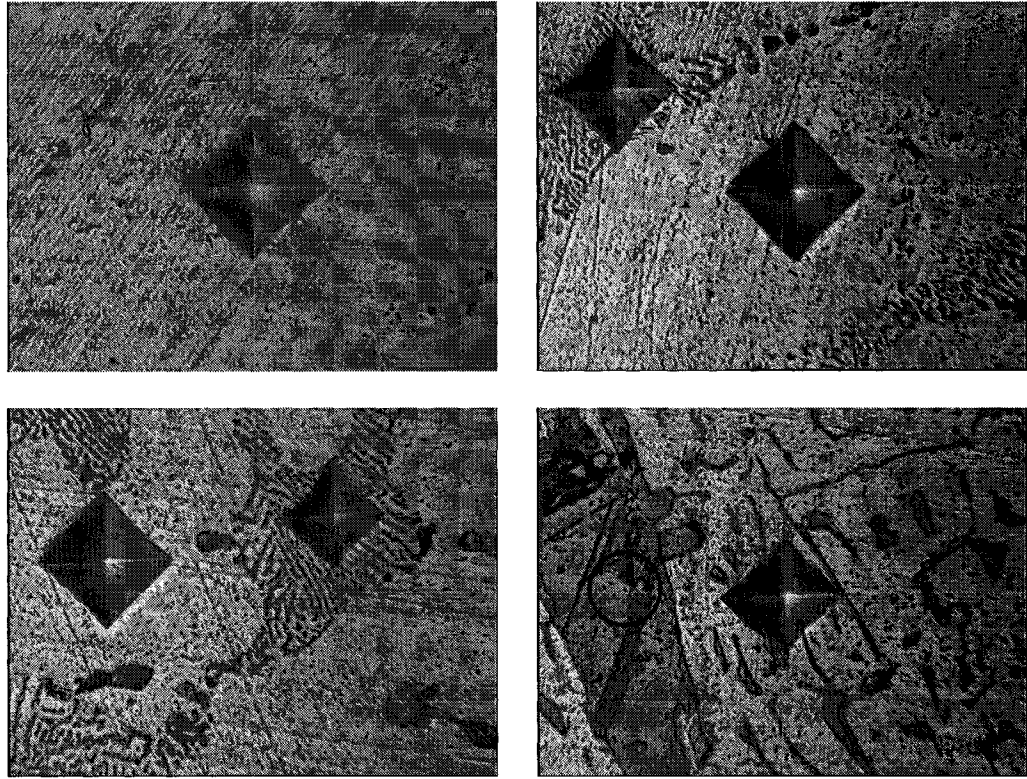


Figure 3.1-4 Indentation tests of surfaces of various samples:
 a) Al-0%Y₂O₃, b) Al-5%Y₂O₃, c) Al-10%Y₂O₃, d) Al-20%Y₂O₃.

Table 3.1-2 Microindentation measurements.

Material	<i>Matrix</i>	<i>Eutectic</i>	<i>Particles, (Al₃Y)</i>
	Vickers's Hardness (HV)	Vickers's Hardness (HV)	Vickers's Hardness (HV)
Al-0wt%Y ₂ O ₃	25	N/A	N/A
Al-5wt%Y ₂ O ₃	26	43.8	N/A
Al-10wt%Y ₂ O ₃	30.7	46.4	N/A
Al-20wt%Y ₂ O ₃	48.8	48.8	428.3

The strengthening of aluminum samples by Y_2O_3 additions was attributed to the eutectic mixture consisting of Al and Al_3Y phase and to the effect of solid solution strengthening of aluminum by yttrium when Y_2O_3 decomposed during the melting process. Fig. 3.1-5 shows the increase of the matrix hardness with the Y_2O_3 content.

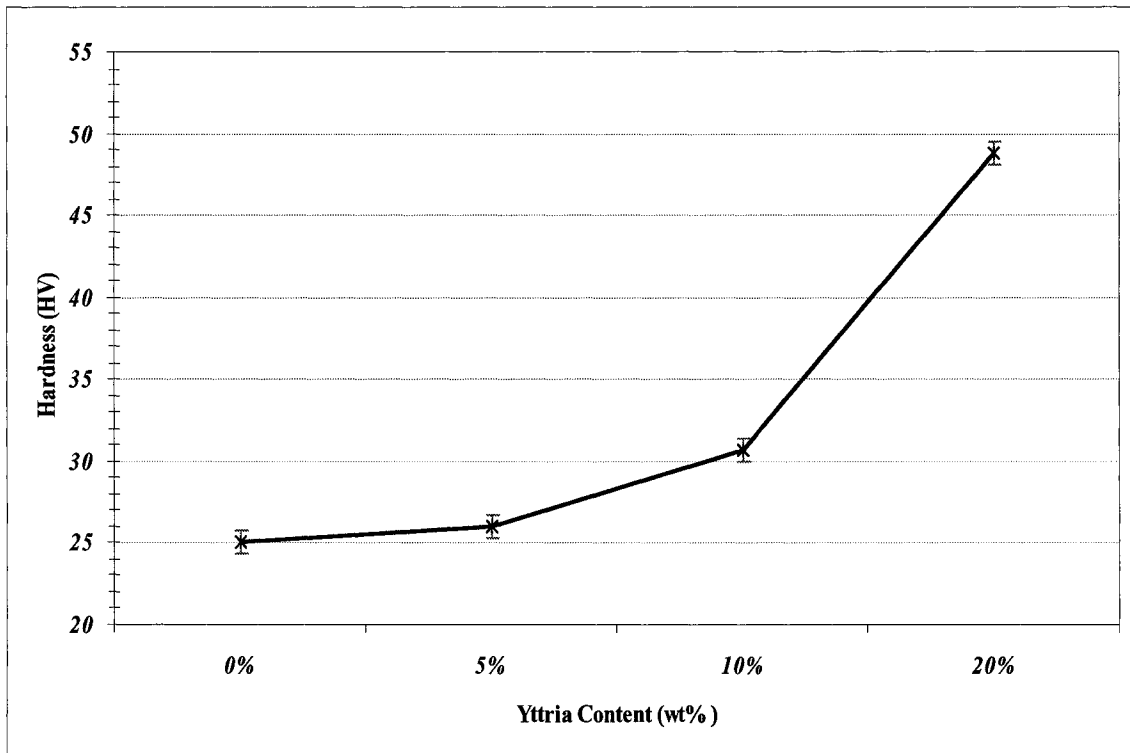


Figure 3.1-5 Increase in the hardness of the matrix by yttrium.

In additions to hardness, the elastic behavior of the samples was also improved by Y_2O_3 additions. The elastic behavior may be reflected by the η value, the ratio of the recoverable deformation energy to the total deformation energy.

The value of η can be determined from the load-displacement curve. Load-displacement curves of Y_2O_3 -free and Y_2O_3 -containing Al samples were determined. Fig.

3.1-6 illustrates load-displacement curves of matrixes of Y_2O_3 -free and Y_2O_3 -containing Al samples.

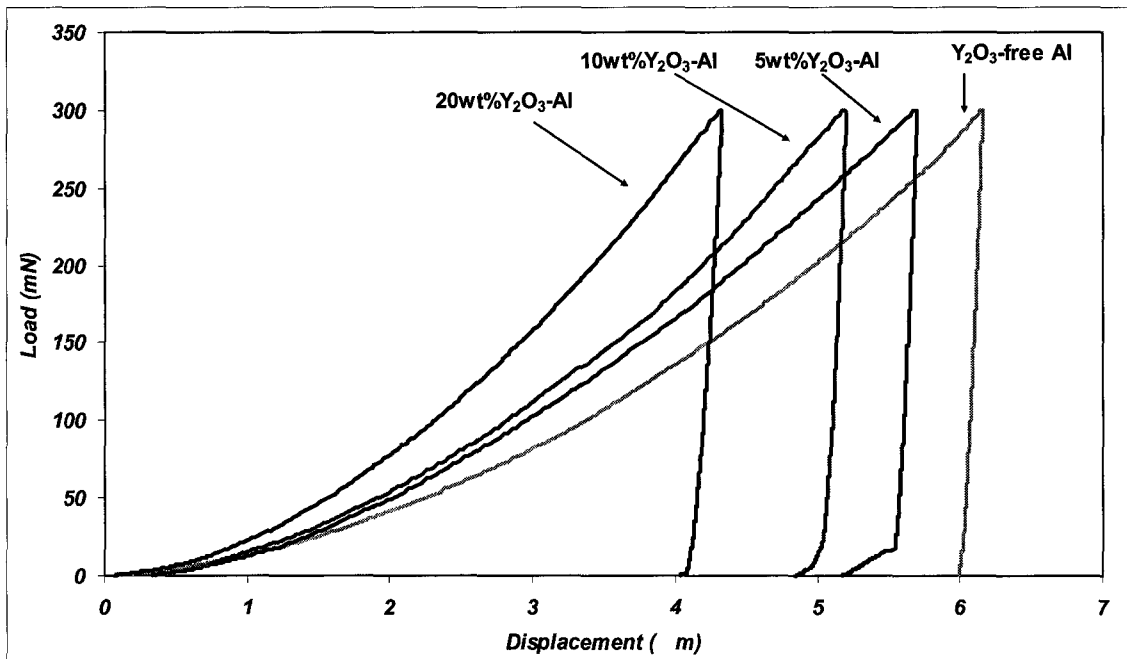


Figure 3.1-6 Load-displacement curves of Y_2O_3 -free and Y_2O_3 -containing Aluminum samples.

η value of the materials were obtained from the load-displacement curves and are given in Table 3.1-3.

Table 3.1-3 The measured (η) ratio of the matrixes in Y_2O_3 -free and Y_2O_3 -containing Aluminum samples.

Materials (Matrix)	η (%)
Al-0wt% Y_2O_3	2.927
Al-5wt% Y_2O_3	3.510
Al-10wt% Y_2O_3	4.333
Al-20wt% Y_2O_3	7.606

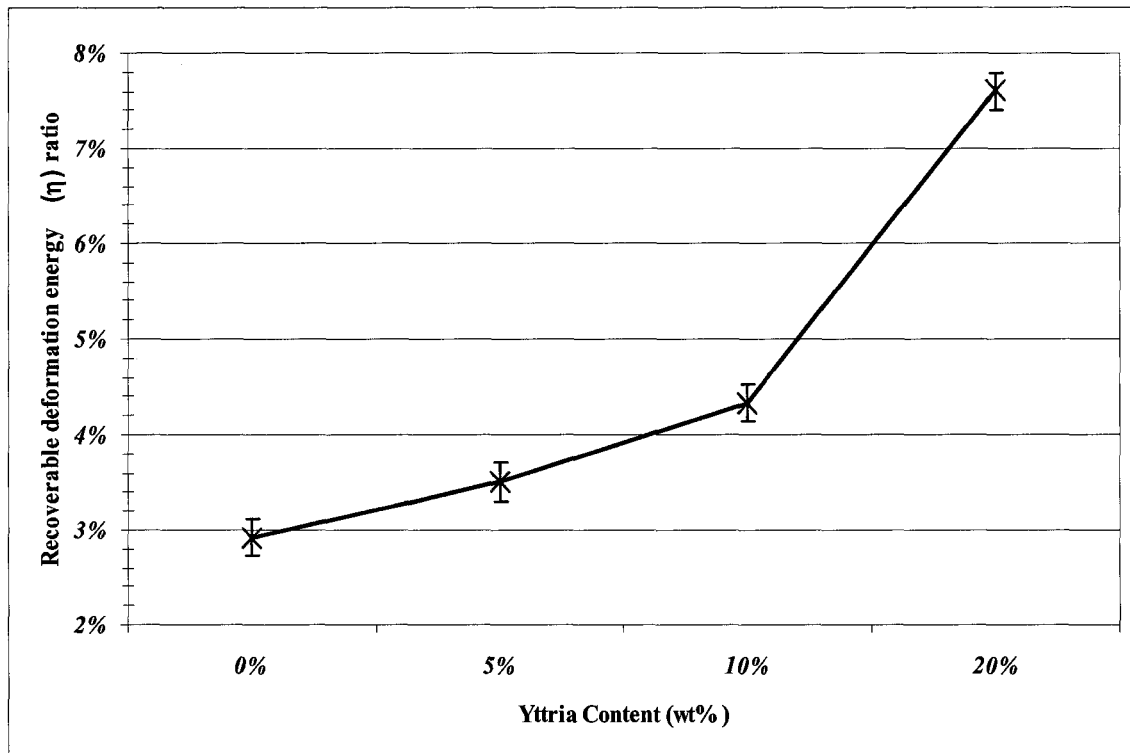


Figure 3.1-7 Variation of (η) ratio in Y_2O_3 -free and Y_2O_3 -containing Aluminum samples.

Fig. 3.1-7 illustrates that the increase in η value with an increase in the Y_2O_3 content in the samples.

The increase in η value could result from the solution-strengthening of the matrix by Yttrium. The corresponding increase in the yield strength or elastic limit could lead to higher η value. The hard Al_3Y phase may also have a similar effect on η value. An increase in the elastic behavior may contribute to the wear resistance of the materials. Such an effect has been studied [133].

The effect of solution-strengthening may not be strong, since the solubility of Yttrium in aluminum is low, as shown in Fig 3.1-8 which is a portion of aluminum-Yttrium phase diagram that is illustrated in Fig.3.1-9. Therefore, the precipitation of Al_3Y

could play a predominate role in strengthening the material. The $\alpha\text{-Al}_3\text{Y}$ phase exists in the eutectic mixture which may help to block dislocation motion and thus suppress the plastic flow. Larger $\alpha\text{-Al}_3\text{Y}$ precipitates in samples containing more Y_2O_3 such as 20wt% Y_2O_3 -containing aluminum sample also provide more barriers to dislocation movement, thus hardening the material.

As a result of the increase in hardness, higher wear resistance could be obtained.

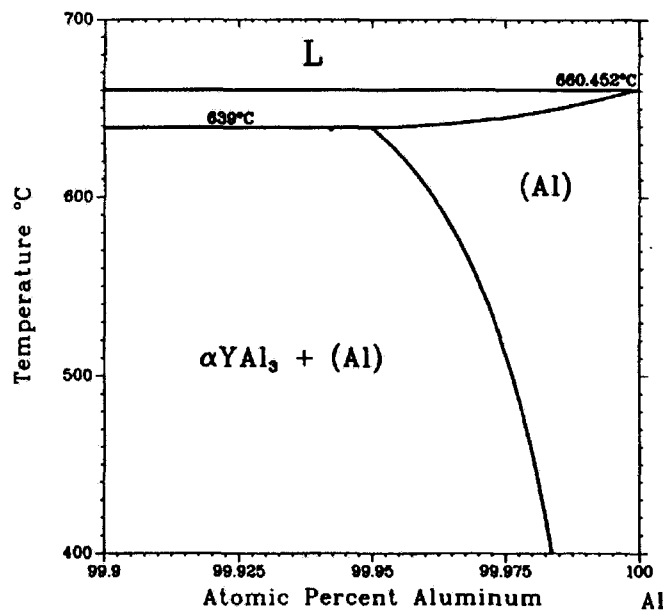


Figure 3.1-8 The solubility of Yin Al shown in an Al-Y phase diagram [127].

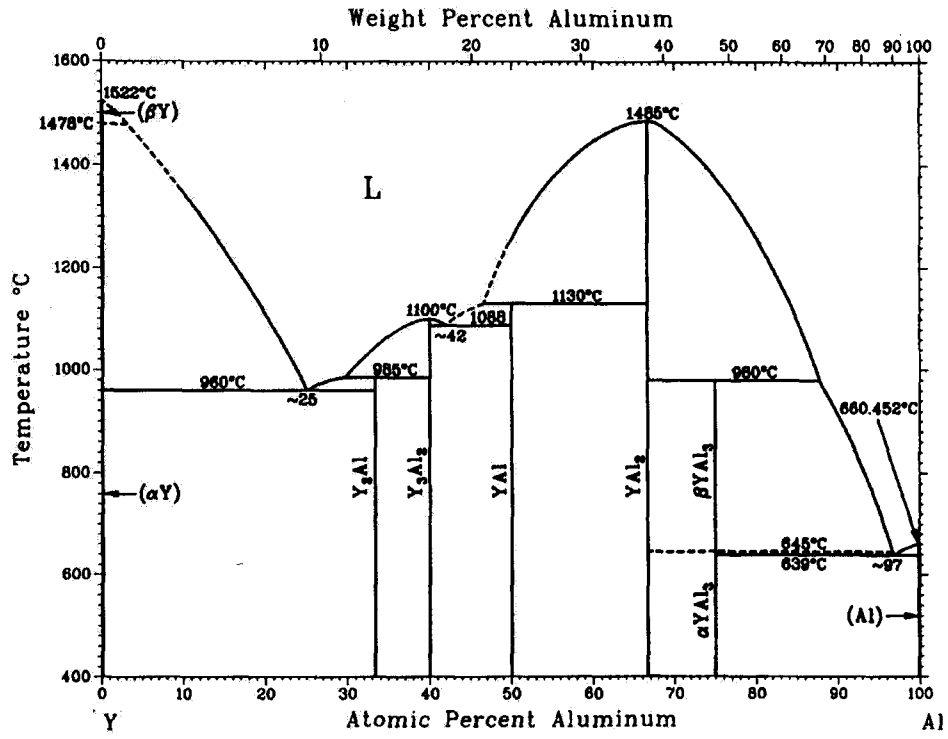


Figure 3.1-9 An Aluminum-Yttrium phase diagram [127]

4 Electrochemical Behavior of Aluminum Modified with Y₂O₃ Addition

4.1 Introduction

Severe damage by corrosive wear is largely attributed to the synergism of corrosion and wear. It is therefore of importance to evaluate effects of Y₂O₃ additions on corrosion behavior of aluminum. The electrochemical polarization test is perhaps the one that provides the most comprehensive information on the corrosion behavior of a material. Corrosion potential, corrosion current and passivity can be evaluated by performing the polarization test. For Al-based materials, the passivity is a particularly important parameter that needs to be evaluated. Passivity refers to the resistance to electrochemical reaction or to corrosion. Such resistance results from the formation of a protective film on a metal surface. This film is usually very thin, in the range of a few nanometers, invisible, consisting of oxygen compounds of the metal. When the passive state is established, the resistance of the metal to a corrosive medium largely depends on properties of the protective passive film. The formed films must be adherent to the metal's surface, dense, strong, thin, and fast to repair itself when damaged.

The passivation behavior of a metal is typically evaluated by measuring changes in current with potential using a basic electrochemical setup. When the potential is increased to a more anodic (positive) range, if the current decreases as Fig. 4.1-1 illustrates, the metal has passivation capability and can be protected by a passive film.

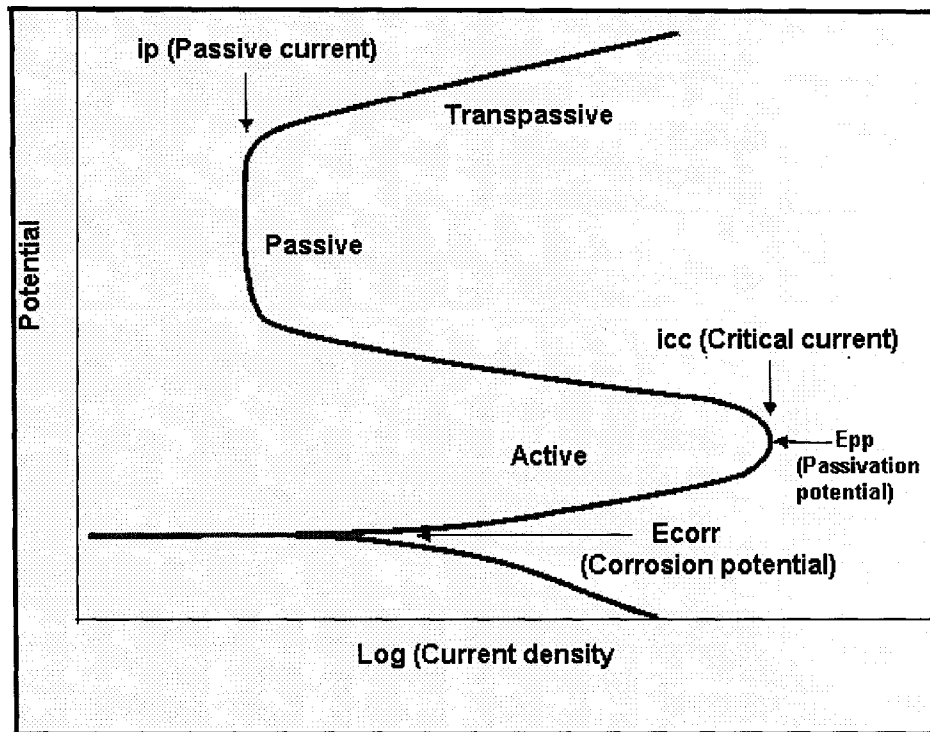


Figure 4.1-1 Typical polarization Curve of a passive metal

Only a few metallic systems, such as aluminum, chromium, titanium and nickel, have passivation capabilities, which render them resistant to corrosion.

In addition to passivation, other parameters, such as corrosion potential (E_{corr}) and pitting potential (E_{pp}), also reflect the corrosion resistance. The higher the potentials, the more the metals are resistant to corrosion.

In the passive region, the corrosion rate is proportional to the passive current density (i_p), therefore, the lower the current density, the lower the corrosion rate. According to Faraday's law, corrosion rate can be calculated from the corrosion current [135];

$$\text{Corrosion rate} = \frac{i_{corr}}{nF} \quad (4.1-1)$$

where i_{corr} is the corrosion current density (A/m^2), F is Faraday's constant ($96490C/mol.e^-$), and n is number of electrons per mole of metal corroded.

The phenomenon of passivation is especially important to the corrosion behavior of aluminum (Al), stainless steels, titanium (Ti), and chromium (Cr) which are basic metals for a wide variety of industrial applications.

Aluminum possesses excellent corrosion resistance due to its high passivation capability and a strong passive film bonded strongly to the substrate. Aluminum has also a strong capability of repassivation. All these render the metal highly resistant to corrosion [21, 26, 136-140].

The passive film on aluminum can form rapidly and thus prevent further corrosive attack. In dry air, the natural passive film also forms rapidly to a limited thickness (3~10 nm) [21, 25].

Corrosion of aluminum is relatively localized, resulting in random formation of pits. When applied potential exceeds a critical value (i.e., the pitting potential) pitting takes place.

In this chapter, polarization behavior, repassivation (electrochemical scratch test), mechanical properties of the formed passive film (Nano-indentation and micro scratch tests) for Y_2O_3 -free Al, and Y_2O_3 -containing Al samples were evaluated in order to investigate the effect of adding Y_2O_3 to aluminum on its corrosion behavior as well as its effect on properties of the passive film.

4.2 Electrochemical polarization test

Electrochemical polarization behavior of Y_2O_3 -free and Y_2O_3 -containing samples was determined in 0.1M H_2SO_4 and 3.5wt% $NaCl$ solutions respectively. Samples containing 0wt% Y_2O_3 , 5wt% Y_2O_3 , 10wt% Y_2O_3 , and 20wt% Y_2O_3 were cut from cast blocks that received homogenization treatment at 630°C for 1 hour. The size of the samples was 10×10×5 mm and were mounted in epoxy. The samples were polished to a roughness of 0.05μm. After polishing, some cavities were observed at the sample/epoxy interface. In order to avoid any possible interference of the interface in the polarization test, a layer of epoxy/hardener was applied at the sample/epoxy interface and then left to dry for several hours before the polarization test.

A Gamry PC4/750 electrochemical measuring system was employed for electrochemical polarization tests at a scan rate of 0.3mV/s. A saturated calomel electrode (SCE) was used as a reference electrode, and a platinum wire as an auxiliary electrode. All polarization tests were repeated four times. The polarization tests were fairly repeatable.

Polarization curves of samples containing various Y_2O_3 additions in a 0.1M H_2SO_4 solution were measured and illustrated in Fig. 4.2-1.

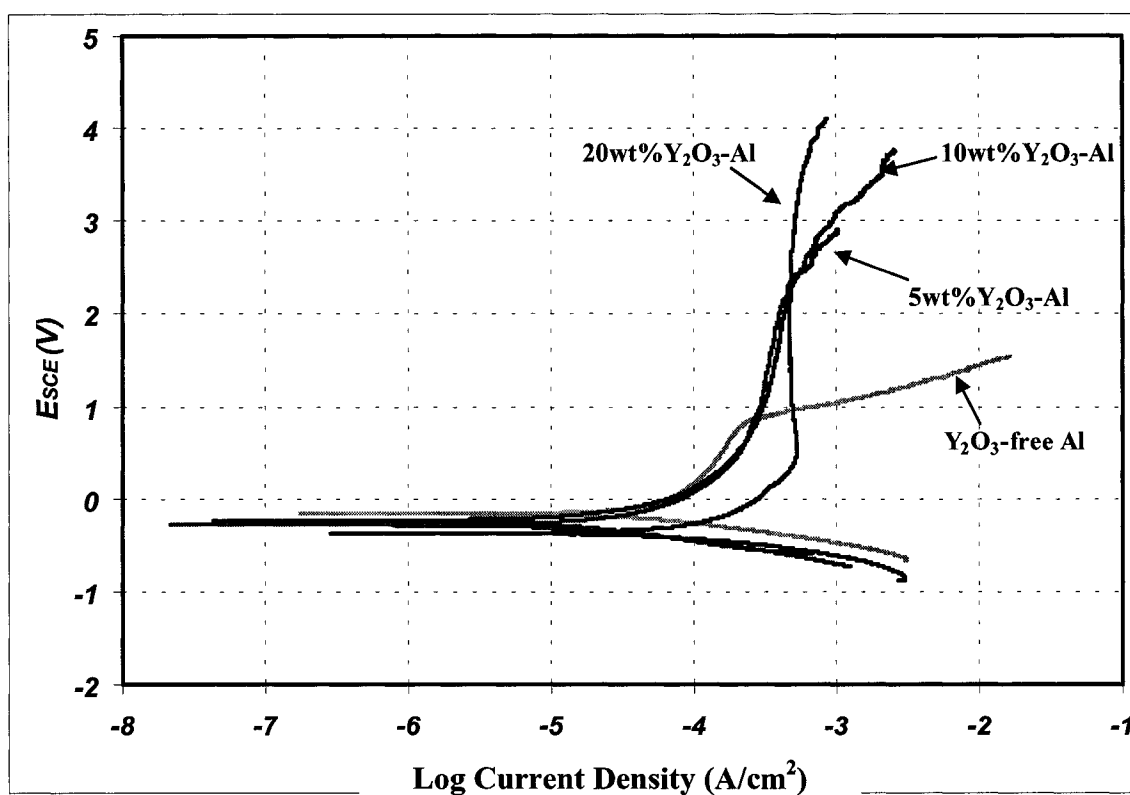


Figure 4.2-1 Polarization curves of Y_2O_3 -free and Y_2O_3 -containing samples in a 0.1M H_2SO_4 solution.

As noted, although adding Y_2O_3 did not significantly influence the corrosion current and potential, the passive behavior of the samples was improved when Y_2O_3 was added and their passive range extended to higher potentials. Such extension shifted the pitting potentials to higher values and thus enhanced the corrosion resistance of the metal. The polarization curve of 20 wt% Y_2O_3 - containing sample shows that the corrosion current and corrosion potential were affected a little more than other samples; its corrosion current shifted toward higher current density with a very slight decrease in the corrosion potential. However, the pitting potential of this sample shifted to markedly higher value, leading to a considerably extended passivation potential range. This can enhance the resistance of the metal to corrosion.

The polarization behavior of the samples in a 3.5wt% NaCl solution was evaluated. Fig. 4.2-2 shows the obtained polarization curves of samples containing different amounts of Y_2O_3 in a 3.5 wt% NaCl solution.

One may see that the corrosion current and potential were affected by adding yttria to aluminum. The added yttria decreased the corrosion current (i_{corr}) and increased the corrosion potential (E_{corr}), while the pitting potential (E_{pp}) was not affected. Although the pitting potential was not affected by adding yttria to the Al in the NaCl solution, the increase in the corrosion potential was beneficial to the corrosion resistance of the material. In addition, Y_2O_3 -containing samples show better passive behavior than the Y_2O_3 -free sample by reducing the corrosion current, which also enhances the corrosion resistance.

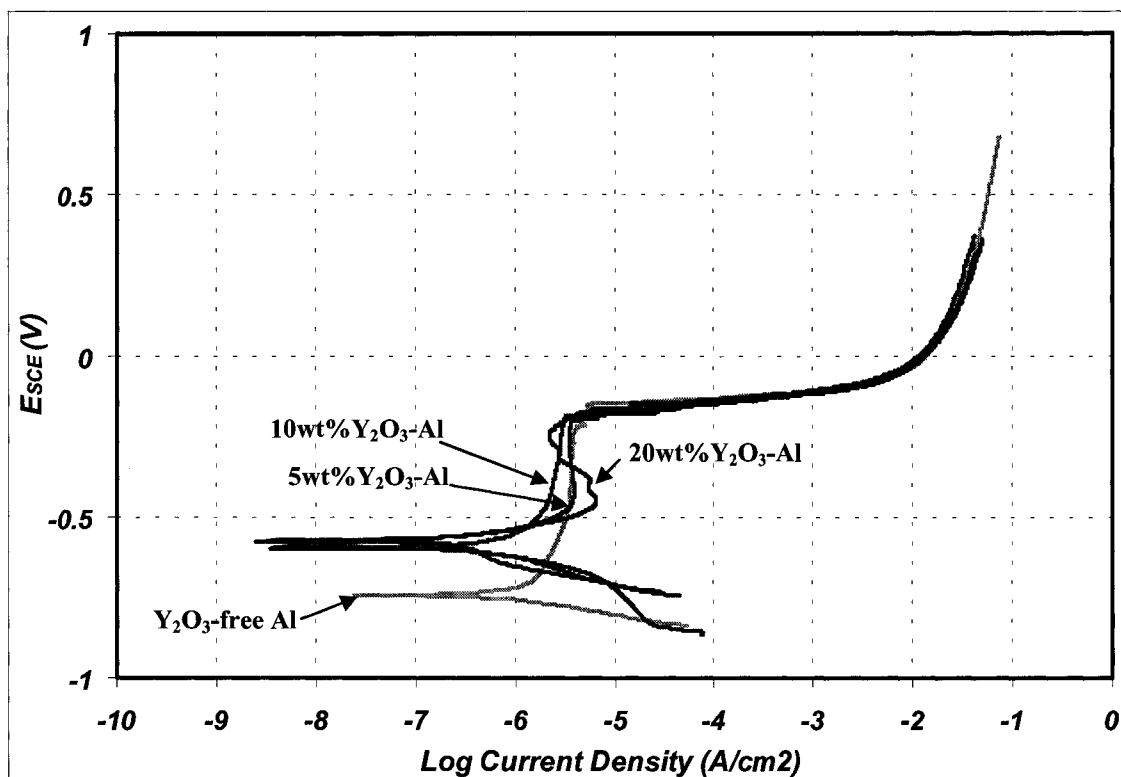


Figure 4.2-2 Polarization curves of Y_2O_3 -free and Y_2O_3 -containing samples in a 3.5wt% NaCl solution.

The improvement in polarization behavior of the samples could be attributed to the formation of a stronger and more adherent passive film due to the high oxygen affinity of yttrium. Efforts have been made to explain the effect of rare-earth elements in improving the corrosion resistance of Al alloys [141] and pure aluminum [28]. It was also found that small additions of yttrium improved the polarization behavior of 304 stainless steel [119, 121] as well as the mechanical properties and the adherence of its passive film [119, 123]. In the present samples, Y_2O_3 decomposed during the melting process and yttrium existed mainly in the form of Al_3Y compound. Such a compound could play a similar role in improving the passive film, especially its adherence to the

substrate. Previous studies have also demonstrated that the passive film was enhanced by adding Y_2O_3 particles to aluminum in a cast process [28].

4.3 Electrochemical scratch test

As mentioned earlier, the passivation capability of aluminum results in its resistance to corrosion. However, in many cases, a surface is also under mechanical attack in addition to corrosion. For instance, erosion corrosion of pipes in chemical processing and the oilsand industries. The formed passive film could be damaged by a slurry flow containing an abrasive material. Under such circumstances, re-passivation ability becomes important. Therefore, repassivation is another parameter that needs to be investigated.

In this study, the repassivation behavior of Y_2O_3 -free and Y_2O_3 -containing samples was investigated using an electrochemical scratch test.

Electrochemical scratch test was performed by scratching a surface immersed in corrosive solution under an applied potential. Fig. 4.3-1 illustrates a typical current-time curve recorded during electrochemical scratch testing. When the passive film is damaged, current will increase, and then decrease after scratching stops. The slope of the current-time curve may provide information on the resistance of the film to scratching and the re-passivation rate. The area, S , under the curve is related to the total amount of dissolved material caused by scratching in the corrosive medium, which can be determined using the equation:

$$S = \int_{t_i}^{t_f} i(t) dt \quad (4.3-1)$$

where S is the area under the current-time curve, i is the current, t is the time, t_f and t_i are the initial time when the change in current starts and the final time when the change in current stops respectively.

The electrochemical scratch has been widely used to study dynamics of repassivation process [142, 143]

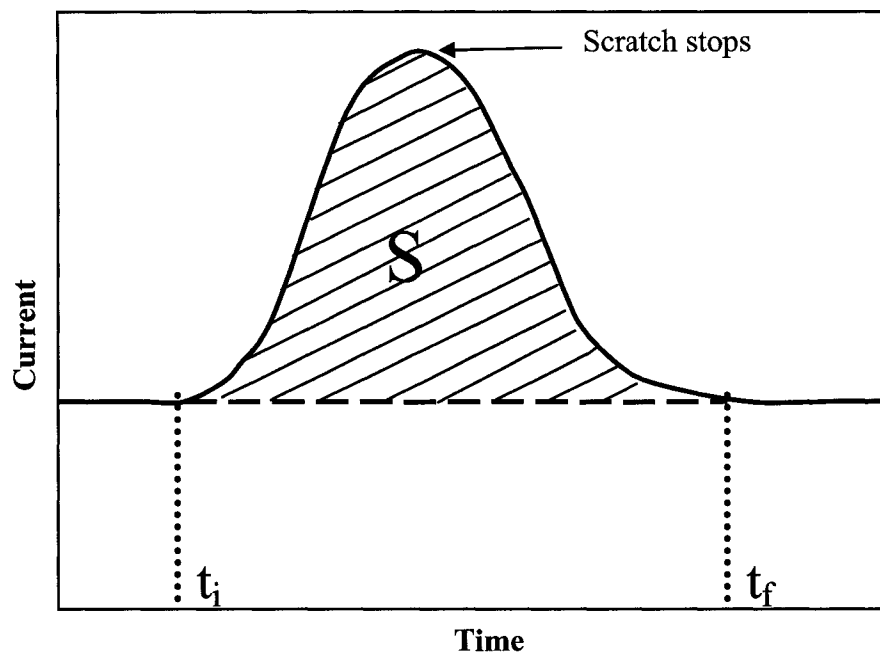


Figure 4.3-1 Schematic plot of anodic current versus time.

The electrochemical scratch test can be useful not only to investigate passive film but also to investigate wear of a material in a corrosive solution [123].

In this section, electrochemical scratch tests were performed to determine Current-Time curves of Y_2O_3 -free and Y_2O_3 -containing samples in a 0.1M H_2SO_4 solution. Before the test, the samples were prepared by connecting them with conductive copper wires, mounting them in epoxy/hardener, and polishing them to roughness of 0.05μ . A Gamry PC4/750 electrochemical measurement system, in combination with a microtribometer (UMT), was employed for the electrochemical scratch test at a scan rate of 0.33mV/s and the current change was recorded every 0.025 seconds. A saturated calomel electrode (SCE) was used as a reference electrode, and a platinum wire as an auxiliary electrode. Scratching was made using universal micro-tribometer (UMT) under a constant load. The scratch length was 1 mm and the scratching speed was 1mm/second. The scratching tip was made of diamond. Two applied loads, 25mN and 35mN, were used in this experiment. The applied potential was 0.5V. All tests were repeated eight times for each sample at different spots. All results were consistent. The electrochemical scratch test was performed on samples with different Y_2O_3 in a 0.1M H_2SO_4 solution. Fig.4.3-2, A schematic illustration the electrochemical scratch system.

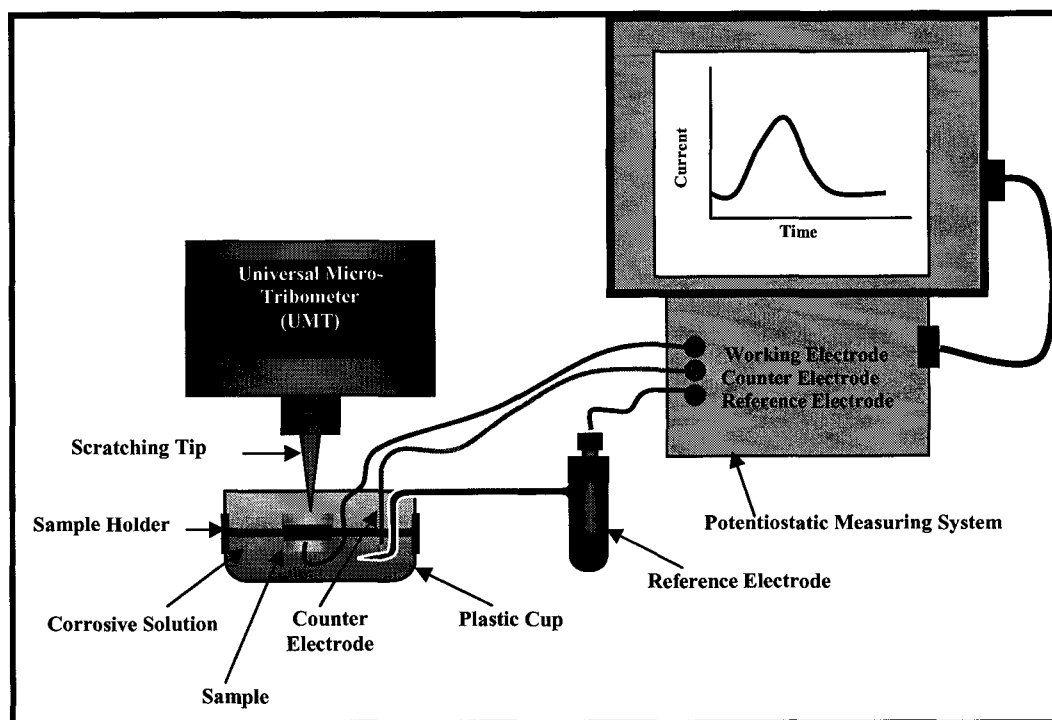


Figure 4.3-2 Schematic illustration of the electrochemical scratch set-up

Fig. 4.3-3 and Fig. 4.3-4 illustrate obtained current-time curves of Y_2O_3 -free and Y_2O_3 -containing samples in the 0.1M H_2SO_4 solution under applied load of 25mN and 35mN respectively. As shown in Fig. 4.3-3, for the test under an applied load of 25mN, the samples modified with Y_2O_3 showed less damage than Y_2O_3 -free samples, evidenced by their smaller area under the current-time curve,

$$S = \int_{t_i}^{t_f} i(t) dt$$

The 10wt% Y_2O_3 -Al sample showed the smallest S. When the scratching load was increased to 35mN, the improvement by Y_2O_3 additions was profound as Fig. 4.3-4 illustrates. Again, 10wt% Y_2O_3 -Al sample showed a better repassivation behavior than the others. The 10wt% Y_2O_3 -Al sample performed the best.

The beneficial effect of Y_2O_3 decreased when too much Y_2O_3 was added such as 20wt%. It is not very clear why 20wt% Y_2O_3 -containing sample performed poorly compared to that contains 10wt% Y_2O_3 -containing sample. It might be attributed to increased structural inhomogeneity. Although Al_3Y phase and possible residual Yttrium in the sample may enhance the passive film and its adherence to the substrate, the increased structural inhomogeneity could promote corrosion reaction when the passive film was damaged during electrochemical scratch. Different from pure corrosion, mechanical properties of both the substrate and the passive film also play a role in resisting the electrochemical scratch. Therefore, there should be an optimal amount of added Y_2O_3 correspond to an optimal balance between electrochemical and mechanical properties.

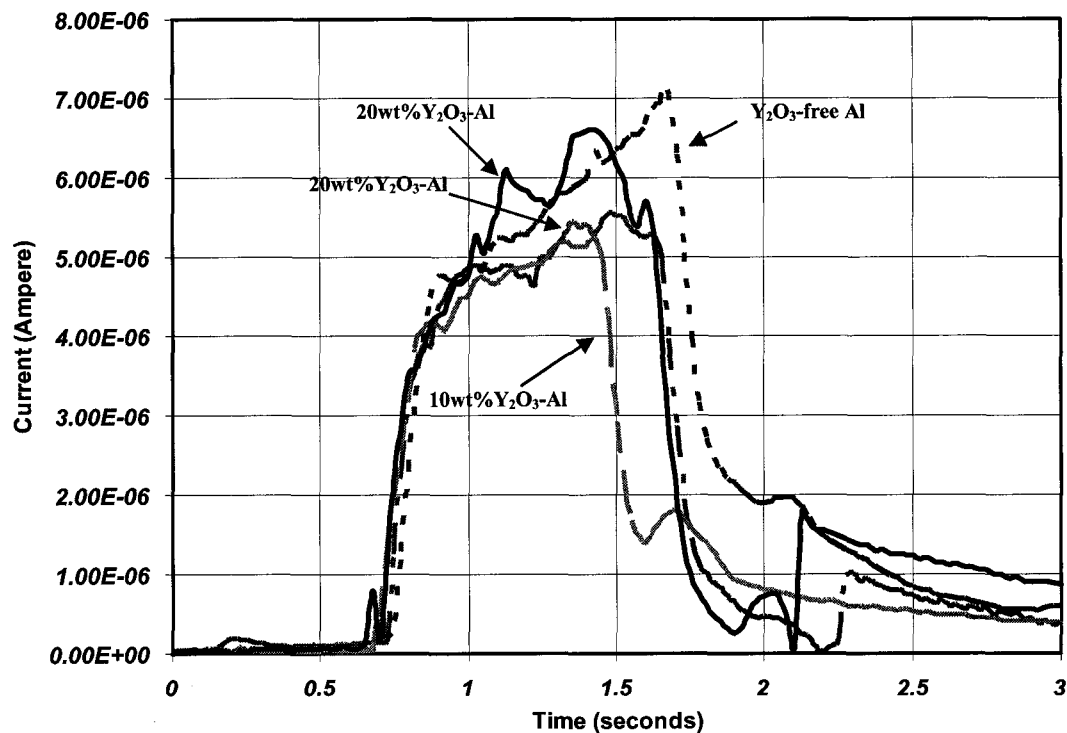


Figure 4.3-3 Current-Time Curves in a 0.1M H_2SO_4 solution, 25mN and 0.5 Volts.

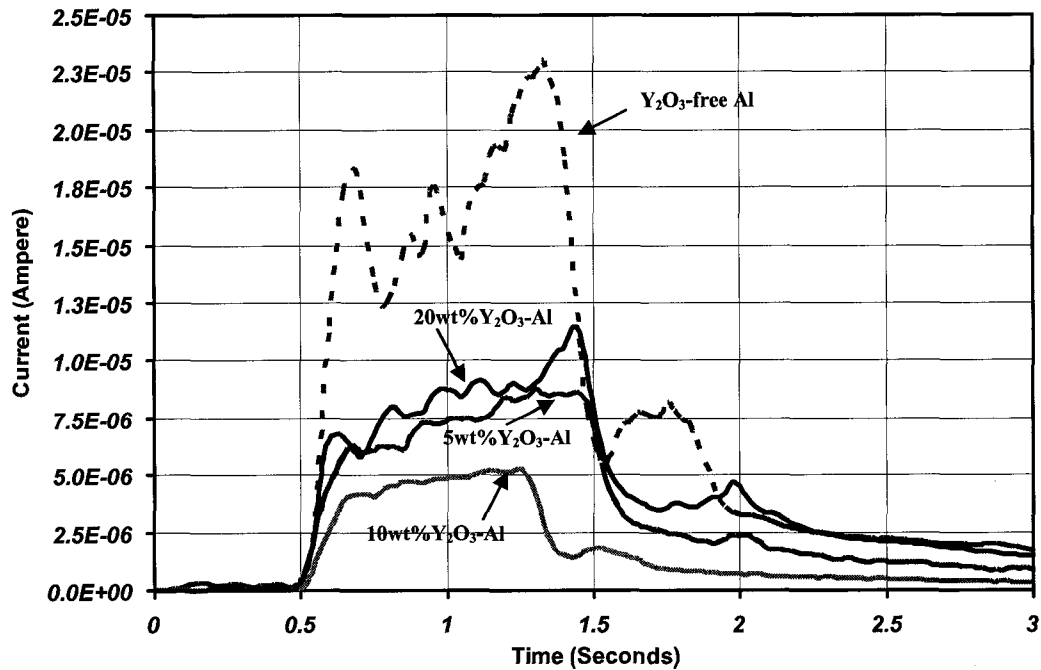


Figure 4.3-4 Current-Time Curves in a 0.1M H₂SO₄ solution, 35mN and 0.5 Volts.

4.4 Nanoindentation analysis: mechanical behavior of the passive film

The mechanical behavior of a passive film may be evaluated using a nanoindentation technique. During the test, an indenter tip is pressed into a surface under an applied load. Changes in the penetration depth with load are recorded.

The indentation depth reflects hardness of the surface. Young's modulus can be calculated based on the load displacement curve. Nanoindenting is an effective method for characterization of material mechanical properties on nano/micro-scales. Since the

indentation can be performed under light loads, this technique is ideal for evaluating the behavior of passive films.

In this study, mechanical properties of the passive film were evaluated using a Triboscope which is a combination of a nanoindenter and an atomic force microscope. The indenter tip was a four-sided pyramidal shaped diamond. The force resolution of the instrument was 0.1 μN and the displacement resolution was 0.2 nm. Hardness of a passive film was evaluated based on the load versus displacement curves obtained during nanoindentation tests. 15 and 20 μN loads were used in this experiment to evaluate mechanical properties of passive films on different samples. All tests were repeated ten times at different locations on the sample surfaces. The results were fairly consistent.

Before nanoindentation test, samples of Y_2O_3 -free aluminum and Y_2O_3 -containing aluminum with dimensions of $10 \times 10 \times 5$ mm were polished to a mirror surface finish (roughness :0.05 μm). The polished surfaces were slightly etched using *Keller's reagent* for 10 to 15 seconds in order to remove the deformed layer caused by polishing.

The obtained load-displacement curves of Y_2O_3 -free and Y_2O_3 -containing samples are presented in Fig.4.4-1 and Fig. 4.4-2 under maximum loads of 15 μN and 20 μN , respectively. Since the maximum load was small and the maximum displacement was in the range of 5 nm, the measurements reflect the mechanical behavior of a passive film although the result may also be influenced by the substrate to some degree. In general, under a fixed load, the smaller the displacement, the harder the surface. In additions, as described in Chapter 2, the ratio (η) of the recoverable deformation energy to the total deformation energy is a measure of the contribution of elasticity to

deformation [144]. From Table 4.4-1, one may see that the surface oxide film on the Y_2O_3 -free Al sample was soft (large indentation depth) with lower η ratio, compared to those on samples containing Y_2O_3 additions. The results indicate that the mechanical properties of the passive protective films on Y_2O_3 -containing samples were improved when Y_2O_3 was added. The improved mechanical properties of the passive films on Y_2O_3 -containing samples could be attributed to possible changes in composition or structure of the passive films. A strong passive film is more protective against failure under mechanical and electrochemical attacks.

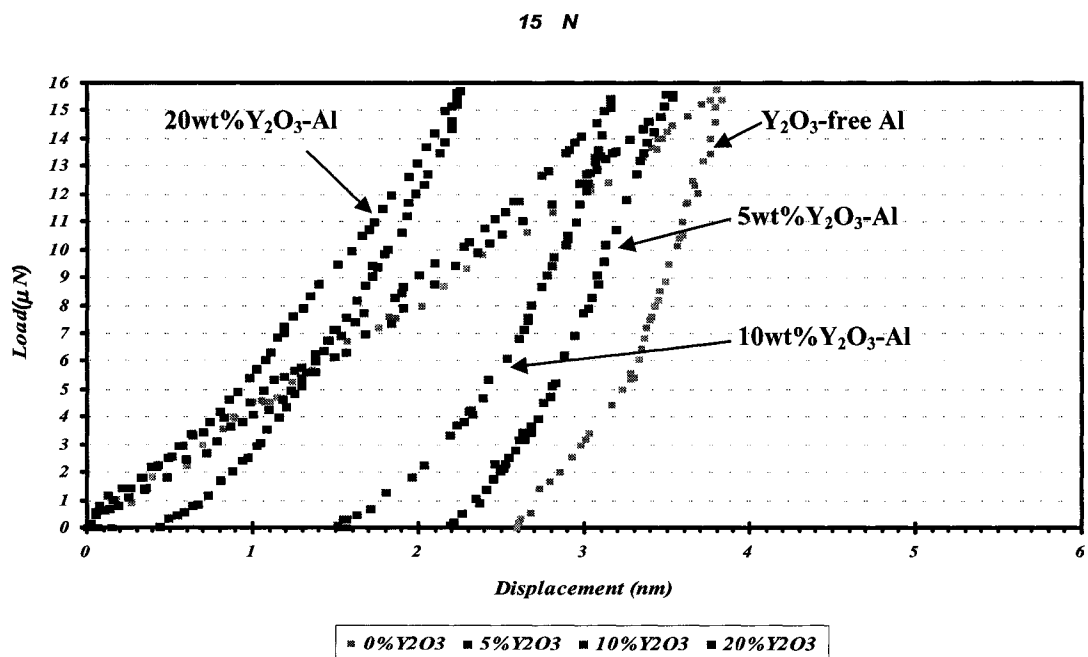


Figure 4.4-1 Nano indentation curves of Y_2O_3 -free and Y_2O_3 -containing Aluminum samples under applied load of 15 μ N.

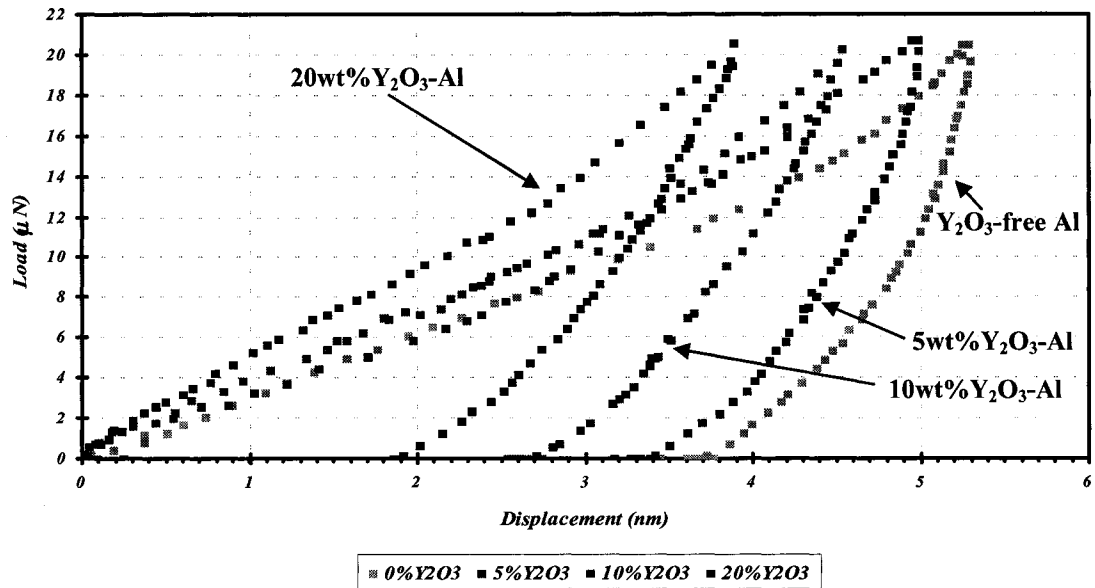


Figure 4.4-2 Nano indentation curves of Y_2O_3 -free and Y_2O_3 -containing Aluminum samples under applied load of 20 μN .

Table 4.4-1 Nanoindentation Parameters results under loads of 15 and 20 μN , respectively.

Material	Load (μN)	Maximum displacement (nm)	η (%)
Y_2O_3 -Free Al	15	3.8	31.6
	20	5.3	28.3
5Wt% Y_2O_3 -Al	15	3.5	37.2
	20	5	30
10Wt% Y_2O_3 -Al	15	3.2	53
	20	4.5	41.5
20Wt% Y_2O_3 -Al	15	2.3	82.6
	20	3.8	54

4.5 The resistance of passive film to scratching

Another critical property of a passive film is its adherence to the substrate. No matter how strong a passive film is, it may fail easily if the adhesion between the film and the substrate is poor.

A film's adhesion to the substrate could be evaluated by the scratch test. The scratch test is a commonly used method in assessing a coating's adhesion [145]. During the test, a passive film surface was scratched by a tungsten carbide tip under a normal applied load that was continuously increased. When the applied normal load exceeded a critical level, the film failed, which was determined by changes in the electrical contact resistance (ECR). By monitoring the changes in the ECR with respect to the applied load, one can determine the critical load at failure, which is related to the adherence of the passive film to the substrate.

In this study, micro-scratch tests were performed on the Y_2O_3 -free and Y_2O_3 -containing Al samples using a universal micro-tribometer made by the Center for Tribology (California, USA). A schematic of the test setup is shown in Fig. 4.5-1. The scratch tip is made of tungsten carbide having a pyramidal shape; Fig. 4.5-2 schematically shows the geometry of the tungsten carbide tip. The scratch tests were performed at a scratch speed of 0.02mm/s over a distance of 3mm. During each test, the normal load continuously increased until the passive film failed, which was determined by the rapid decrease in the electrical contact resistance. The scratch tests for each sample

were repeated six times at different locations on the sample surfaces. The repeatability was reasonably good.

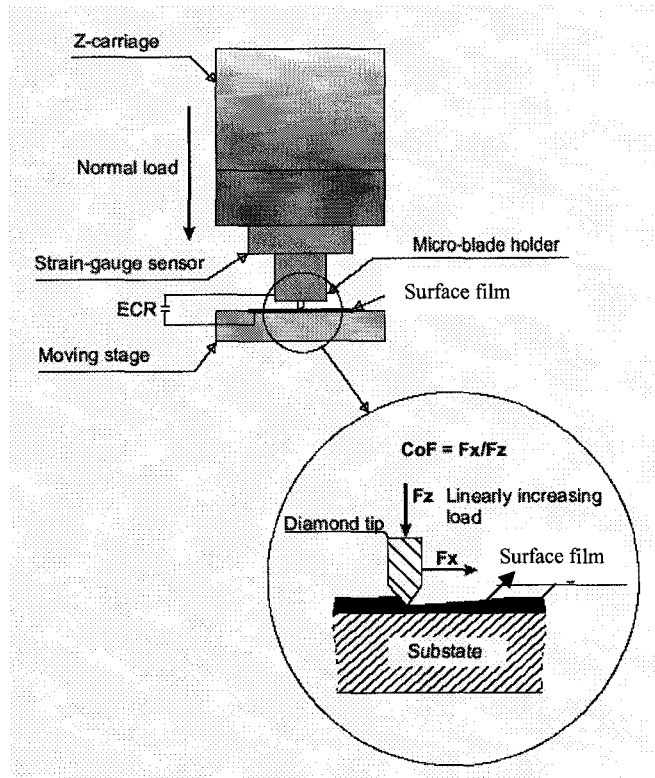


Figure 4.5-1 Schematic of test setup for scratch and adhesion tests [145].

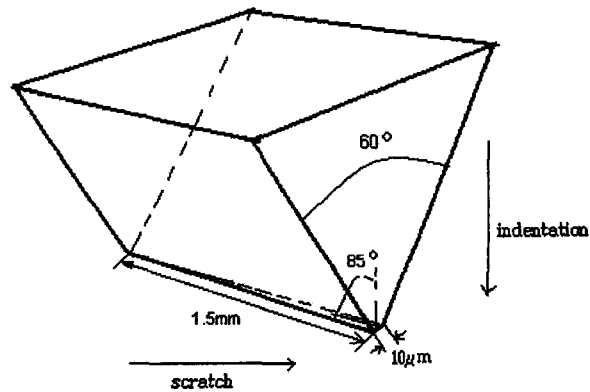
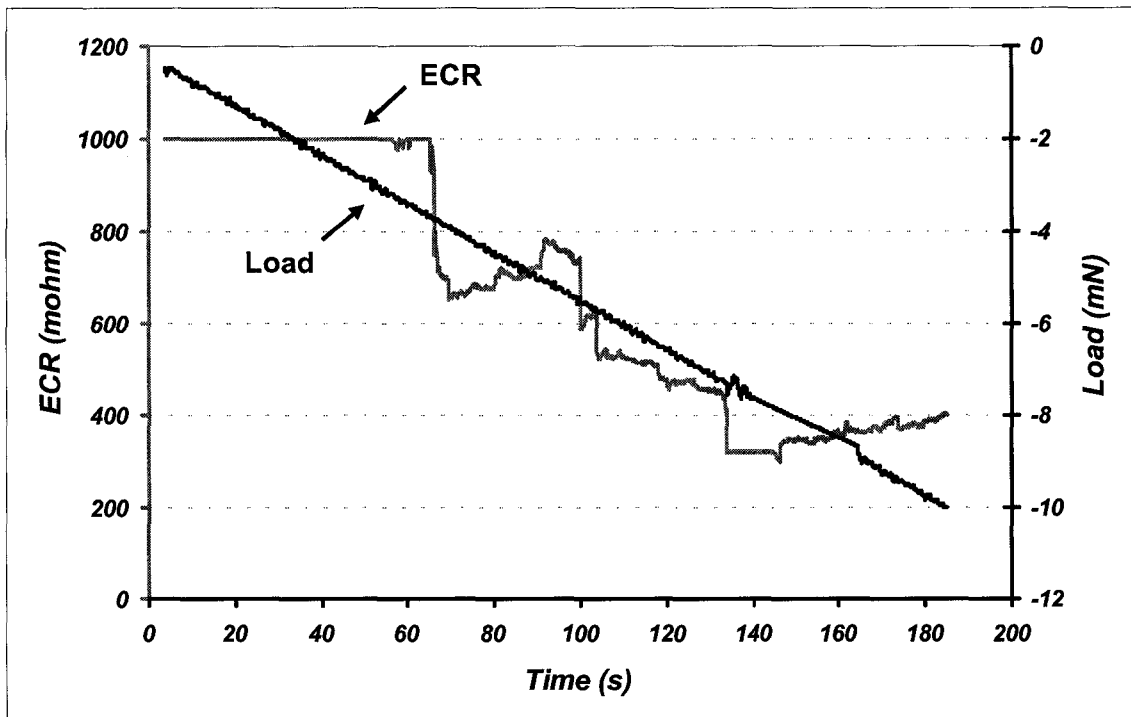


Figure 4.5-2 The geometry of the tip used in the scratch test.

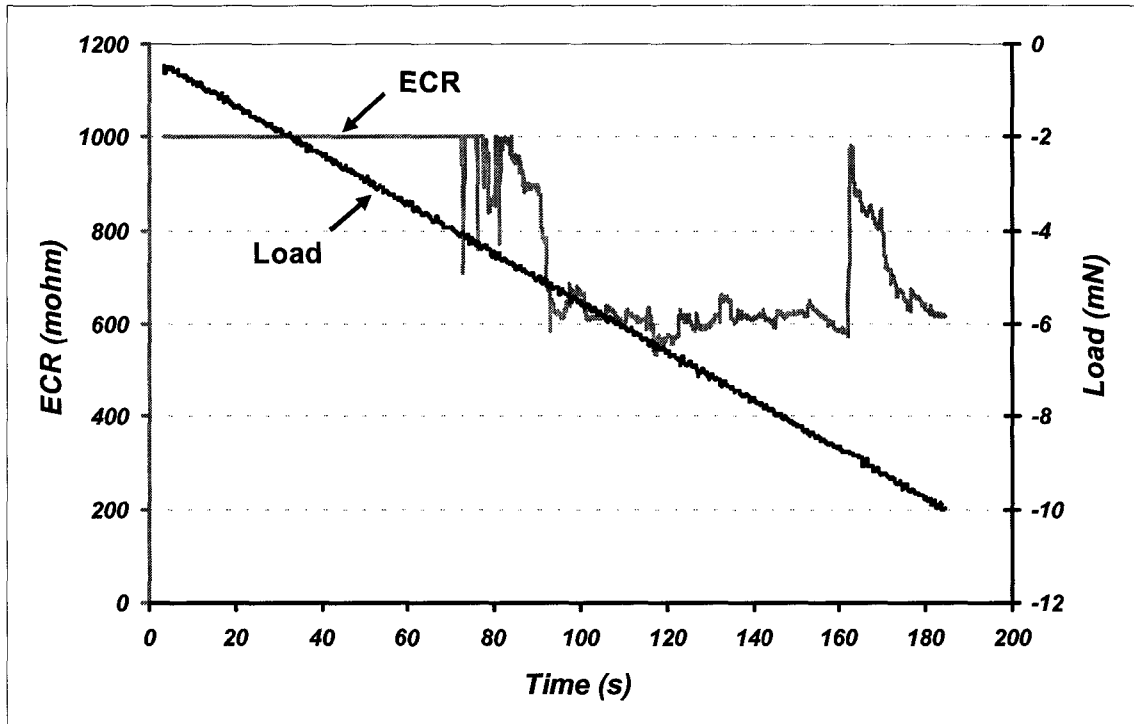
Y_2O_3 -free and Y_2O_3 -containing Al samples for scratch testing were polished to a mirror surface finish using a slurry containing alumina particles with their diameter equal to $0.05\mu m$.

Results of the scratch test are presented in Fig. 4.5-3; tested samples include Y_2O_3 -free Al, 5wt% Y_2O_3 -Al, 10wt% Y_2O_3 -Al, and 20wt% Y_2O_3 -Al.

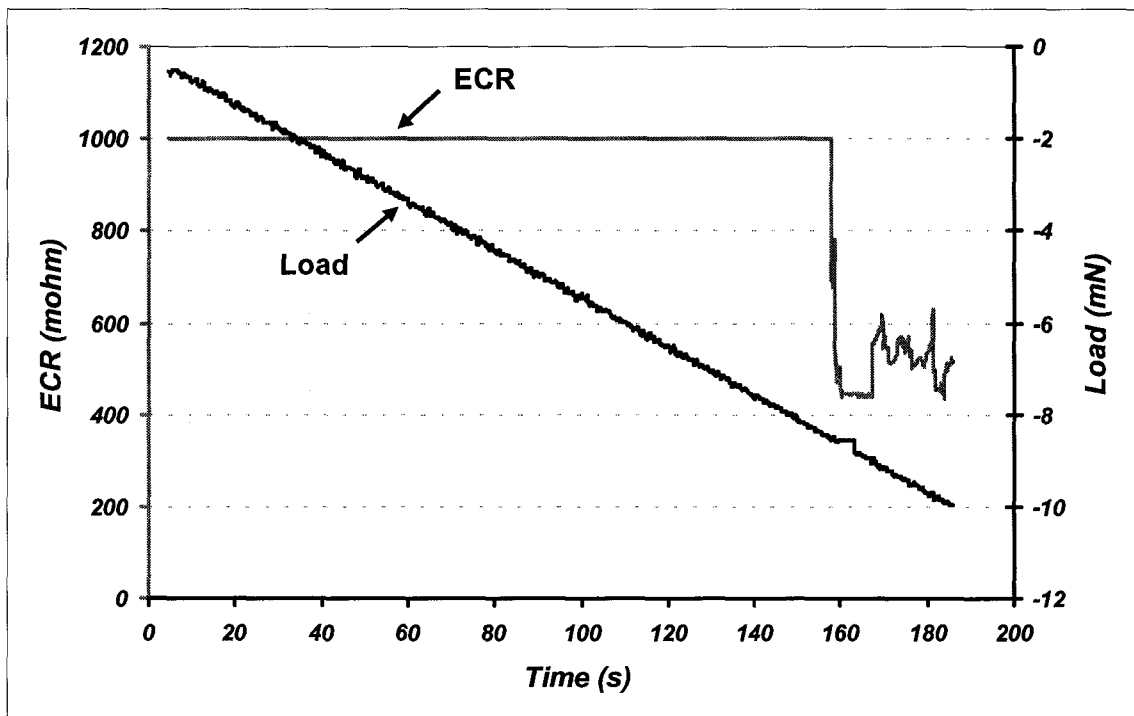
As shown in Fig. 4.5-3 a, b, c, and d, when the load was linearly increased to a certain level, a drop in electrical contact resistance (ECR) occurred, corresponding to failure of the passive film. Table 4.5-1 presents critical loads at failure for different samples. It was demonstrated that the failure loads of Y_2O_3 -containing Al samples were much higher than that for the Y_2O_3 -free Al sample. The improvement in the scratch resistance could be due to the improvement in mechanical behavior of the passive film as well as its adherence to substrate when Y_2O_3 was added.



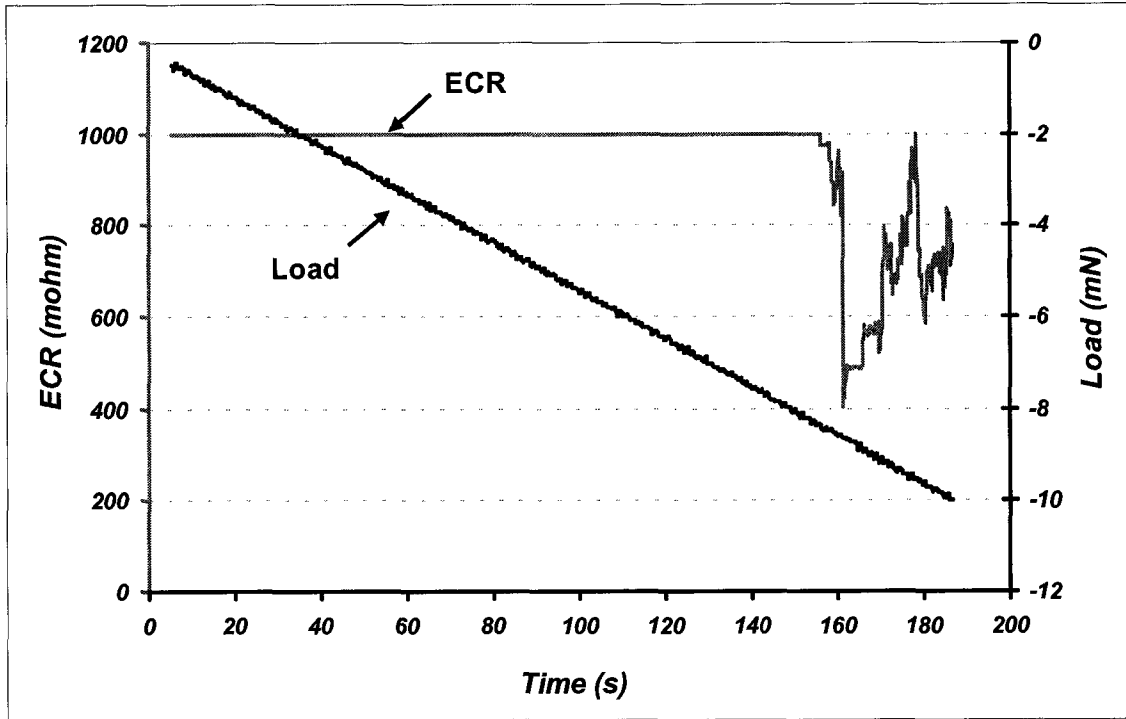
(a)



(b)



(c)



(d)

Figure 4.5-3 Electrical contact resistance (ECR) measurements ;a) Y_2O_3 -free Al, b) 5wt% Y_2O_3 -Al, c) 10wt% Y_2O_3 -Al, and d) 10wt% Y_2O_3 -Al.

Table 4.5-1 The critical failure loads of the passive film during the scratch test

Material	Failure load, F_c , (mN)
Y_2O_3 -free Al	3.6
5wt% Y_2O_3 -Al	4.1
10wt% Y_2O_3 -Al	8.4
20wt% Y_2O_3 -Al	8.5

In conclusion, adding Y_2O_3 improved the electrochemical behavior of aluminum by shifting its pitting potential in a 0.1M H_2SO_4 solution and the corrosion potential

toward more anodic potentials in a 3.5wt%NaCl solution, which means that the corrosion resistance of the metal was enhanced. The beneficial effect of Y_2O_3 additions was also demonstrated by the electrochemical scratch test, especially under higher scratching load.

However, such a beneficial effect decreased if too much Y_2O_3 was added. The improvement in the corrosion resistance may largely benefit from the enhancement of the passive film and its adherence to a substrate.

The improved electrochemical properties of aluminum should be attributed to the dissolved yttrium and the Al_3Y phase as a result of the decomposition of the originally added Y_2O_3 . As mentioned earlier, previous studies have demonstrated that rare-earth elements can increase the oxide/metal adherence, and improve the properties of oxide scale. It is believed that yttrium may also improve the adherence and mechanical properties of the passive film on aluminum which forms in a corrosive medium.

Such improvement in electrochemical behavior is beneficial to the metal when under attack of corrosive wear, as demonstrated in the next chapter.

5 Corrosive Wear of Aluminum Modified with Y_2O_3 Addition

It has been demonstrated that Y_2O_3 additions improved aluminum in terms of strength and corrosion resistance. It was consequently expected that the Y_2O_3 additions would enhance aluminum's resistance to corrosive wear.

Corrosive wear is the damage to a material by synergistic attack of wear and corrosion. The resultant material loss could be significantly larger than those respectively caused by wear or corrosion. This happens because a corrosively degraded surface has a higher wear rate and resultant fresh metal is vulnerable to corrosion and thus corrodes quickly.

Even for passive alloys, under the synergistic attack of wear and corrosion, they may become ineffective as non-passive alloys. The strong destructive effect of the combined mode of corrosion and wear is due to the fact that corrosion accelerated is due to the damage of passive films and plastic deformation as well as other defects. A highly irregular surface with residual oxide debris may enhance surface stress concentration, thus leading to a high wear rate. On the other hand, the failure of the passive film makes the surface more susceptible to corrosion, resulting in greater material loss. The lattice defects introduced by wear also promotes corrosion and thus promotes the synergism of wear and corrosion. Many industrial facilities are subjected to wear in corrosive environments, which cause large capital losses on repair and replacement of industrial facilities and resultant energy consumption, lost of productivity, and industrial accidents.

Corrosive wear has considerable impact on many industrial sectors, such as mining and mineral, chemical, petroleum, and oilsand processing.

5.1 Corrosive wear mechanism

The phenomena of corrosive wear is rather complex, and its quantitative analysis is still in its infancy. Corrosive wear can, however, be qualitatively analyzed in order to evaluate the effect of wear-corrosion synergism on the overall wear rate. Although it is not easy to quantitatively determine the roles that corrosion and wear play during a corrosive wear process, mutual effects of wear and corrosion on each other have been understood to some degrees.

5.1.1 Effect of corrosion on wear

In a corrosive environment, a metallic material may degrade with formation of loosely packed corrosion product, oxide scale. Such a oxide scale can be easily removed by the wearing force. Compared to wear without corrosion, the removal of material is considerably increased. Since corrosion is spatially inhomogeneous due to residual stress, lattice defects and second phases, stress concentration may be increased, thus resulting in a higher wear rate when corrosion is involved.

5.1.2 Effect of wear on corrosion

Corrosion can promote wear and, on the other hand, wear can also accelerate corrosion. The wearing force removes the oxide scale and thus increases fresh metal surface area for further corrosion. The wearing force also increases inhomogeneous plastic strain in the surface layer which promotes material dissolution and establishes microelectrodes that further accelerate electrochemical reactions.

Passive alloys have high resistance to corrosion due to the formation of protective passive films that prevent further corrosion. However, when wear is involved, the passive films could be damaged by the wearing force. As a result, a passive alloy could be as ineffective as a non-passive alloy during a corrosive wear process.

In summary, during a corrosive wear process, corrosion and wear interact and promote each other. Such interaction is known as the wear-corrosion synergism, which leads to significantly larger material loss.

5.2 Evaluation of wear-corrosion synergism

As corrosive wear involves different failure modes and mechanisms, material damage is hard to be predicted on the basis of separate wear and corrosion processes [146]. Therefore, understanding the phenomena of corrosion and wear and their interaction are of importance to the development of effective materials against corrosive wear.

Many researchers [147-159] have studied the synergism between wear and corrosion. The total material loss may be divided into three components as follows;

$$T = W + C + S \quad (5.2-1)$$

where T is the total volume loss, W is the volume loss caused by wear only, C is the volume caused by to corrosion only, and S is the volume resulting from the synergism of corrosion and wear.

T , W and C can be experimentally determined [160]. The pure wear (W) could be determined under a cathodic protection condition that may minimize corrosion effect. While the corrosion loss (C) may be determined without mechanical wear involved. The total volume loss (T) can be determined by directly measuring volume loss of a specimen that experiences corrosive wear without any applied potential. Once T , W and C are determined, the volume loss caused by the wear-corrosion synergism, S , could be determined as;

$$S = T - (W+C) \quad (5.2-2)$$

Although the above mentioned method still has some difficulty for accurate determination of pure wear due to the possible influence of the cathodic potential on the mechanical properties of the material, it has been used by researchers to investigate corrosive wear.

The volume loss caused by the wear-corrosion synergism, S , includes two components, one is the increase in wear due to corrosion (S_1), and the other is the increase in corrosion due to wear (S_2).

$$S = S_1 + S_2 \quad (5.2-3)$$

Wang and Li [161] recently proposed an electrochemical scratch/wear method to determine S_1 and S_2 . By performing the scratch/wear test under an applied potential, we may determine the amount of additional material dissolution caused by the scratching or wearing force, which is related to S_2 . Consequently, S_1 can be determined, which is equal to $S - S_2$.

5.3 Effects of Y_2O_3 additions on corrosive wear of aluminum

5.3.1 Experimental details

The wear behavior of Y_2O_3 -free Al and Y_2O_3 -containing Al samples in dry and corrosive media was evaluated using a pin-on-disk tribometer (CSEM THT) illustrated in Fig. 5.3-1. The pin was a Si_3N_4 ball with a diameter of 6mm. Wear tests were carried out at room temperature under normal loads of 1, 2, and 3N, respectively, at a sliding speed of 2 cm/s for 500 rotations with a radius of 1.5mm.

The corrosive wear tests were performed respectively in two different corrosive environments, a 0.1M H₂SO₄ solution and a 3.5wt% NaCl solution.

The dry wear test was performed in ambient atmosphere. Volume losses of the samples caused by wear were determined using an optical microscope with capability for image analysis.

Before conducting any of the tests, samples of Y₂O₃-free Al and Y₂O₃-containing aluminum were cut from casts and their final dimensions were 15×10×5 mm. The samples were polished using grit 600 sand papers. Care was taken to ensure the front and back surfaces of the samples were parallel to each other so that the wear track was homogeneous. In the corrosive wear test, a sample was placed in a plastic cup and the wear test performed in a corrosive solution. The measured volume loss was an average of four measurements. The variation of the measured volume loss was in the range of ± 5% to ± 12%.

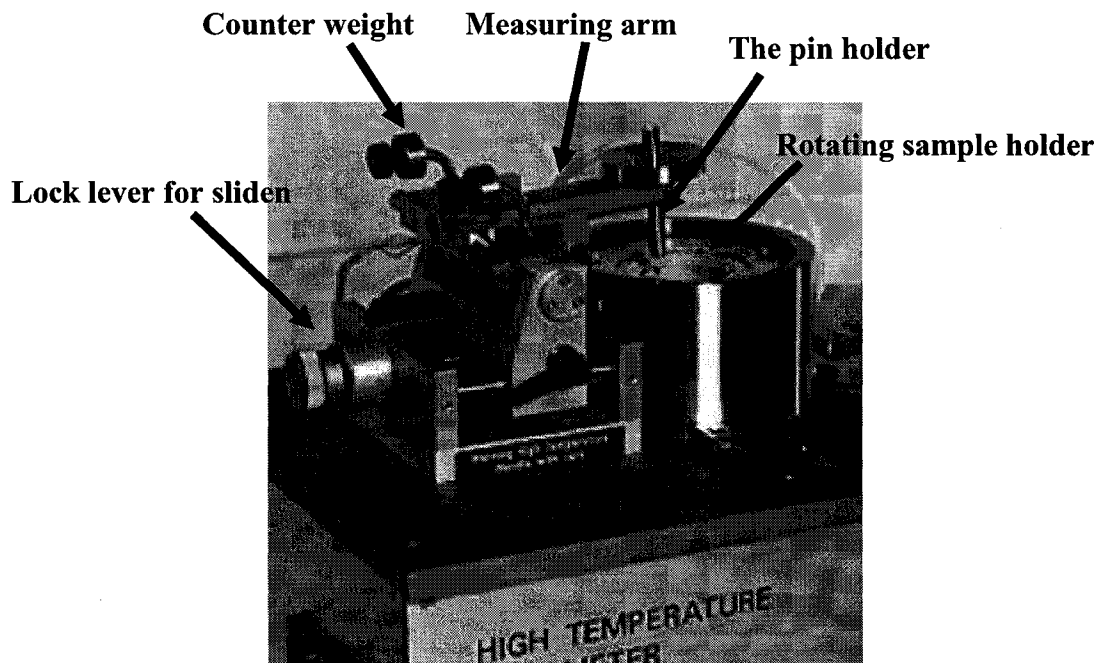


Figure 5.3-1 A pin-one-disk tribometer for wear test.

5.3.2 Results and discussion

5.3.2.1 Dry sliding wear behavior

Wear losses of the tested materials as a function of applied load were measured and results are presented in Fig. 5.3-2. As demonstrated, the wear losses increased with an increase in the applied load for all samples (Y_2O_3 -free Al and Y_2O_3 -containing samples) under the dry sliding condition. Among these samples, the wear loss of Y_2O_3 -free Al sample was considerably higher than those of Y_2O_3 -containing samples. Among the Y_2O_3 -containing samples, the sample added with 20wt% Y_2O_3 exhibited the lowest wear loss. Apparently, the wear loss decreased with an increase in the Y_2O_3 content in the range of Y_2O_3 content under the study.

This enhanced sliding wear resistance should be related to the improved mechanical properties of the Y_2O_3 -containing samples. It was demonstrated in chapter 2, the added Y_2O_3 increased the hardness of aluminum due to the formation of Al_3Y phase and modified eutectic microstructure after the Y_2O_3 being decomposed during the melting process. In the sample containing 20wt% Y_2O_3 , the wear performance of this alloy was superior to that of other Y_2O_3 -containing Al samples. The wear testing results are consistent with results of macro-hardness, micro-hardness, and the nanoindentation tests which showed that hardness of the material increased with an increase in the Y_2O_3 content. Since the wear resistance of a material is proportional to its hardness of material (Archard's equation, equation 2.2-1), the added Y_2O_3 increased the hardness of aluminum, and thus its resistance to wear.

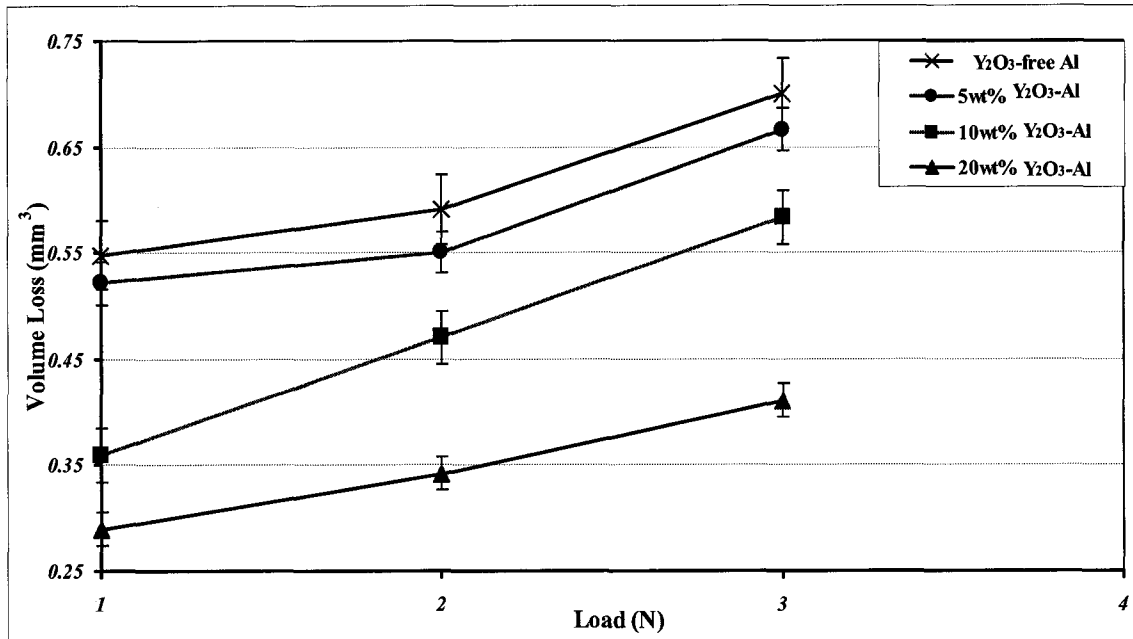


Figure 5.3-2. Dry wear loss of Y₂O₃-free and Y₂O₃-containing Al samples against the applied load.

5.3.2.2 Corrosive wear behavior

Sliding wear behavior of all Y₂O₃-free and Y₂O₃-containing Al samples in a 0.1M H₂SO₄ solution and a 3.5wt% NaCl solution was evaluated and results are presented in Fig.5.3-3 and Fig.5.3-4, respectively. The tests demonstrated considerably improved performance of samples added with Y₂O₃. The Y₂O₃-free sample showed the greatest wear. For the Y₂O₃-containing Al samples, their wear loss decreased with an increase in the Y₂O₃ content.

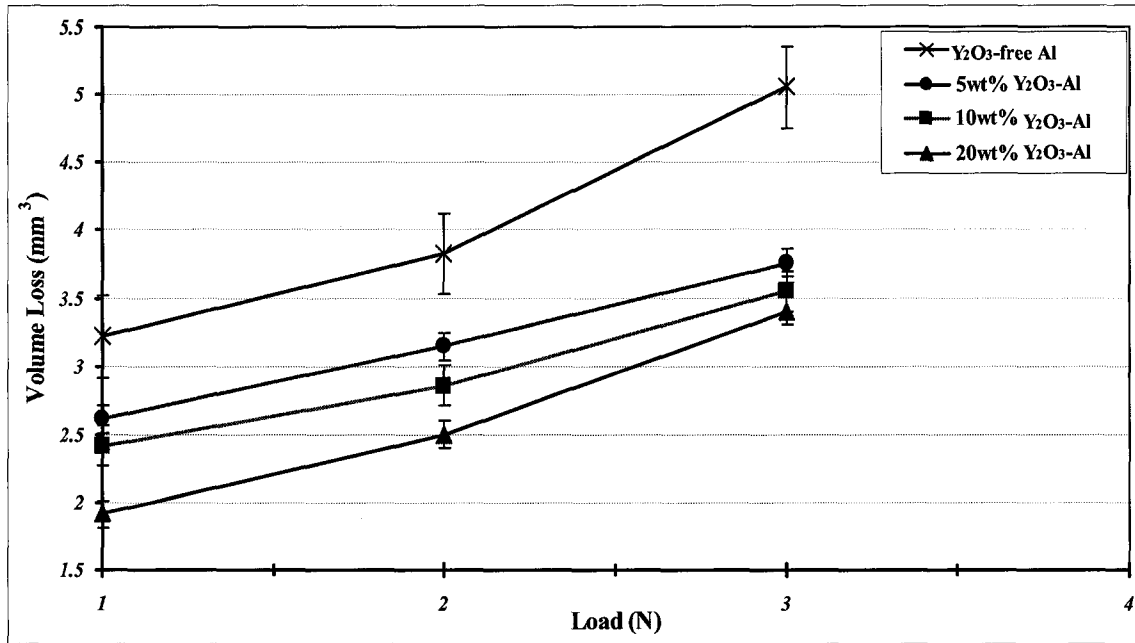


Figure 5.3-3. Wear losses of Y₂O₃-free and Y₂O₃-containing Al samples with respect to the applied load in a 0.1M H₂SO₄ solution.

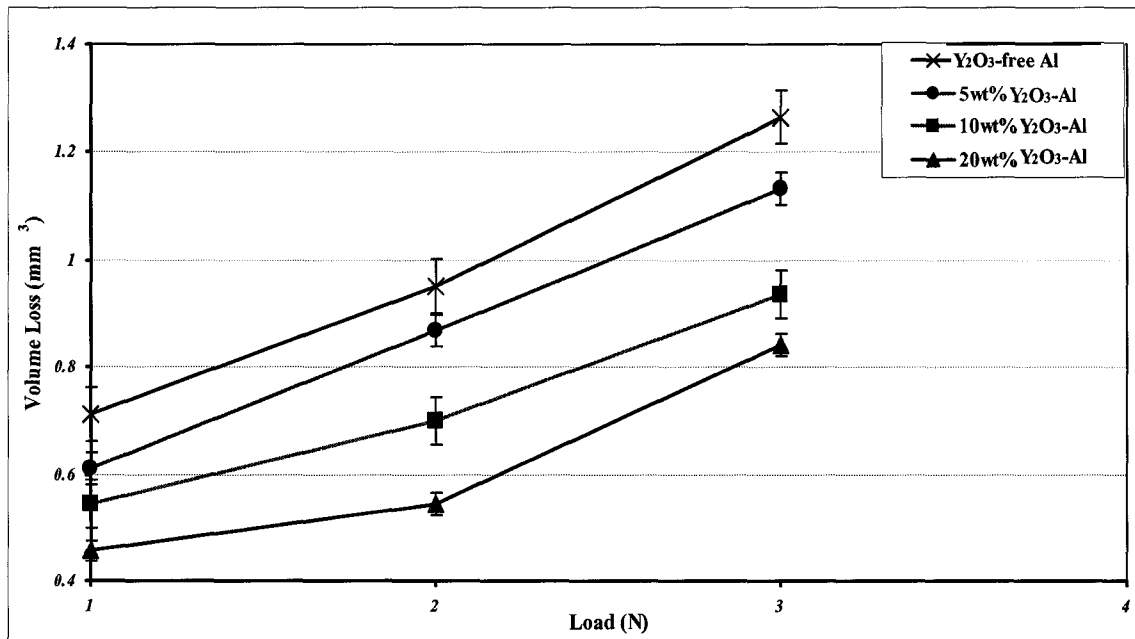


Figure 5.3-4 Wear losses of Y₂O₃-free and Y₂O₃-containing Al samples with respect to the applied load in a 3.5wt% NaCl solution.

The enhanced resistance of aluminum with Y_2O_3 additions to the synergistic attack of corrosion and wear in both 0.1 M H_2SO_4 and 3.5wt% NaCl solutions were attributed not only to improved mechanical properties of the metal caused by the Y_2O_3 additions, but also to its improved corrosion resistance and enhanced passive film on the Y_2O_3 -containing Al samples.

When mechanical properties and electrochemical properties were improved, both corrosion and wear were suppressed, thus resulting in higher resistance to corrosive wear.

In conclusion, the added Y_2O_3 improved the corrosive wear resistance of aluminum in both 0.1 M H_2SO_4 and 3.5wt% NaCl solutions as a result of improvements in corrosion resistance, mechanical and Tribological properties of both the substrate and its passive film.

The testing data was consistent with previous studies on the improvement in the resistance of the metal to corrosive wear by adding metallic yttrium. Yttria has also demonstrated its beneficial effect on the polarization behavior and mechanical properties of the metal and as well as passive film [28,44,119-123]. This research has demonstrated that yttria can play a similar role as yttrium does.

As mentioned earlier, yttria is inexpensive and easy to handle, compared to yttrium. It is explored that yttria would find more applications in the field of tribology and wear of materials.

Such an improvement resulted from the formation of the Al_3Y phase and modified eutectic microstructure. The improvement might also benefit from the possible existence of residual yttrium in the material. These modifications to microstructure of aluminum improved the metal with higher resistance to wear, corrosion, and corrosive wear.

6 Summary and Future Work

In the previous chapters, material processing, microstructure, mechanical and electrochemical behavior, and corrosive wear behavior of Y_2O_3 -free and Y_2O_3 -containing Al samples were reported in details. It was demonstrated that the Y_2O_3 addition modified the eutectic microstructure and improved the mechanical properties and the electrochemical behavior of aluminum. The electrochemical behavior, mechanical behavior and the adherence of the formed passive film on the Y_2O_3 -containing samples were also enhanced. These improvements resulted in enhanced performance of aluminum during wear in 0.1M H_2SO_4 and 3.5wt% $NaCl$ solutions. It was suggested that the improved performance of aluminum modified with Y_2O_3 is mainly attributed to the formed Al_3Y phase, which was resulted from the possible decomposition or melting of the originally added Y_2O_3 . Although there were no available thermodynamics data to show any possible decomposition or reducing of Y_2O_3 by aluminum, the experimental results of this work did show that the absence of Y_2O_3 particles in the Y_2O_3 -containing aluminum. The XRD, SEM and EDX results suggest that the added Y_2O_3 was decomposed or melted. The released yttrium reacted with aluminum to form Al_3Y phase, which was demonstrated by SEM, EDX and XRD analyses. Since yttrium and other rare-earth elements are expensive, active and hard to handle during material processing, the investigated decomposition of inexpensive Y_2O_3 particles can have great impact on the application of rare-earth oxides in replacing reactive metallic yttrium to enhance performance of aluminum alloys during corrosive wear. Accordingly, investigation on the

mechanism responsible for the decomposition of Y_2O_3 in aluminum is important for both fundamental understanding and industrial application of rare-earth oxide.

The first section of this chapter summarizes the current work about the effects of Y_2O_3 on the performance of aluminum to corrosive wear, while the second discusses future work with the emphasis on the decomposition of Y_2O_3 based on experimental investigations.

6.1 Summary of the thesis

As mentioned earlier that the added Y_2O_3 enhanced the performance of aluminum during corrosion and wear due to the improvement in mechanical and electrochemical behavior of aluminum. Summaries are made as follows.

1. Eutectic microstructure developed during melting when Y_2O_3 particles were added to aluminum. However, the Y_2O_3 particles were somehow melted or decomposed; the released yttrium reacted with aluminum to form Al_3Y phase. The final eutectic microstructure consisted of aluminum dendrites domains and Al_3Y -aluminum mixture. The Al_3Y phase grew up when the content of Y_2O_3 was increased.
2. Y_2O_3 additions strengthened aluminum due to the second phase strengthening mechanism. Since the solubility of yttrium in aluminum is limited to less than 0.1wt% Y, the precipitation of Al_3Y could play a predominate role in strengthening the

material. The Al_3Y may exist in the eutectic mixture that helps to block dislocation motion and thus suppress the plastic flow. Larger $\alpha-Al_3Y$ precipitates in samples containing more Y_2O_3 such as 20wt% Y_2O_3 -containing aluminum sample also provide more barriers to dislocation movement, thus further hardening the material.

3. The corrosion resistance of Y_2O_3 -containing samples was enhanced. Y_2O_3 additions improved the electrochemical behavior of aluminum by shifting its pitting potential in the 0.1M H_2SO_4 solution and the corrosion potential toward more anodic potentials in a 3.5wt%NaCl solution, thus enhancing the corrosion resistance of the metal. The beneficial effect of Y_2O_3 additions was also demonstrated by the electrochemical scratch test, especially under higher scratching loads. However, such a beneficial effect decreased if too much Y_2O_3 was added. The improvement in the corrosion resistance may largely benefit from the enhancement of the passive film and its adherence to the substrate.

The improved electrochemical properties of aluminum should be attributed to possibly dissolved yttrium and Al_3Y phase resulted from the decomposition of the originally added Y_2O_3 .

The mechanical behavior and the resistance to scratch of the passive film on the Y_2O_3 -containing samples were improved. It is believed that the passive film adherence to its substrate in the Y_2O_3 -containing samples was also improved.

4. The improved mechanical properties and electrochemical behavior of Y_2O_3 -containing samples and their passive films, resulted in enhanced resistance to corrosive wear of aluminum in 0.1 M H_2SO_4 and 3.5wt% NaCl solutions. Such an improvement resulted from the formation of Al_3Y phase and modified eutectic microstructure. The improvement might also benefit from possibly existence of residual yttrium in the material.

6.2 Possible Future Work

It was demonstrated by the microstructural observation (SEM, EDX and XRD), presented in chapter 2, that there was no indication of the presence of originally added Y_2O_3 in aluminum. Instead, a yttrium compound, Al_3Y , was observed, which raises a question that whether or not the originally added Y_2O_3 was decomposed, or was melted during the arc melting process. In order to provide more information regarding the decomposition of the originally added Y_2O_3 , sintered preliminary examination was made to Y_2O_3/Al samples. Details of the work are presented in the next section.

6.2.1 Material Processing and sintering

Aluminum samples containing 5, 10, and 20 wt.% Y_2O_3 powder were prepared by mixing commercial pure aluminum powder (99.8%) with particle size of -40 to +325 Mesh (420 to 44 μm) with Y_2O_3 powder having its particle size smaller than 10 μm .

During sample preparation, Al and Y_2O_3 powders were mixed in a plastic bottle with a size of 60 mm in diameter and 120 mm in height. A number of alumina milling balls were put into the bottle to prevent any agglomeration of the Y_2O_3 particles and to ensure a homogenous powder's mixture. The bottle was then rotated at a speed of 155 rpm on a mill apparatus in air for 10 hours.

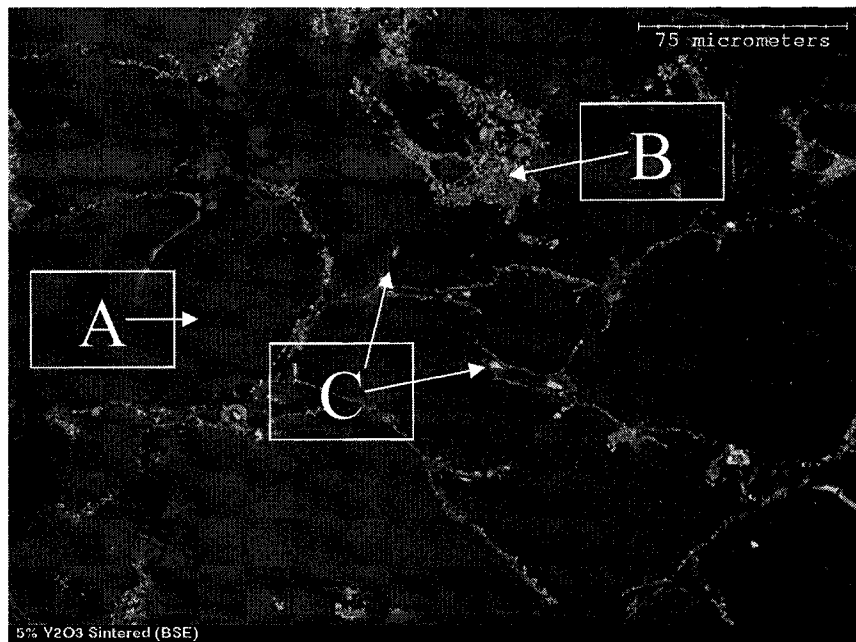
The mixed powder was then loaded into a tool steel compaction die having a size of 1" in diameter, (25.4mm diameter). The die's wall and punches were lubricated using SILCHEM mould release spray before the powders were loaded into it for easy removal of a sample from the die after compaction. A Carver laboratory press machine was used to press the die under a compaction load of 24,000 Lbs, (11 Tons). The die was kept under the compaction load for 5 minutes.

Sintering process was performed in an environment protected furnace. Argon gas was used as the protective medium. Before turning the furnace on and at room temperature, argon gas let to flush into the furnace through the inlet of a mullite tube where samples were placed for 10 minutes to flush air away from inside the tube. The sample was placed in alumina boat inside the mullite tube. All samples were sintered at 630°C for 8 hours. During the sintering process, argon gas flow was maintained. All samples cooled in furnace with a flow of argon gas to minimize any possibility of oxidation when the samples were still hot.

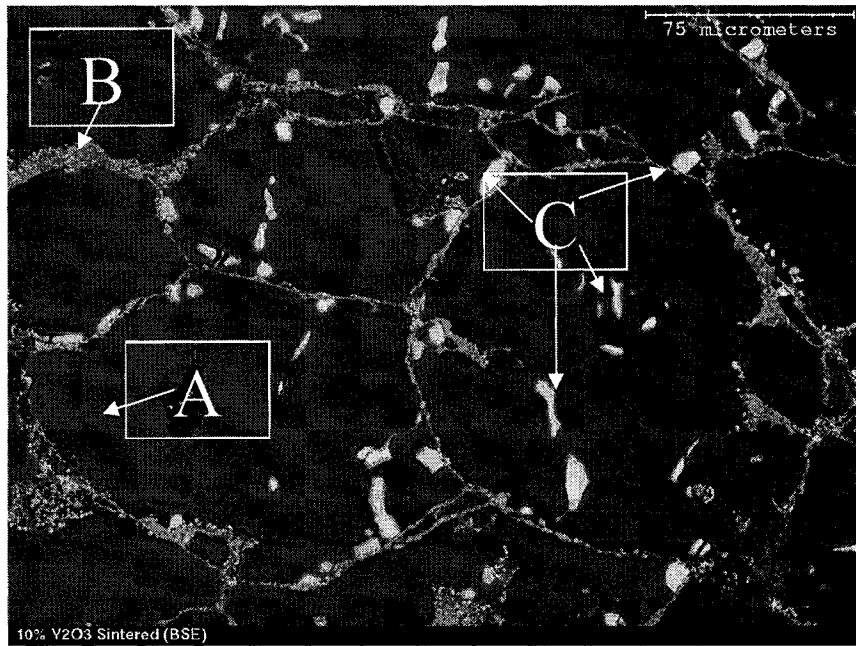
6.2.2 Microstructural observation

Y_2O_3 -free Al and Y_2O_3 -containing Al samples were cut from the sintered materials using an ISOMET 2000 linear precision cooled saw. The samples having dimensions of $5 \times 10 \times 10$ mm were mounted in epoxy resin, polished to $0.05\mu\text{m}$ (roughness) and etched for 1 minute using a *Keller's reagent* (2mL HF (48%), 3mL HCl (con), 5mL HNO_3 (con), 190mL water). SEM and EDX were used to examine 5, 10, 20wt% Y_2O_3 -containing Al samples using a PGT PRISM SEM/EDX system.

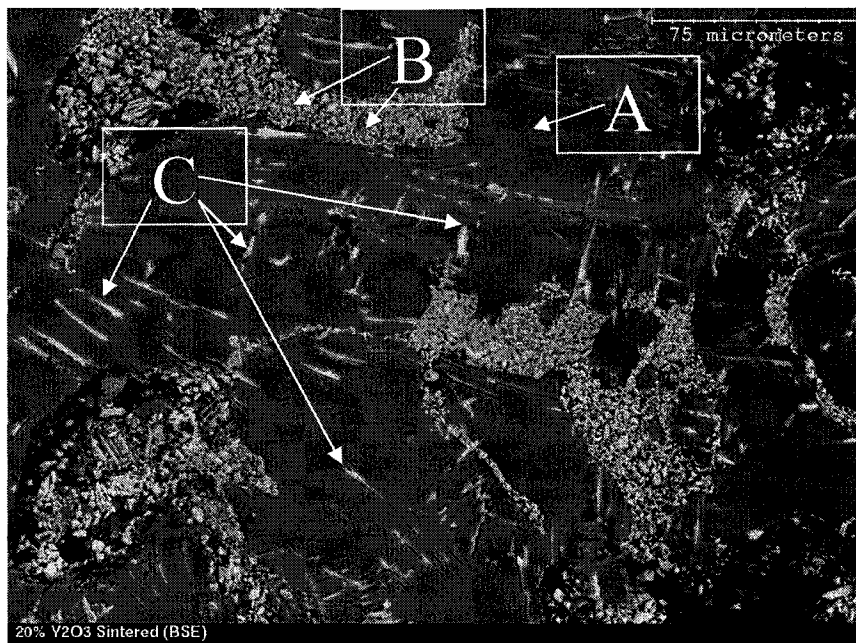
Fig. 6.2-1 illustrates backscattered electron image of sintered aluminum with different Y_2O_3 contents; (a) 5wt% Y_2O_3 , (b) 10wt% Y_2O_3 , and (c) 20wt% Y_2O_3 , respectively.



(a)



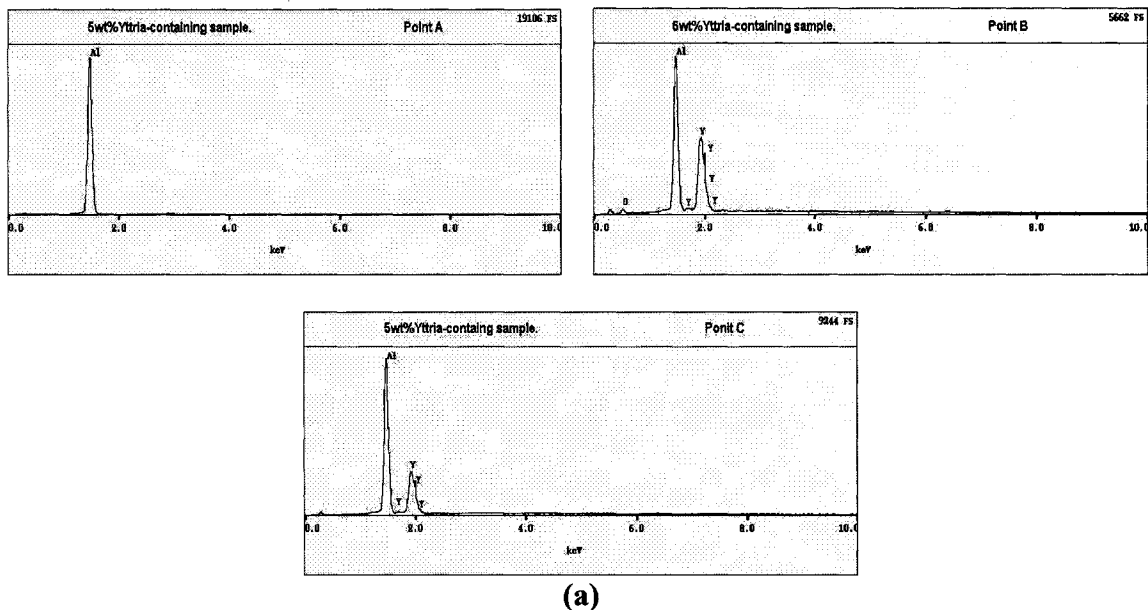
(b)

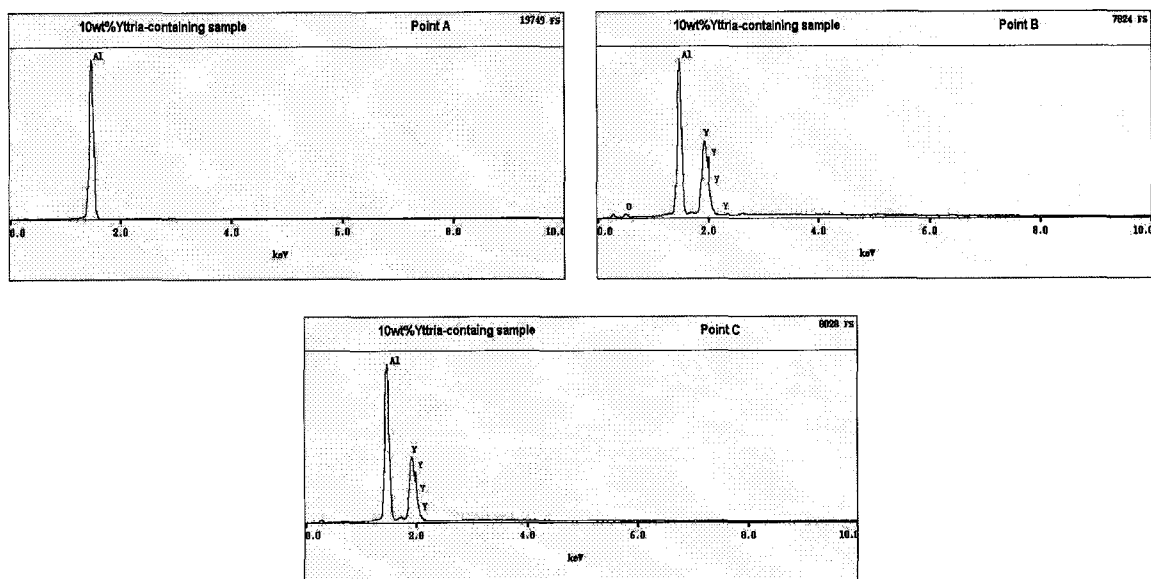


(c)

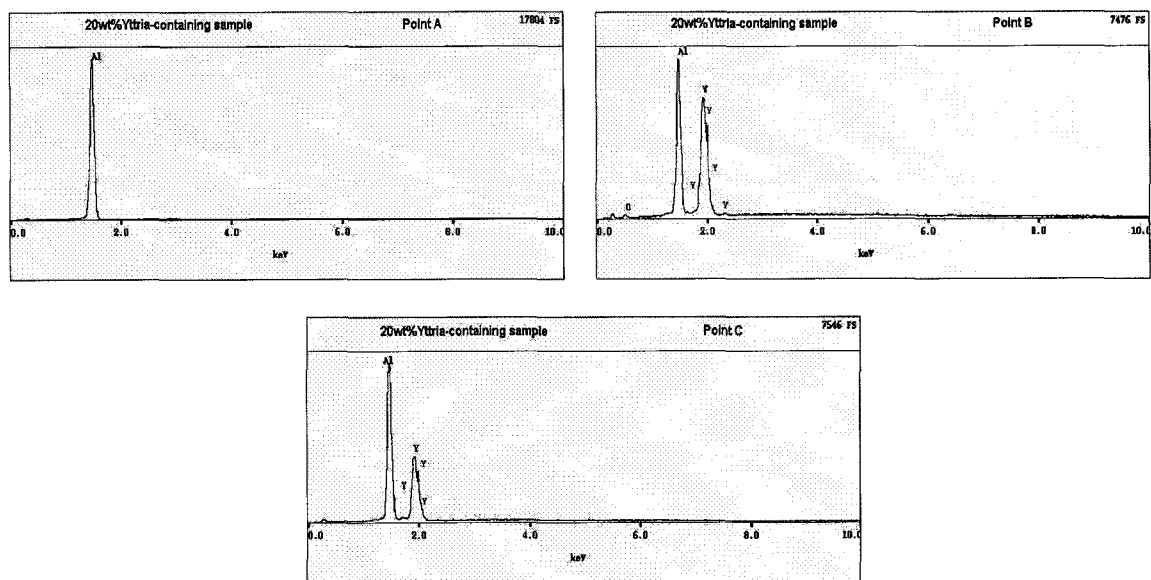
Figure 6.2-1 SEM images of samples sintered at 630°C for 8 hours: (a) 5wt% Y_2O_3 -containing Al, (b) 10wt% Y_2O_3 -containing Al, (c) 20wt% Y_2O_3 -containing

From Fig. 6.2-1, one may see two different domains. The first is the dark domain which is believed to be a pure aluminum contains bright particles that are most probably a Y-rich phase. The second is the domain that seems to contain accumulated particles surrounding the dark domain. The bright particles in the dark domain seem to be increased and more detectable when the amount of Y_2O_3 increased in 10 and 20wt% Y_2O_3 -containing samples than that in 5wt% Y_2O_3 -containing sample. For further microstructural investigation, points were chosen at different domains in the microstructure of 5, 10 and 20wt% Y_2O_3 -containing samples for EDX analysis, as Fig. 6.2-1 illustrates. Point (A), is the dark domain which is believed to be a pure aluminum, point (B), is a domain consisting of accumulated particles. Point (C) is a bright domain. Fig. 6.2-2; a) illustrates EDX peaks of 5 wt% Y_2O_3 , b) 10 wt% Y_2O_3 and c) 20 wt% Y_2O_3 -containing samples, respectively. Compositions of points A, B and C in different samples were examined.





(b)



(c)

Figure 6.2-2 EDX peaks for different points illustrated in Fig.6.2-1; a) 5wt% Y_2O_3 -containing Al, b) 10 wt% Y_2O_3 -containing Al, c) 20 wt% Y_2O_3 -containing Al.

The obtained chemical composition of the different points on each sample is given in Table 6.2-1.

EDX analysis shows that the dark domain (A) in Fig. 6.2-1 a), b), and c) was pure aluminum, while the domains of the accumulated particles (B) in the same figure, Fig. 6.2-1 a), b), and c), contained aluminum, Yttrium, and oxygen, which might be cluster of Y_2O_3 particles. The bright spots (C) in Fig. 6.2-1 a), b), and c) showed different compositions. From the EDX analysis, those spots are not Y_2O_3 particles, since they only contained yttrium and aluminum and there was no any indication of oxygen content.

Table 6.2-1 Chemical composition of sintered 5, 10, and 20wt% Y_2O_3 -containing Al samples.

Material	Overall Wt%			Dark domain, (A), Wt%			Accumulated particles, (B), Wt%			Bright spots, (C), Wt%		
	Al	Y	O	Al	Y	O	Al	Y	O	Al	Y	O
5wt% Y_2O_3	90.9	9.1	0.0	100	0.0	0.0	35.6	51.6	12.8	47	53	0.0
10wt% Y_2O_3	85.3	13.1	1.7	100	0.0	0.0	35	52.2	12.8	39.5	60.5	0.0
20wt% Y_2O_3	79.3	18.6	2.1	100	0.0	0.0	35.3	51.9	12.8	39.5	60.5	0.0

The EDX analysis implies that portion of Y_2O_3 particles decomposed during the sintering process and reacted with aluminum to form Y-Al compound probably the Al_3Y phase. The appearance of the formed phase is similar to that formed during the arc melting process (see chapter 2).

The microstructure of Y_2O_3 -containing Al after sintering demonstrates that decomposition of Y_2O_3 to metallic yttrium is possible not only during melting but also during sintering at $630^\circ C$. This brings potential application of inexpensive Y_2O_3 particles in replacing expensive and reactive metallic yttrium for applications whereas yttrium is expected to improve mechanical and electrochemical properties.

Further comprehensive study on the mechanism responsible for the decomposition of Y_2O_3 and the formation of Y-rich phases during melting and sintering processes is recommended.

References

1. Lipson, C., *Wear Considerations in Design*. Fundamentals in Engineering Design, ed. J.B. Reswick. 1967, New Jersey: Prentice-Hall Series in Engineering Design.
2. Eyre, T.S., *Wear Resistance of Metals*. Wear, ed. T. O. M. S. A. Technology, 1979. **13**.
3. Davis, J.R., *Surface Engineering For Corrosion And Wear Resistance*. 1st ed. 2001: ASM.
4. Bowden, F.P. and D. Tabor, *The Friction and Lubrication of Solids*. Clarendon Press. Vol. I, II. 1964, Oxford: University of Oxford Press.
5. Buckley, D.H., *Surface Effects in Adhesion, Friction, Wear and Lubrication*. Tribology Series. Vol. 5. 1981, Amsterdam: Elsevier.
6. Czichos, H., Journal of Physics "Applied Physics", 1972. **5**: p. 1890-1897.
7. Eley, D.D. and R. Rudham, *Adhesion Fundamentals and Practice*. 1969, London: McLaren and Sons.
8. Maugis, D., *Adherence in Solids, in Microscopic Aspects of Adhesion and Lubrication*. Tribology Series. Vol. 7. 1982, Amsterdam: Elsevier.
9. Sikorski, M.E., Wear, 1964. **7**: p. 144-162.
10. Ernest, R., *A study of abrasion wear under three-bodies conditions*. Wear, 1961. **4**: p. 345-351.
11. Ernest, R., *Friction and Wear of Materials*. 1st. ed, ed. W.S.o.t.S.a.T.o. Materials. 1965: John Wiley and Sons, Inc.

12. Gahr, K.-H.Z., *Microstructure and Wear of Materials*. 1st. ed. Tribology Series. Vol. 10. 1987, Amsterdam: Elsevier Science.
13. Bitter, J.G.A., *Wear*, 1963. **6**(5-21): p. 169-190.
14. Raask, E., *Erosion Wear in Coal Utilization*. 1st. ed. 1961, Berlin: Hemisphere.
15. Rao, P.V. and D.H. Buckley. *Erosion by Liquid and Solid Impact*. in *Proc. 6th Int. Conf.* 1983. Cambridge, England.
16. Ruff, A.W. and S.M. Wiederhorn, *Mater. Sci. Technol.*, 1979. **16**: p. 69-126.
17. Said, J., *Friction and Wear of Ceramics*. 1st. ed. Materials Engineering, ed. N.I.o.S.a. Technology. 1994, Gaithersburg, Maryland: Marcel Dekker, Inc.
18. Tilly, G.P., *Wear*, 1973. **23**: p. 87-96.
19. Tilly, G.P., *Mater. Sci. Technol.*, 1979. **13**: p. 287-319.
20. Winter, R.E. and I.M. Hutchings, *Wear*, 1974. **29**: p. 181-194.
21. Uhlig, H.H. and R.W. Revie, *Corrosion and Corrosion Control*. 3rd. ed. An Introduction to Corrosion Science and Engineering. 1985, New York: John Wiley and Sons, Inc.
22. Ulick, R.E., *An Introduction to Metallic Corrosion*. 3rd. ed. 1981, England: Edward Arnold Ltd.
23. West, J.M., *Basic Corrosion and Oxidation*. 2nd. ed. 1986, England: Ellis Horwood Ltd.
24. Wranglen, G., *An Introduction to Corrosion and Protection of Metals*. 1st. ed. 1985, Stockholm, Sweden: Chapman and Hall.
25. Tomashov, N.D. and G.P. Chernova, *Passivity and Protection of Metals Against Corrosion*. 1st. ed. 1967, New York: Plenum Press.

26. Fontana, M., *Corrosion Engineering*. 3rd ed. Mater. Sci. Eng. 1987, Ohio: McGraw-Hill.
27. Craig, B.D., *Fundamentals Aspects of Corrosion Films in Corrosion Science*. 1st. ed. 1991, New York: Plenum Press.
28. ZHANG, T.C. and D.Y. Li, *J. Mater. Sci.*, 2001. **36**: p. 3479.
29. Trfonov, D.N., *The Rare-Earth Elements*. 1963, New York: The Macmillan Company.
30. Hedrick, J.B., *Rare Earth Elements and Yttrium*. Mineral Facts and Problems, 1985. **675**: p. 647-664.
31. Li, H., A. Mclean, J.W. Rutter, and I.D. Sommerville, *Metall. Trans. B.*, 1988. **19B**: p. 383-395.
32. Guo, M. and H. Suito, *ISIJ Int.*, 1999. **39**(7): p. 722-729.
33. Lan, J., J. He, W. Ding, Q. Wang, and Y. Zhu, *ISIJ Int.*, 2000. **40**(12): p. 1275-1282.
34. Moore, J.J. *Modification of Cast Structure Using Rare Earth Additions*. in *AIME Steelmaking Proc.* 1984.
35. Nuri, Y., T. Ohashi, T. Hiromoto, and K. Kitamura, *Trans. ISIJ.*, 1982. **22**: p. 399-407.
36. Waudby, P.E., *Int. Mat. Rev.*, 1978. **229**(2): p. 74-99.
37. Yang, Q., X. Ren, B. Liao, M. Yao, and X. Wan, *Journal of Rare Earths*, 1999. **17**(4): p. 293-297.
38. Wu, Y.L., F.H. Froes, C.G. Li, and L. J. in *Synthesis/Processing of Lightweight Metallic Materials II*. 1997. Orlando, FL, USA.

39. Wu, Y.L., F.H. Froes, and A. Alvarez, *Metall. Mater. Trans.*, 1999. **A 30A**: p. 1017-1024.
40. Torma, T., *Mater. Sci. Forum*, 1987. **13/14**: p. 497-503.
41. Lichtenberger-Bajza, E. and I. Boczur, *Aluminum*, 1980. **56(10)**: p. 653-657.
42. Wang, P., Z.F. Wang, K.S. Kumar, and C.L. Briant. *Stress Corrosion Cracking of Aluminum-Magnesium Alloys Containing Scandium and Silver*. in *Proc. Chemistry and Electrochemical of Corrosion and Stress Corrosion Cracking*. 2001: TMS.
43. Shao, G.L., Q.Y. Feng, and H.L. Liu. in *Special edition in the proc. 2nd in Int. Conf. on Rare Earths Development and Applications*. 1991. Beijing, China: Journal of rare earths.
44. Wang, X.Y. and D.Y. Li, *Mater. Sci. Eng.*, 2001. **A315**: p. 158-165.
45. Lu, Y.C. and M.B. Ives, *Corros. Sci.*, 1993. **34(11)**: p. 1773-1785.
46. Ahmed, Z., A. Ul-Hamid, and B.J. Abdul-Aleem, *Corros. Sci.*, 2001. **43**: p. 1227-1243.
47. Braun, R., B. Lenczowski, and G. Tempus, *Mater. Sci. Forum*, 2000. **331-337**: p. 1647-1652.
48. Ganiev, I.N., *Russ. J. Applied Chem.*, 1986. **60**: p. 1961-1965.
49. Ganiev, I.N., *Protection of Metals*, 1995. **31**: p. 543-546.
50. Kharina, G.V. and V.P. Kochergin, *Protection of Metals*, 1996. **32**: p. 134-136.
51. Seon, F.M., *J. Less Common Metals*, 1989. **148**: p. 73-81.
52. Sinyavskii, V.S., V.D. Val'kov, and E.V. Titkova, *Protection of Metals*, 1998. **34**: p. 549-555.

53. Vyazovikina, N.V., *Protection of Metals*, 1999. **35**: p. 448-453.
54. Ahmed, Z. and B.J. Abdul-Aleem. *Scandium Alloyed Al5052: A High Performance Material for Marine Environment*. in *Euro. Corr.* 2002.
55. Hamdy, A.S. and A.M. Beccaria, *Corros. Report.*, 2001: p. 101-109.
56. Bennet, M.J. and A.T. Tuson, *Mater. Sci. Eng.*, 1989. **116**: p. 79-87.
57. Buscail, H., C. Courty, M.F. Stroosnijder, Y.P. Jacop, and J.P. Larpin, *Oxid. Met.*, 2002. **49**: p. 561-581.
58. Gueff, R., H. Buscail, E. Caudron, C. Issartel, and F. Riffard, *Oxid. Met.*, 2002. **58**: p. 439-455.
59. Hamid, A.U., *Oxid. Met.*, 2002. **58**: p. 41-56.
60. Hou, P.Y. and J. Stringer, *Mater. Sci. Eng.*, 1995. **202**: p. 1-10.
61. Liu, Z., H. Gao, and Y. He, *Oxid. Met.*, 2002. **53**: p. 341-350.
62. Mennicke, C., E. Schumann, M. Ruhle, R.J. Hussey, G.I. Sproule, and M.J. Graham, *Oxid. Met.*, 1998. **49**: p. 455-466.
63. Perez, F.J., M.J. Cristobal, M.P. Hierro, F. Pedraza, G. Arnau, and P. Merino, *Surf. Coating Tech.*, 2002. **126**: p. 116-122.
64. Phunger, E., A. Schroer, P. Voumard, L. Donohue, and W.D. Munz, *Surf. Coating Tech.*, 1999. **115**: p. 17-23.
65. Wei, Y., C. Zheng, P. Fan, S. Cheng, W. Li, and G. Ying, *Journal of Alloys and Compounds*, 2000. **311**: p. 65-68.
66. Zeng, C.L., F.C. Rizzo, M.J. Monteiro, and W.T. Wu, *Oxid. Met.*, 1999. **51**: p. 495-506.
67. Liu, R. and D.Y. Li, *J. Mater. Sci.*, 2000. **35**: p. 633.

68. Zhang, T.C. and D.Y. Li, Mater. Sci. Tech., 1999. **15**: p. 1441.
69. Zhang, T.C. and D.Y. Li, Mater. Sci. Eng. A, 2002. **325**: p. 87-92.
70. Ahmadi, H. and D.Y. Li, Wear, 2003. **255**: p. 933-942.
71. Ahmadi, H. and D.Y. Li, Surf. Coatings Tech., 2002. **161**: p. 210-217.
72. Wang, X.Y. and D.Y. Li, Surf. Coatings Tech., 2002. **160**: p. 20-24.
73. Zhang, T.C. and D.Y. Li, Mater. Sci. Eng. A, 2000. **277**: p. 18-22.
74. Ramanathan, L.V., Corros. Prev. & Cont., 1998: p. 87-92.
75. Whittle, D.P. and J. Stringer, Phil. Trans. R. Soc. London, 1980. **A.295**: p. 309-329.
76. Whittle, D.P., M.E. El-Dahshan, and J. Stringer, Corros. Sci., 1977. **17**: p. 879-891.
77. Hou, P.Y. and J. Stringer, Oxid. Met., 1972. **5**: p. 11-47.
78. Stringer, J., B.A. Wilcox, and R.I. Jaffee, Oxid. Met., 1972. **5(1)**: p. 11-47.
79. Rhys-Jones, T.N., H.J. Grabke, and H. Kudielka, Corros. Sci., 1987. **27(1)**: p. 49-73.
80. Rhys-Jones, T.N. and H.J. Grabke, Mater. Sci. Tech., 1988. **4**: p. 464-454.
81. Hindam, H. and D.P. Whittle, Oxid. Met., 1982. **19(5/6)**: p. 245-284.
82. Moon, D.P., C.R.M. Grovenor, P.E. Baston, and A.P. Sutton. *In Conf. on Physiscs of Oxidation.* in R. Soc. Chem. 1985. Oxford.
83. Moon, D.P., Surf. Interface. Anal., 1988. **12**: p. 27-34.
84. Ramanarayanan, T.A., M. Raghavan, and R. Petkovic-Lutton, J. Electrochem. Soc., 1984. **131(4)**: p. 923-931.

85. Yurek, G.L., K. Przybylski, and A.J. Garrat-Reed, *J. Electrochem. Soc.*, 1987. **134**: p. 2643-2644.
86. Evans, H.E. and R.C. Lobb. *Metallic Corrosion*. in *9th Int. Cong.* 1984. Ottawa, Canada: NRC Canada.
87. Golightly, F.A., F.H. Stott, and G.C. Wood, *Oxid. Met.*, 1976. **10**: p. 163-187.
88. Anderson, A.B., S.P. Mehandru, and J.L. Smialek, *J. Electrochem. Soc.*, 1985. **132**: p. 1695-1701.
89. Smialek, J.L., *J. Electrochem. Soc.*, 1979. **126**: p. 2275-2276.
90. Reddy, K.P.R., J.L. Smialek, and A.R. Cooper, *Oxid. Met.*, 1982. **17**: p. 429-449.
91. Bennet, M.J., B.A. Bellamy, C.F. Knights, N. Meadows, and N.J. Eyre, *Mater. Sci. Eng.*, 1985. **69**: p. 359-373.
92. Bennet, M.J., J.A. Desport, and P.A. Labun. in *43rd Annual Meeting of Electron Microscopy Society of America (EMSA)*. 1985. San Francisco.
93. Bennet, M.J., H.E. Bishop, P.R. Chalker, and A.T. Tuson, *Mater. Sci. Eng.*, 1987. **90**: p. 177-190.
94. Kvernes, I.A., *Oxid. Met.*, 1973. **6**: p. 45-64.
95. Tien, J.K. and F.S. Pettit, *Metall. Trans.*, 1972. **3**: p. 1587-1599.
96. Sybolt, A.U., *Corros. Sci.*, 1966. **6**: p. 263-269.
97. Lustmann, B., *Trans. Metall. Soc. A. I. M. E.*, 1950. **233**: p. 1587-1599.
98. Giggins, C.S., *Metall. Trans.*, 1974. **5**: p. 1685-1688.
99. Francis, E.J. and W.H. Whitlow, *Corros. Sci.*, 1965. **5**: p. 701-710.
100. Felten, E.J., *Oxid. Met.*, 1961. **10**: p. 23-28.
101. Allam, I.A., D.P. Whittle, and J. Stringer, *Oxid. Met.*, 1978. **12**: p. 35-67.

102. Moon, D.P., Mater. Sci. Tech., 1989. **5**: p. 755-764.
103. Qudakkers, W.J., H. Holzbrecher, K.G. Briefs, and H. Beske, *The Effect of Yttria Dispersion on The Growth Mechanisms and Morphology of Chromia and Alumina Scales*, in *The Role of Active elements in The Oxidation Behavior of High Temperature Metals and Alloys*. 1989, Elsevier Science: Amstrdam. p. 155-173.
104. Whittle, D.P. and D.H. Boone, Mater. Sci. Eng., 1981. **14**: p. 487-502.
105. King, J.F., Advanced Materials Technology Int., 1990: p. 12.
106. Mukhina, I.Y., Chem. Abs., 1972. **4**: p. 125.
107. Chang, C.F., S.K. Das, D. Raybould, R.L. Bye, and N.J. Kim. *Advanced Magnesium Alloys for Aerospace Application*. in *2nd Int. SAMPE Conf. Space Age Metals Technology*. 1984.
108. Hefny, M.M., W.A. Badawy, and S.S. El-Egmy, Electrochem. Acta, 1990. **35**: p. 799.
109. Hampson, N.A. and J.B. Lakeman, J. Electroanal. Chem., 1980. **107**: p. 177.
110. Zhang, T.C. and D.Y. Li, Mater. Sci. Eng. A, 2003. **345**: p. 179-189.
111. Hinton, B.R.W. and L. Wilson, Corros. Sci., 1989. **29**: p. 967-985.
112. Hinton, B.R.W., D.R. Arnott, and N.E. Ryan, Metals Forum, 1984. **7**(4): p. 211-217.
113. Arnott, D.R., B.R.W. Hinton, and N.E. Ryan, Mater. Perform., 1987. **26**: p. 42.
114. Arnott, D.R., B.R.W. Hinton, and N.E. Ryan, Corrosion, 1989. **45**(1): p. 12-18.
115. Arnott, D.R., N.E. Ryan, and B.R.W. Hinton, Application of Surf. Sci., 1985. **22/23**: p. 236-251.

116. Hinton, B.R.W., P.N. Trathen, L. Wilson, and N.E. Ryan. *The Inhibition of Mild Steel Corrosion in Tap Water By Cerious Chloride*. in *Proc. 28th Australian Corros. Assoc. Conf.* 1988. Australia: Australian Corrosion Association.
117. Ryan, N.E., *Rare Earths in High and Low Temperature Corrosion Protection*, in *Rare Earths Resources, Science, Technology and Applications*, R.G. Bautista and N. Jackson, Editors. 1991, TMS: Pennsylvania.
118. Zhang, T.C. and D.Y. Li, *J. Mater. Sci. Peform.*, 1999. **8(6)**: p. 635-640.
119. Zhang, T.C. and D.Y. Li, *J. Mater. Sci.*, 2001. **36**: p. 3479-3486.
120. Caudron, E. and e. al., *Thin Solid Films*, 1999. **350**: p. 168.
121. Zhang, T.C. and D.Y. Li, *Mater. Sci. Tech.*, 1999. **15**: p. 1441-1446.
122. Zhang, T.C. and D.Y. Li, *Surf. Coating Tech.*, 2000. **130**: p. 57-63.
123. Wang, X.Y. and D.Y. Li, *Mater. Sci. Eng.A*, 2001. **315**: p. 158-165.
124. Wang, L. and D.Y. Li, *Wear*, 2003. **255**: p. 535-544.
125. Zhang, T.C. and D.Y. Li, *Wear*, 2001. **251**: p. 1250-1256.
126. Massalski, T.B., *Binary Alloy Phase Diagrams*, 1986. **1**: p. 179-182.
127. Gschneidner, K.A. and F.W. Calderwood, *Bulletin of Alloy Phase Diagrams*, 1989. **10(1)**: p. 44-47.
128. Ludema, K.C., *Friction, Wear, and Librication*. 1st. ed. 1996, Florida: CRC.
129. Hutchings, I.M., *Tribology: Friction and Wear of Engineering Materials*. 1st ed. Metallurgy & Materials Science. 1992, London: Edward Arnold.
130. O'Neil, H., *Hardness Measurements of Metals and Alloys*. 2nd ed. 1967, London: Chapman and Hall.

131. Petty, E.R., *Hardness Testing*, in *Techniques of Metals Research*, R.F. Bunshaw, Editor. 1971, Wiley-Interscience: New York.
132. Tabor, D., *The Hardness of Metals*. 1st ed. 1951, New York: Oxford University Press.
133. Liu, R. and D.Y. Li, *Wear*, 2001. **251**: p. 956-964.
134. Oliver, W.C. and G.M. Pharr, *J. Mater. Res.*, 1992. **7**(6): p. 1564-1583.
135. Bradford, S.A., *Corrosion Control*. 1993, New York: Van Nostrand Reinhold.
136. Godard, H., W. Jepson, M. Bothwell, and R. Kane, *The Corrosion of Light Metals*. 1967, New York: Wiley.
137. Davis, J.R., *Corrosion of Aluminum and Aluminum Alloys*, ed. A. International. 1999, Ohio: Material Park.
138. McCafferty, E., *Corros. Sci.* **45**(7): p. 1421-1438.
139. Pearson, T. and W. Ruther, *Met. Rev.*, 1957. **2**: p. 305.
140. Sinyavskii, V.S., *Prot. Met.*, 2001. **37**(5): p. 469-478.
141. Kharin, G.V. and V.P. Kochergin, *Russ. J. Appl. Chem.*, 1996. **69**(10): p. 1576-1578.
142. Jemmely, P., *Wear*, 2000(237): p. 63-68.
143. Burstein, G.T. and A.J. Davenport, *J. Electrochem. Soc.*, 1989. **136**: p. 936.
144. Liu, R., D.Y. Li, Y.S. Xie, and R. Liewellyn, *Scripta. Mater.*, 1999. **41**: p. 691.
145. *Universal Micro-Tribometer Operation Manual*. Center for Tribology, Inc.
146. Mischler, S., E.A. Rosset, and D. Landolt, *Wear*, 1993. **167**: p. 253-259.
147. Ball, A. and J.J. Ward, *Tribol. Int.*, 1985. **18**: p. 347-351.
148. Barker, K.C. and A. Ball, *Corros. J.*, 1989. **24**: p. 222-228.

149. Batchelor, A.W. and G.W. Stachwiak, *Wear*, 1988. **123**: p. 281-291.
150. Dunn, D.J. *Metal Removal Mechanisms Comprising Wear in Mineral Processing*. in *Wear of Materials*. 1985. Vancouver: ASME.
151. Gatzanis, G.E. and A. Ball, *Wear*, 1993. **165**: p. 213-220.
152. Jiang, X.X., S.Z. Li, D.D. Tao, and J.X. Yang, *Corrosion*, 1993. **49**(10): p. 836-841.
153. Kotlyar, D.C., C.H. Pitt, and M.E. Wadsworth, *Corrosion*, 1988. **44**: p. 221-228.
154. Madsen, B.W., *Mater. Perform.*, 1987. **26**: p. 21-28.
155. Madsen, B.W., *Wear*, 1988. **123**: p. 127-142.
156. Noel, R.E.J. and A. Ball, *Wear*, 1983. **87**: p. 351-361.
157. Schumacher, W.J. *Corrosive Wear Synergy of Stainless Steel*. in *Wear of Materials*. 1985. Vancouver: ASME.
158. Schumacher, W.J., *Mater. Perform.*, 1993. **23**(7): p. 50-53.
159. Yue, Z., Zhou, and J. Shi. *Some Factors Influencing Corrosion-Erosion Performance of Materials*. in *Houston*. 1987. Houston: ASME.
160. Watson, S.W., F.J. Friedersdorf, B.W. Madsen, and S.D. Cramer, *Wear*, 1995. **181-183**: p. 476-484.
161. Wang, X.Y., Li, D.Y. *Tribology lett*, 2001. **11**: p. 117.